Optical Spectroscopy and Magnetic Field Profile Measurements on the Self Magnetic Pinch Diode

by

Sonal Patel

A dissertation submitted in partial fulfillment
of the requirements for the degree of
Doctor of Philosophy
(Nuclear Engineering and Radiological Sciences)
in the University of Michigan
2016

Doctoral Committee:

Professor Ronald M. Gilgenbach, Chair
Mark D. Johnston, Sandia National Labs
Professor Yue Y. Lau
Assistant Professor Louise Willingale

DEDICATION

To family and friends.

ACKNOWLEDGEMENTS

First, I would like to thank my advisor, Professor Ronald Gilgenbach. Over the years he has given me countless opportunities to work on interesting projects. He has taught me a great deal on how to be an experimentalist, and without his guidance I would barely have known how to use a screwdriver let alone how to make these measurements. His advice on starting with the experimental data rather than with previously held notions will always be remembered.

Next, I would like to thank Dr. Mark Johnston, from Sandia National Labs and a member of my committee. I came to Sandia without knowing much about optics and nothing about radiography. Mark taught me so much about how to take precise, optical and spectroscopic measurements and was willing to answer all my, sometimes ridiculous, questions. And without him these measurements would not have been possible.

I would also like to thank Professor Y.Y. Lau for being on my committee and for his amazing classes, all starting from first principles. Additionally, I'd like to thank Professor Louise Willingale for taking the time to be on my committee.

Thank also to the RITS-6 group. Dr. Mark Kiefer, my manager at Sandia, gave me the opportunity to work on this project. Dr. Timothy Webb took the time to explain his radiography data to me, and his spot size measurements were integral to the analysis of the spectral data. Dr. Nichelle Bennett did the simulations in this thesis. Conversations with her about this project were always extremely helpful. Thanks to Dr. Mike Mazarakis and Joshua Leckbee for answering my pulsed power questions and to Sean Simpson for the many interesting conversations. Thanks also to Dr. Yitzhak Maron. Conversations with him were always extremely helpful, and his suggestions were invaluable to these measurements and analysis.

Thanks to Derek Ziska, Frank Wilkins, Robert Obregon, Dan Nielsen, Raymond Gignac, Harvey Wigelsworth, and Tobias Romero for setting up for shots everyday, and for all of the laughter. In particular, thanks to David Muron who was responsible for aligning and fielding some of the optical and spectroscopic equipment. He also taught me everything I know about streak cameras.

Most of my time as a graduate student was spent in the PPPM lab, at the University of Michigan. Thanks especially to Mark Perrault for all the advice and help in setting up experiments on the LTD. The grad students before me, David French, Jacob Zier, and Matthew Gomez, also all taught me a ton. Jacob Zier, in particular, took the time to explain the LTD and plasma physics to me when I was a first year graduate student. Matt Gomez, also at Sandia, let me try some magnetic field measurements on Z, which was an incredibly cool experience. Thanks also to Dr. David Chalenski, who was a research scientist in the PPPM lab.

I'd also like to thank the students I shared grad school with. Matthew Franzi, Ian Rittersdorf, and Steven Excelby, thanks for all the help and good times in and out of lab. Adam Steiner and David Yager, thanks especially for the years of friendship. You guys turned those 40 switches into great memories. Thanks also to Geoff Greening. Our discussion on headlight fluid was extremely valuable. Thanks to David Simon for all the adventures. It wouldn't have been the same without you (I never would've looked up rhodamine).

And finally thanks to my family. My brother, Ravi, was always there for fun conversations and crazy plans. My mom, who arrived here alone from a poor village in India which thought a woman couldn't succeed, has always been an inspiration to me. My dad taught me to dream and he would've been extremely happy to see me graduate.

Sandia National Laboratories is a multi-program laboratory managed and operated by Sandia Corporation, a wholly owned subsidiary of Lockheed Martin Company, for the U.S. Department of Energys National Nuclear Security Administration under contract DE-

AC04-94AL85000. Part of my time as a graduate student was supported by the NPSC fellowship, from Sandia National Labs.

TABLE OF CONTENTS

Chapter

LIST OF FIGURES

LIST OF TABLES

LIST OF APPENDICES

ABSTRACT

Optical Spectroscopy and Magnetic Field Profile Measurements on the Self Magnetic Pinch Diode

by

Sonal Patel

Chair: Ronald M. Gilgenbach

The Self-Magnetic Pinch (SMP) diode has been tested at Sandia National Laboratories on the RITS-6 accelerator for use as a flash x-ray radiography source. The diode consists of a hollow cathode that emits electrons through an approximately 1-cm vacuum A-K gap onto a high-Z material. The electron beam pinches from its own magnetic field as it traverses the gap. Plasmas form on the electrode surfaces and expand into the gap, decreasing the diode impedance over time.

Visible spectra of the electrode plasma have been taken during the radiation pulse using a high resolution spectrometer and a lens coupled fiber array focused across the anode surface of the diode. Electron temperatures have been determined from C III/ C IV line ratios. Electron densities have been estimated from Stark broadened line emission and densities have been estimated from several different ionization states. These measurements suggest that a large axial density gradient is present on the diode surface, with densities varying by up to an order of magnitude within ~1 mm of the anode target surface.

Zeeman splitting measurements of C IV suggest magnetic fields of 3-5 T a few mm from the diode axis. These results differ from LSP simulations of the beam current, and suggest that a significant fraction of the total current density may be outside the few mm x-ray source diameter. Several dopants have also been characterized for Zeeman splitting, intensity, and their effect on the SMP diode performance. Zeeman splitting was measured on the Al III 4s-4p transition and this line may be used in the future to further spatially isolate these measurements. Additionally, it was found that salt coatings on the diode lengthened the radiation pulse. Finally, measurements of the C IV Zeeman line splitting on the anode surface represent the first experimental estimates of current distribution within a diode.

CHAPTER 1

Introduction

Flash radiographic sources typically produce high energy x-rays through bremsstrahlung interactions which are used to image fast hydrodynamic events which has applications for stockpile stewardship. The Radiographic Integrated Test Stand (RITS) at Sandia National Labs (SNL) [1] was developed as a test bed for such sources, and several radiographic diodes have been investigated over the past decade, such as the rod pinch diode [2], the paraxial diode [3], and the self- magnetic pinch (SMP) diode [4–6], the focus of this thesis.

The SMP diode consists of a hollow cylindrical cathode and a planar anode. The cathode emits electrons through an approximately 1 cm vacuum A-K gap onto a high Z material. The electron beam pinches from its own magnetic field as it traverses the gap and consequently, bremsstrahlung x-rays are produced from a source smaller ($<$3 mm) than the cathode diameter. Within a few nanoseconds the electron beam increases the anode surface temperature to $>$400 C [6] and desorbs hydrocarbon contaminants. Electrode plasmas expand into the anode-cathode (AK) gap, decrease the diode impedance over time, and eventually short the diode [5]. In order to limit electrode plasma expansion early in the current pulse an aluminum foil, which is transparent to the electron beam, is typically placed over the high atomic number (Z) target material, such as tungsten, tantalum, or gold.

Dense surface plasmas that form on the anode have a direct effect on the diode performance. Plasma expansion of the anode plasma into the A-K gap eventually shorts the diode, and effectively ends the radiation pulse which reduces the dose. Additionally, the dense anode surface plasma can potentially cause the beam to defocus at the target. [7,8]. Backstreaming ions from the surface plasma and plasma expansion into the AK gap cause the beam focus to shift upstream of the target. This results in an overfocused beam at the target and therefore a larger x-ray source diameter. Therefore, characterizing the electrode plasma composition, densities, and temperatures, is critical to understanding gap closure mechanisms on time scales (10's of nanoseconds) within the diode.

In addition to lengthening the x-ray radiation pulse and therefore maximizing the dose, minimizing the x-ray source spot size is also desired in order to limit image blur. The source diameter depends on the beam current and its self-magnetic field, since the resulting $\mathbf{J} \times \mathbf{B}$ force drives the beam toward the axis. Estimates of the diode current were previously limited to B-dot current monitors and simulations. B-dots, described in detail in Chapter 3, measure the magnetic flux through a wire loop and must be placed outside the AK gap. Therefore they are unable to measure the current distribution within the diode.

Non-perturbing methods of measuring magnetic fields include Faraday rotation and Zeeman splitting. Faraday rotation requires an external light source with a known polarization direction, such as a laser. When the laser interacts with the magnetic field, its polarization angle will rotate. For the case of an azimuthal magnetic field, the Faraday rotation for a laser beam travelling radially across the field lines, will be reversed on either side of the axis, and polarimetry techniques are often used to deduce the polarization angle [9]. However, since the polarization angle is proportional to $\int n_e \mathbf{B} \cdot \mathbf{dl}$ [10], the data represent an integrated measurement along the line of sight. Consequently, measurements along large density or B-field gradients cannot be used to approximate local magnetic fields. Additionally, a line integrated electron density is required, but can be obtained using interferometry along the same line of sight as the Faraday rotation measurements [10].

In contrast, Zeeman splitting, the technique explored in this thesis, can be used to infer local magnetic fields within a plasma. The Zeeman effect was first discovered in 1896 by Pieter Zeeman who measured broadening of the sodium D lines in an external magnetic field. By this time Lorentz had already theorized that charged particles, acting as harmonic oscillators bound to the nucleus, are responsible for emitted light. In the presence of a magnetic field, he suggested, these particles experience both the harmonic force and the Lorentz force. The subsequent motion can be decomposed into three components, the original linear oscillation, and two circular oscillations in opposing directions, resulting in three spectral lines. Zeeman was also able to estimate the charge to mass ratio of the charged particles using this theory, which became a key piece of evidence for the electron [11].

Shortly after the discovery of the Zeeman effect, with higher resolution measurements, it was found that most spectral lines split into more than three components. This effect, although more common than normal Zeeman splitting, was termed the anomalous Zeeman effect. Though empirical rules were able to predict the line splitting, it was not until the development of quantum mechanics and the discovery of electron spin, that anomalous splitting was fully explained [12]. The coupling of the spin angular momentum to the orbital angular momentum breaks the atomic degeneracy in the orbital quantum number and results in additional atomic energy levels. The normal Zeeman effect is recovered when the total spin is zero for both the upper and lower energy levels of a transition. The theory of the Zeeman effect is discussed in more detail in Chapter 2.

Since the energy shift of a level is proportional to the magnetic field it is possible to determine the field by measuring the splitting of a spectral line. Still, the parameter space in which splitting measurements are possible is restricted by line broadening which is typically dominated by the instrument resolution and electron density in the SMP diode plasma. However, in this thesis, the spectral line profiles are either split or sufficiently broadened to fit the profiles with a magnetic field.

Like Faraday rotation, Zeeman splitting measurements can be complicated by variations of the magnetic field along the line of sight. The contribution of different plasma conditions can obscure the splitting and must be deconvolved in order to estimate a local magnetic field. However, dopants can be used to isolate the spectral line and obtain a truly localized measurement. Since the electron beam in the SMP diode is assumed to be cylindrically symmetric, current profiles can also be obtained.

Chapter 2 will discuss some additional background of dense plasma spectroscopy that will be used in this thesis. Chapter 3 will discuss the experimental setup for the measurements. Chapter 4 will discuss electron temperature and density measurements in the SMP diode. Electron temperatures are obtained using the line ratios of adjacent ionization states in conjunction with PrismSPECT [13], a commercial collisional-radiative code which solves the rate equations of various atomic processes. Electron densities are estimated using Stark broadened spectral lines, and the electron densities obtained from different ionization states are compared. These measurements suggest that a large axial density gradient is present on the diode surface, with densities varying by an order of magnitude within 1 mm from the surface.

Chapter 5 will discuss the measurements of Zeeman split spectral lines and current profile estimates on the SMP diode. Current and magnetic profile measurements, which are critical to understanding diode performance and x-ray spot size measurements, have been measured for several different shots and diode configurations on RITS-6. These measurements represent the first measurements of current distributions within a diode. The measurements differ from LSP [14,15] (a hybrid PIC code) simulations of the beam current and suggest that the current density is distributed within a larger radius on the target surface than the simulations suggest. Dopant lines are also assessed for Zeeman splitting, intensity, and their effect on the SMP diode performance. Identifying dopant lines with strong signals and line splitting on the SMP diode may be useful for magnetic field measurements in other applications with similar plasma parameters, such as the Z-machine convolute for which the Zeeman effect may be used to estimate the current loss in the convolute. Conclusions and suggestions for future work will be given in Chapter 6.

CHAPTER 2

Spectroscopy of Dense Plasmas

Measuring the emitted optical radiation of plasmas can yield insights into a range of plasma parameters such as electron and ion temperatures, densities, and species. The spectra collected on RITS-6 and discussed in this thesis contain both continuum radiation from radiative recombination and bremsstrahlung interactions, and line emission from bound-bound transitions, pictured in Figure 2.1.

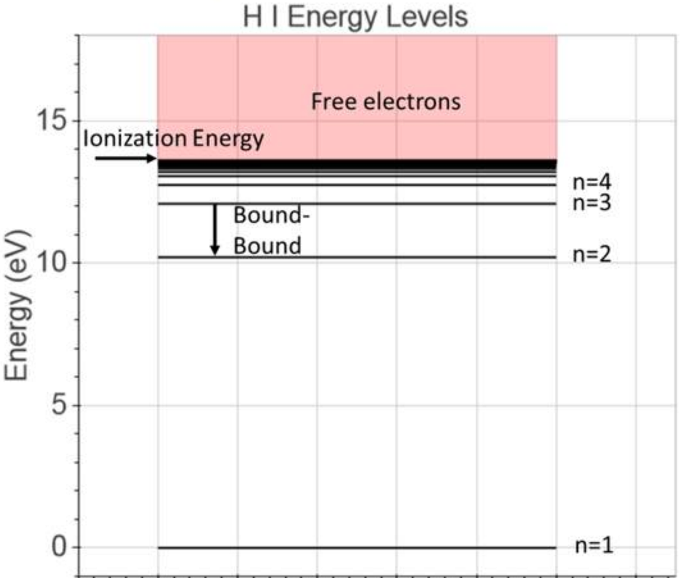

Figure 2.1: H I energy levels with continuum and line emission transitions. The bound-bound transition results in the H-alpha line which is widely used for density measurements.

Free-free transitions, or bremsstrahlung, occurs when an ion deflects an electron and the resulting photon is emitted with an energy that is equal to the electron energy loss. X-ray bremsstrahlung radiation is produced in the SMP diode for use in flash radiography [16]. Since the intensity of bremsstrahlung radiation is proportional to the square of the atomic number of the target, a high Z material, such as tungsten or tantalum, is used to convert the electron beam to x-rays. Free-bound transitions, or radiative recombination, occurs when an ion captures a free electron. The resulting photon energy is the ionization energy of the ion starting from the bound state of the electron subtracted from the kinetic energy of the electron. The opposing process is called photoionization, in which a bound electron is ejected from the atom or ion.

Bound-bound transitions result in characteristic line emission or absorption. The photon energy corresponds to the difference between the upper and lower energy levels of the transition. Emission lines are used in this thesis to determine electron density, electron temperature, and magnetic field profiles across the anode surface of the SMP diode.

2.1 Line Broadening

The profile of a spectral emission line is determined by several mechanisms. Typically, these mechanisms are approximated as either Gaussian or Lorentzian distributions which are convolved together to form a Voigt profile, a common line shape for spectra that have been broadened by the instrument resolution, temperature, and density [17].

2.1.1 Natural Line Broadening

All spectral lines have a minimum width, which is approximated as a Lorentzian profile, due to the time-energy uncertainty principle, given by $\Delta E \Delta t = \hbar/2$, where t indicates the lifetime of the excited state, and can be approximated as the inverse of the transition's Einstein coefficient. Solving for ΔE gives the resulting width of the spectral line [18]. This is an extremely small broadening mechanism. For example the C IV line at 580.1 nm, studied extensively in this thesis, has an Einstein coefficient of 3.14×10^{7} s^{-1} and therefore a natural line width of 5.6×10^{-6} nm , several orders of magnitude less than the instrument resolution of 0.065 nm. For this reason natural line broadening is not included in the spectral line fits.

2.1.2 Thermal Doppler Broadening

Thermal Doppler broadening produces a Gaussian line shape and occurs when ions or atoms have a distribution of velocities as a result of the electron temperature. Velocity components along the line of sight cause red and blue Doppler shifts in the measured spectra. Because there is a range of velocities the line is broadened rather than shifted. For a Maxwellian electron energy distribution the line width is given by [19]

$$\Delta\lambda = 2\sqrt{\frac{2\ln(2)kT}{m_o c^2}}\lambda_0 \tag{2.1}$$

where kT is the ion energy, m_o is the ion mass, λ_0 is the center wavelength. Although this broadening mechanism was included in the spectral analysis, the effect was about half the instrument resolution.

2.1.3 Instrumental Broadening

Another Gaussian contribution to the line profile is instrumental broadening. The optical system used to collect the spectra determines the minimum spectral line width. This is usually dominated by the grating, the entrance slit width, and the camera resolution. For the SMP diode spectral analysis the resolution was determined from the spectrum of a glow discharge lamp. The spectrum was then fit with a Gaussian profile to determine the FWHM of a spectral line. The procedure is discussed further in Chapter 3.

2.1.4 Stark Broadening

Spectral lines shift and split in the presence of an external electric field. On a smaller scale, electric fields caused by nearby particles, such as electrons and ions, perturb the emitter. Consequently, a range of micro electric fields cause the spectral line to broaden. In the absence of other broadening mechanisms the electron density can be determined from the FWHM of the Lorentzian component of the spectral line fit. The relation between the Stark width of a line and the corresponding electron density has been extensively studied theoretically [20, 21] and experimentally [22]. Stark broadening is discussed in more detail in Chapter 4 where it is used to determine densities from the SMP diode spectral data.

The convolution of the Gaussian and Lorentzian profiles results in a Voigt profile. The Gaussian profile is determined from the instrument resolution, and the thermal Doppler width (estimated from the electron temperature), which is discussed further in Chapter 4. Compared to Gaussian profiles, the Lorentzian profile has larger wings which extend further further out from the line center. Additionally, the Lorentzian width for a particular electron density depends on the spectral line, and is often termed the Stark Width. For the SMP diode anode surface plasma, C IV Lorentzian widths ranged from the Gaussian width to several times the Gaussian width.

The width of the Voigt profile in terms of the Gaussian and Lorentzian widths can be approximated by [23]

$$W_V = \frac{1}{2}\left(1.0692 + \sqrt{0.86639W_L^2 + 4W_G^2}\right) \tag{2.2}$$

This approximation is accurate to within 0.02% [23]. The convolution of two Gaussian distributions results in a Gaussian profile with a width equal to the widths of the original profiles added in quadrature. Similarly, the convolution of two Lorentzian profiles results in a Lorentzian with a width equal to the sum of the two original Lorentzian widths. The effect of the four broadening mechanisms discussed here is shown in Figure 2.2.

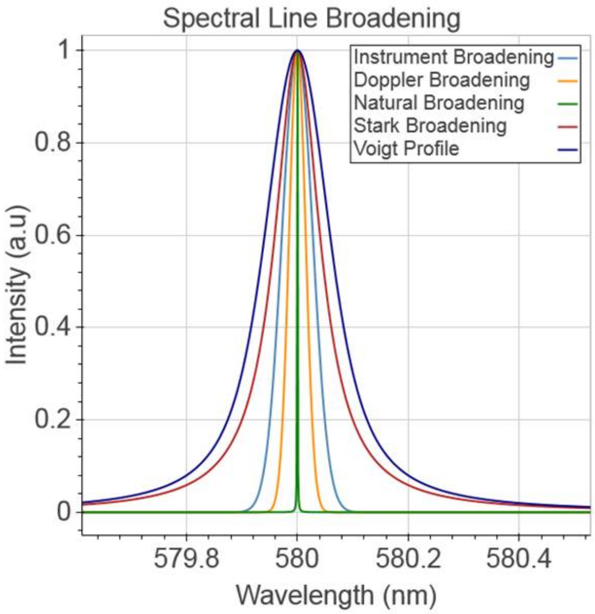

Figure 2.2: Spectral line broadening due to various effects. Typically on the spectra seen on the SMP diode, Stark broadening dominates the line shape.

2.2 Zeeman Splitting

Four quantum numbers can be used to characterize electrons within an atom. The principle quantum number, n, refers to the principle energy level. The orbital quantum number, l, describes the shape of the sublevel in n. The magnetic quantum number, $\mathrm{m_l}$, determines the orientation and number of orbitals. Finally, the spin, $\mathrm{m_s}$, refers to the intrinsic spin of the electron, $\pm 1/2$. The interaction between the motion of an electron and the intrinsic spin causes what is known as spin-orbit coupling. The total angular momentum is given as $\mathbf{J} = \mathbf{L} + \mathbf{S}$, the sum of the total orbital angular momentum (L) and the total spin (S) angular moment for light atoms or ions. (For higher Z elements, a better approximation is $\mathbf{J} = \sum \mathbf{l}_i + \mathbf{s}_i$. The spin and orbital angular momenta, in this case, are first coupled together to form the angular momentum, j, for each electron. The individual angular momenta are then summed to obtain the total angular momentum. This is known as jj coupling). Spin orbit coupling prevents the degeneracy in l but maintains degeneracy in j.

The addition of an external magnetic field, however, also breaks the degeneracy in j.

This effect is usually derived as a perturbation on the Hamiltonian, or the total energy of the system [24]. In the weak magnetic field limit the energy separation between the atomic fine structure levels, due to spin-orbit interactions, is much greater than the separation between the Zeeman split levels, and the total angular momentum vector processes about the external magnetic field vector. The fine structure dominates in the weak field case, and the Zeeman effect is treated as a perturbation on the fine structure energy. To first order, the correction to the energy is given by [25]

$$E_n^1 = \langle \psi_n | H' | \psi_n \rangle \tag{2.3}$$

ψ_n is the wave function for the state and H' represents the perturbing energy. The equation says that the expectation value of H' in the unperturbed state, ψ_n, is the energy correction to the system. Griffiths textbook has a detailed derivation of the Zeeman effect [24], which is summarized here.

The perturbation due to an external magnetic field is

$$H_z' = -\left(\mu_l + \mu_s\right) \cdot \mathbf{B} = -\left(-\frac{e}{2m}\mathbf{L} - \frac{e}{m}\mathbf{S}\right) \cdot \mathbf{B} = \frac{e}{2m}\left(\mathbf{L} + 2\mathbf{S}\right) \cdot \mathbf{B} \tag{2.4}$$

where μ_s refers to the spin magnetic moment and μ_l is the orbital magnetic moment. The extra factor of two in the spin magnetic moment arises from a quantum mechanical correction known as the g-factor.

$$E_n^1 = \langle \psi_{nljm_j} | H' | \psi_{nljm_j} \rangle = \frac{e}{2m}\mathbf{B} \cdot \langle \mathbf{L} + 2\mathbf{S} \rangle = \frac{e}{2m}\mathbf{B} \cdot \langle \mathbf{J} + \mathbf{S} \rangle \tag{2.5}$$

Since ψ_{nlm_j} is an eigenfunction of $\mathbf{J}$, the expectation value for $\mathbf{J}$ is simply the eigenvalue of $\mathbf{J}$, $\hbar m_j$. m_j is the z component of the angular momentum. $\mathbf{S}$ precesses about the vector $\mathbf{J}$ and so the time average of $\mathbf{S}$ is equal to its projection along $\mathbf{J}$, $\mathbf{S}_{ave} = \frac{\mathbf{S}\cdot\mathbf{J}}{\mathbf{J}^2}\mathbf{j}$.

$$\begin{aligned} \mathbf{L} = \mathbf{J} - \mathbf{S} \rightarrow L^2 + J^2 + S^2 = 2\mathbf{J} \cdot \mathbf{S} \rightarrow \mathbf{J} \cdot \mathbf{S} &= \frac{1}{2}\left(J^2 + S^2 + L^2\right) \\ &= \frac{\hbar^2}{2}[j(j+1) + s(s+1) - l(l+1)] \end{aligned} \tag{2.6}$$

$$\frac{e}{2m}\mathbf{B}\cdot\langle\mathbf{J}+\mathbf{S}\rangle = \frac{e}{2m}\mathbf{B}\cdot\left(\hbar m_j + \left(\frac{\hbar^2[j(j+1)+s(s+1)-l(l+1)]}{2\hbar^2 j(j+1)}\right)\langle\mathbf{J}\rangle\right) \tag{2.7}$$

And so the Zeeman energy correction, in the weak field approximation is

$$E_n^1 = \frac{e\hbar}{2m} g m_j B = \mu_B g m_j B \tag{2.8}$$

where g is the lande g-factor, and μ_B is the Bohr magneton constant. The magnetic field has been chosen to be along the z-axis and correspondingly, m_j.

In the strong field case, known as the Paschen-Back effect, the energy separation due to the magnetic field is much greater than the fine structure energy separation. (C IV, analyzed in this thesis, is in the weak field regime for magnetic fields less than about 25 T, and in the Paschen-Back or strong field regime at fields greater than about 40 T.) The quantum numbers j and mj are not applicable here because L and S are decoupled. And so the energy shift is given by

$$\begin{aligned} E_n^1 &= \langle\psi_{nlm_lm_s}|\frac{e}{2m}\mathbf{B}\left(\mathbf{L}+2\mathbf{S}\right)|\psi_{nlm_lm_s}\rangle \\ &= \langle\frac{e}{2m}\mathbf{B}\left(\mathbf{B}+2\mathbf{S}\right)\rangle = \frac{e\hbar}{2m}B(m_l+2m_s) \end{aligned} \tag{2.9}$$

In the intermediate case, the fine structure and Zeeman splitting result in comparable energy shifts, and the perturbing energy in Equation 2.3 is the sum of the fine structure and Zeeman Hamiltonians. This case requires the use of degenerate perturbation theory [24], and will not be considered further.

A schematic for the strong and weak field approximations is shown in Figure 2.3. In the weak field approximation four pi lines and six sigma lines are visible. In the strong field, or Paschen-Back approximation three sets of closely spaced doublets are visible, which in practice usually appear as three lines due to line broadening. The spectral lines analyzed in this thesis for Zeeman splitting were in the weak field regime.

Zeeman split lines, designated as pi ($\Delta m_j = 0$) and sigma ($\Delta m_j = \pm 1$), are polarized

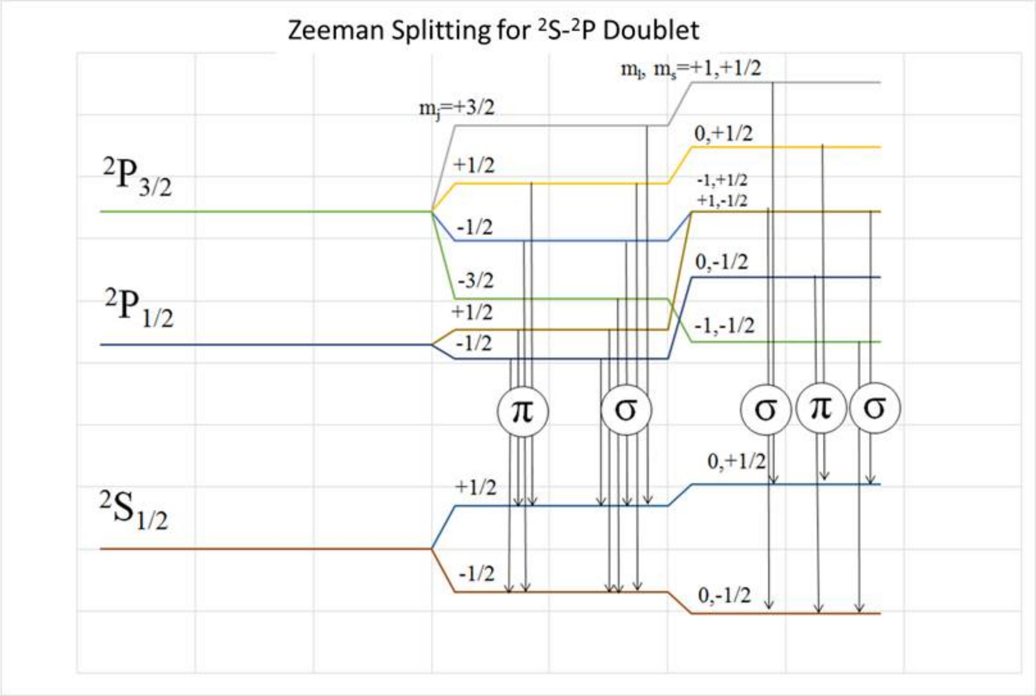

Figure 2.3: A schematic for line splitting in an external magnetic field in the Zeeman and Paschen-Back approximations.

depending on the angle of the line of sight to the magnetic field. When measuring parallel to the magnetic field only the circularly polarized sigma lines are present. Perpendicular to the field, pi lines are polarized parallel to the field, and sigma lines are polarized perpendicular to the field. A textbook by A.E. Siegman [26] gives a derivation of the Zeeman pattern polarization properties. In summary, the pi transitions can be thought of as an electric dipole oscillating along the magnetic field axis. Light is only emitted perpendicular to the oscillation direction, and so when viewing parallel to the field, the central pi lines are not visible. The sigma transitions resemble a rotating dipole centered on the B-field axis, as shown in Figure 2.4.

The Zeeman components also vary in intensity. The Zeeman relative intensities were first determined empirically by Ornstein and Burger in 1924 based on three rules [27]. The first simply states Zeeman splitting occurs symmetrically around the unshifted line. The second states that the sum of the intensities in the upper or lower Zeeman split atomic level is equal to the sum of the intensities in any other upper or lower Zeeman split level. And

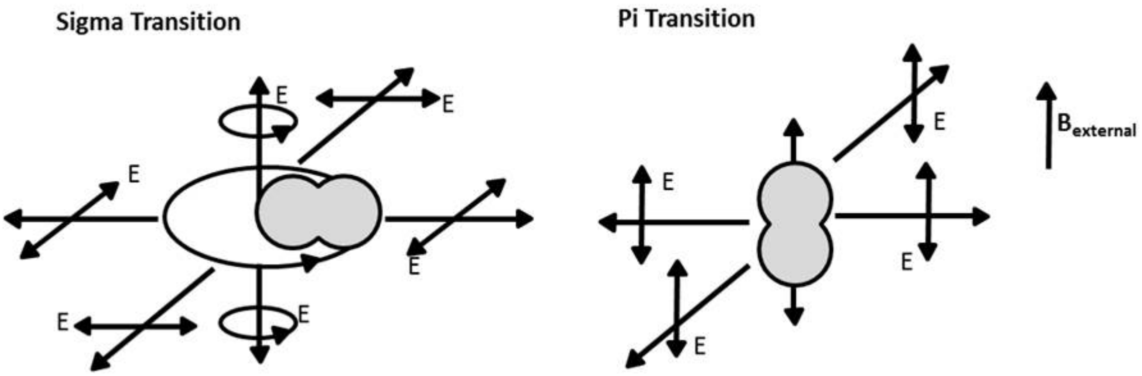

Figure 2.4: Sketch of the Zeeman component transitions and polarizations which are designated by the E-field direction.

the last rule states that the combined components must result in unpolarized light. Later these were confirmed with a quantum mechanical derivation [28].

Finally, the line intensities also depend on the angle of the line of sight to the magnetic field. This dependence was derived in 1981 by Martin and Wickramasinghe [29] for a Zeeman multiplet using the four Stokes parameters which describe the polarization of EM waves. The angle dependences are

$$I_{\pi}(\theta) = I_{90} sin^2\theta, \quad I_{\sigma}\theta = I_{90}(1 + cos^2\sigma) \tag{2.10}$$

where θ is the angle between the line of sight and the magnetic field, and I_{90} is the intensity of the component with a perpendicular line of sight to the magnetic field, given in Table 2.1.

Using these intensity calculations a simulated spectrum is calculated for the C IV $^2P_{3/2} -^2 S_{1/2}$ and $^2P_{1/2} -^2 S_{1/2}$ transition. The location of the Zeeman components and relative intensities are shown as well.

The resolution requirement is lowered for a parallel line of sight because the central pi lines for both transitions are not visible. Additionally, a linear polarizer, aligned perpendicular to the field, could also be used to block the pi components in a perpendicular line of sight.

For Stark dominated line shapes, the splitting may not be apparent, as in the case of

Table 2.1: Relative intensity of the Zeeman components for a perpendicular line of sight to the B-field.

$\Delta J = -1$	
Comp.	Relative,Intensity [28], [30]
σ_-	$\frac{1}{4}(J+m_j)(j+m_j-1) \propto I_o$
π	$J^2 - m_j^2 \propto I_o$
σ_+	$\frac{1}{4}(J-m_j)(j-m_j-1), \propto I_o$
$\Delta J = 0$	
Comp.	Relative Intensity
σ_-	$\frac{1}{4}(J+m_j)(j+m_j+1) \propto I_o$
π	$m_j^2 \propto I_o$
σ_+	$\frac{1}{4}(J-m_j)(j-m_j+1) \propto, I_o$

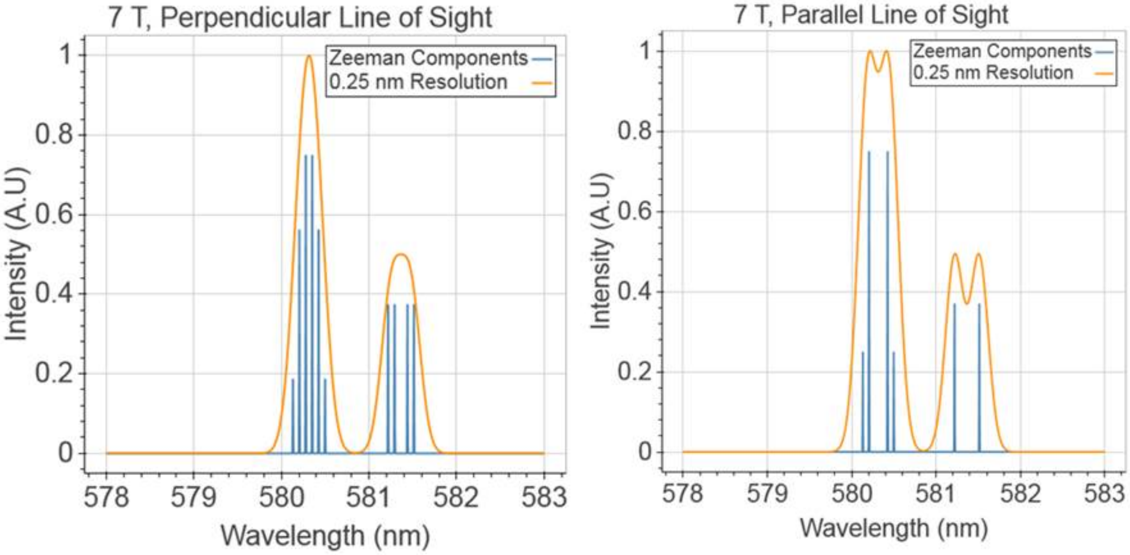

Figure 2.5: Simulated spectrum of C VI $^2P_{3/2} -^2 S_{1/2}$ and $^2P_{1/2} -^2 S_{1/2}$ lines. The location and relative intensities of the lines are also shown. In the parallel line of sight the pi lines are not visible.

the perpendicular line of sight in Figure 2.5. However, the $^2P_{1/2} -^2 S_{1/2}$ is slightly broader than the $^2P_{3/2} -^2 S_{1/2}$ since the pi to sigma ratio for this line is 1:1 on the 1/2-1/2 transition, and 2:1.5:0.5 for the 3/2-1/2 transition. Additionally, the energy shift from the unshifted line for the pi transition is $\Delta E = \frac{2}{3}\mu_B B$ on the 1/2-1/2 transition and $\Delta E = \frac{1}{3}\mu_B B$ B for the 3/2-1/2 transition. This effect led to the development of the Zeeman broadening technique at the Weizmann Institute [31, 32] The technique uses the width difference of the two lines to estimate the magnetic field. The SMP diode spectra that are analyzed in this thesis usually show visible line splitting and so are fit with a simulated profile. Still, this technique is used qualitatively for higher density spectra located within 3-4 mm of the beam axis to determine if a magnetic field is present before fitting the line profile, as is discussed in Section 5.5.

CHAPTER 3

Experimental Configuration

The analysis of the magnetic field profiles and plasma parameters on the SMP diode relied on several diagnostics that were fielded on the Radiographic Integrated Test Stand (RITS-6). The RITS-6 Accelerator, pictured in Figure 3.1, is an induction voltage adder (IVA) which is comprised of six inductively isolated cavities. A Marx bank, which contains 36, 2.2 μF capacitors, discharges into two intermediate storage capacitors which are each connected to six pulse forming lines (PFLs), through two laser triggered gas switches [1]. The six PFLs each contain a self-breaking water switch, a water peaking switch used to sharpen the rise time, and an oil pre-pulse switch. As the PFLs charge, some voltage will enter the diode region which could cause plasma formation on the electrode surfaces. To reduce this pre-pulse the oil switch is placed in series with the two other water switches. Each PFL is triggered sequentially and is timed to match the pulse propagation along the magnetically insulated transmission line (MITL), resulting in a fast rise time and flat top pulse at the diode [33].

Each annular cavity consists of an azimuthal transmission line, a ferromagnetic core, and a vacuum insulator stack. The voltage pulse is injected into the cavity at a point on the azimuthal transmission line which is tapered with the maximum width on the injection side and the minimum width on the opposite side in order to uniformly distribute the current on the MITL and minimize the cavity rise time [34].

A radial transmission line connects the azimuthal line to the inner radius of the cavity

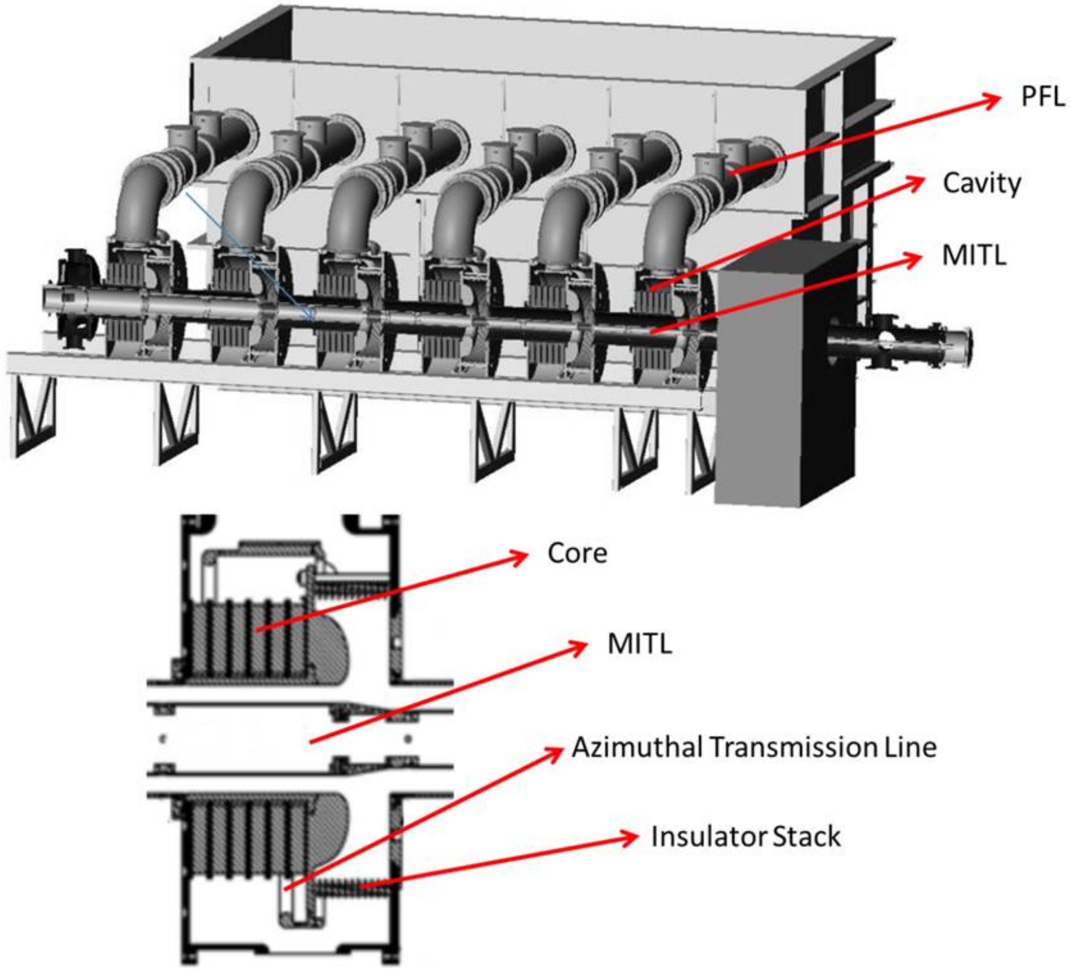

Figure 3.1: RITS-6 Accelerator (top) with six pulse forming lines (PFLs) and cavities. A single cavity cross section (bottom) is also shown.

annulus. The radial transmission line and vacuum insulator stack form the vacuum region of the cavity. The ferromagnetic cores increase the inductance between the high voltage side of the azimuthal transmission line and the outer radius of the annular cavity which is at ground. This isolation greatly reduces the loss current in each cavity and allows the voltage from multiple cavities to be added along the MITL [34]. However, as the current increases the magnetic flux density also increases in the core, until the saturation point of the ferromagnetic material. At this point no further magnetization of the material occurs, the core inductance falls, and the ground path is no longer isolated.

3.1 Self Magnetic Pinch (SMP) Diode

The RITS-6 accelerator is used to deliver power to the SMP diode, which consists of a cylindrical hollow cathode and planar anode, shown in Figure 3.2. The diode can generate >350 rads at 1 m with a sub-3 mm x-ray spot FWHM [6]. The large electric fields cause electrons to emit from the cathode and impact the anode. The electron beam pinches onto the anode target from its self-magnetic field. A high Z target material, typically tantalum, converts the beam energy to bremsstrahlung x-rays for use as a flash radiography source [16].

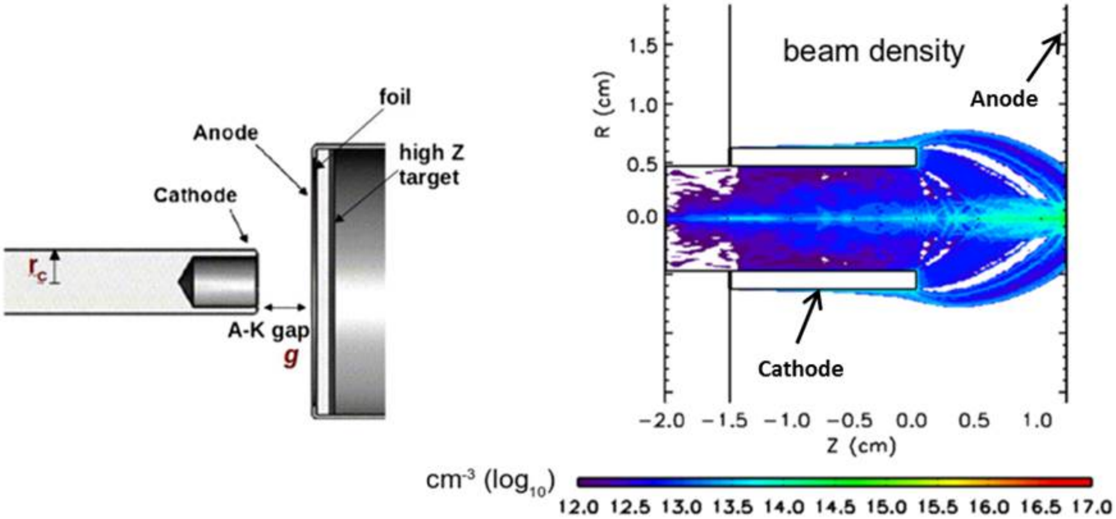

Figure 3.2: Sketch of the SMP Diode (left) [5]. Simulation of the electron beam density in the diode [4] which shows the beam pinching onto the anode surface.

The electron beam heats the anode to temperatures greater than 400 C within a few nanoseconds [6] which causes space-charge limited ion emission. The ions partially charge neutralize the electron beam, resulting in higher beam currents and stronger pinching. Eventually, the electrode plasma formation expands into the AK gap decreasing the diode impedance [35]. To extend the x-ray radiation pulse and delay the electrode plasma from shorting the AK gap, an aluminum foil, which is transparent to the electron beam, is placed over the high Z convertor in the standard SMP diode geometry. For many of the shots discussed in this thesis, however, the foil was removed to increase the spectral signal. Diagnostics for the SMP diode include spot size measurements, time-gated framing camera images, streak spectroscopy, and time-gated spectroscopy, which will be discussed further in the following sections.

3.2 Current Monitors

B-dot probes are often used in pulsed power experiments in order to characterize load currents. In the simplest configuration, shown in Figure 3.3, current flow causes a time changing magnetic field which induces a voltage in a single wire loop. Therefore, the voltage signal is proportional to $\frac{dI}{dt}$, and is integrated to recover the current trace. Often, there are several loops in a B-dot and the two wire leads are twisted together to further enhance the signal. The B-dots on RITS-6 contain three loops that are embedded in a non-conducting epoxy.

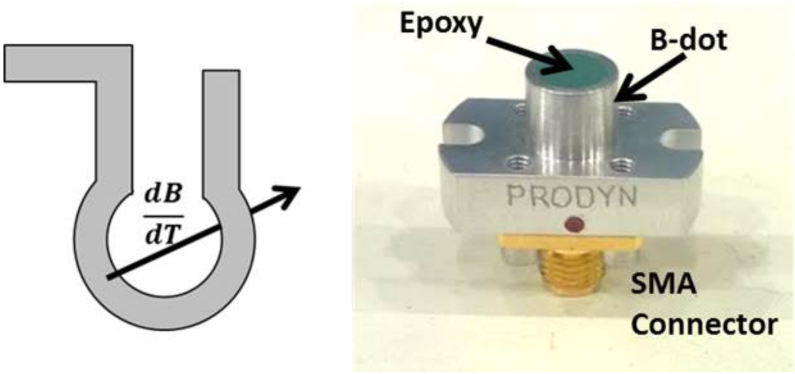

Figure 3.3: Left: Example of a single loop B-dot probe. Right: Cathode faceplate B-dot (at IBEAM in Figure 3.4) used on RITS-6

The SMP diode current includes both ion and electron flow and is measured using B-dots placed behind the cathode stalk. More recently, in order to separate out the ion current, copper coupons were placed behind the cathode to measure activation due to back-streaming protons from the anode plasma [36]. Multiple B-dots are also placed along the RITS-6 transmission line to characterize the power flow along the accelerator.

Figure 3.4 shows the locations of the B-dots used on this accelerator. Positions F and G

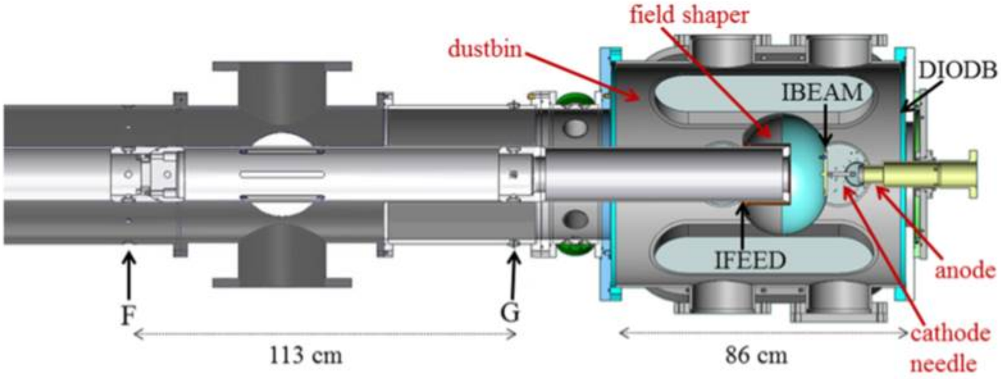

Figure 3.4: Location of B-dots on RITS-6, at positions F, G, IFEED, IBEAM, and DIODB [35]

measure the current along the MITL. IFEED measures the electron current before the field shaping knob. At this point some of the diode current is lost to the sheath current which goes around the cathode and contacts the anode or outer vacuum chamber walls. This can be seen in the difference between the current measurements at DIODB and IBEAM. The IBEAM B-dots measure the beam current and emission from the cathode faceplate within a 6.5 cm circle.

3.3 Voltage Calculations

Voltages are calculated from the MITL B-dots at Position F in Figure 3.4. A set of four B-dots is placed symmetrically around the inner conductor to measure the cathode current, while a second set is placed on the inner anode surface to measure the anode current. The difference between the anode and cathode current represents the free electron sheath current [37], and it is plotted in Figure 3.5 for a typical SMP diode geometry.

The average value of both currents is used with Mendel's equation to obtain the voltage [38, 39]

$$V = Z\left(I_a^2 - I_c^2\right)^{\frac{1}{2}} - \frac{mc^2}{eF}\left(\frac{I_a}{I_c} - 1\right) \times \left(G\left[2F\left(\frac{I_a}{I_c} + 1\right)\right]^{\frac{1}{2}} - 1\right) \tag{3.1}$$

F and G are space charge terms and are typically taken as equal to 1 [39]. Z is the MITL impedance, 51.3 Ω, and I_a and I_c are the anode and cathode currents. The voltage for Shot 1960 is plotted in Figure 3.6.

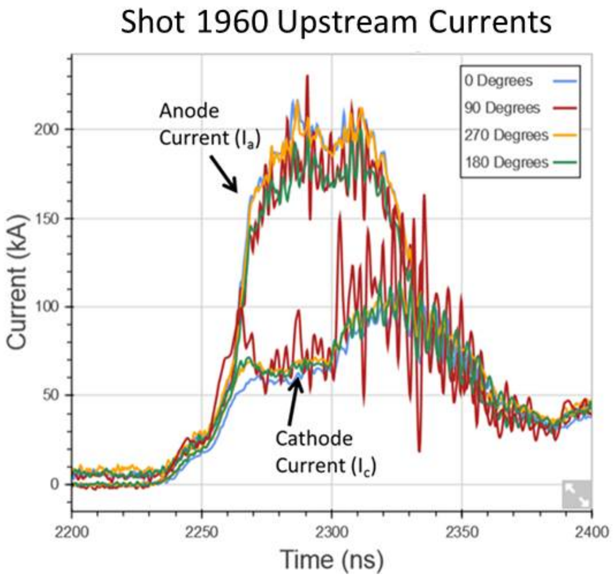

Figure 3.5: Cathode and anode currents for a standard SMP diode shot.

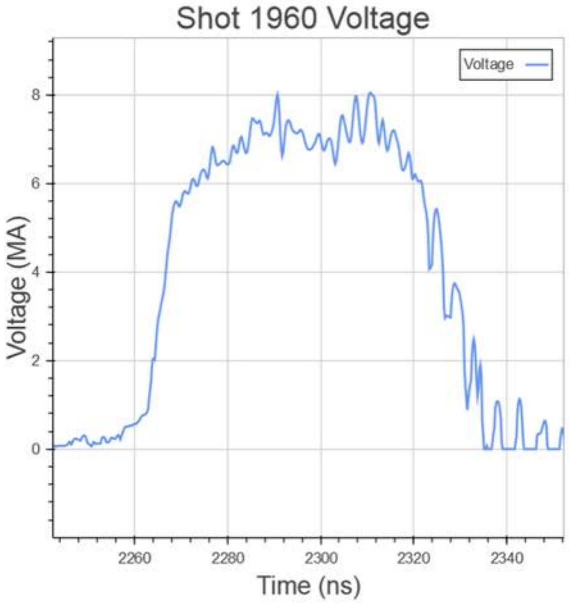

Figure 3.6: Voltage calculated using Equation 3.1 from the currents measured at Position F shown in Figure 3.4.

3.4 ICCD Framing Camera

In addition to spectroscopic measurements a single frame ICCD PI-Max [40] camera images the AK gap and the self-emission from the plasmas that form on the diode electrodes. The images are particularly useful for determining whether asymmetries in the plasma formation affected the measured spectra. Light from the diode exits the vacuum chamber and two turning mirrors direct the light into a telescoping lens assembly which images the light onto the camera, as shown in Figure 3.7. For the shots discussed in this thesis, the framing camera was gated for about 10 ns, toward the end of the radiation pulse. A pre-shot image was taken with this camera before every shot to check alignment and to provide a baseline from which to measure plasma expansion into the gap. Due to the intensity of the anode plasma during the shot, a low gain of about 25 was used along with an f-stop value of f-22.

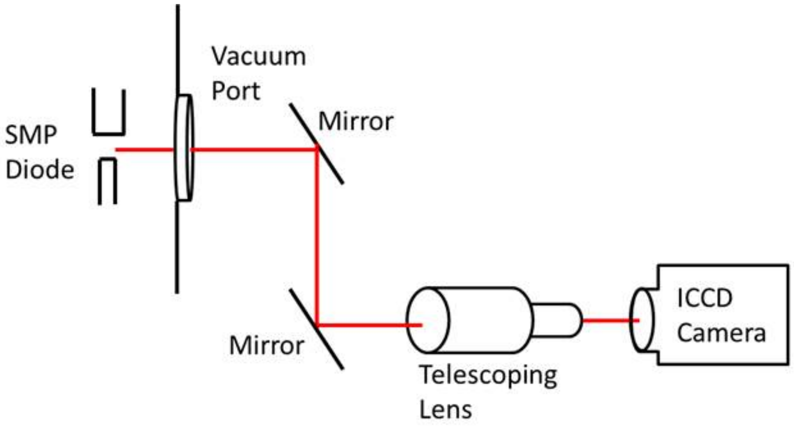

Figure 3.7: Diagram of the framing camera setup.

Previously, an 8-Frame camera was fielded by Dr. Mark Johnston using the same setup in Figure 3.7. This camera was able to take 7-8 images of the electrode plasma formation during the pulse separated by about 10 ns. These images are used to estimate radial plasma expansion of the anode plasma in order to determine the influence of Doppler shifts in the spectra.

3.5 Visible Spectroscopy Diagnostics and Calibration

Three types of spectrometers were used in this experiment, but the principle operating mechanisms for each spectrometer are similar. Broadband light enters through a spectrometer slit, a grating disperses collimated light into its component wavelengths, and a concave mirror focuses the light onto a detector. This type of configuration is sketched in Figure 3.8, and is known as a Czerny-Turner spectrometer [41].

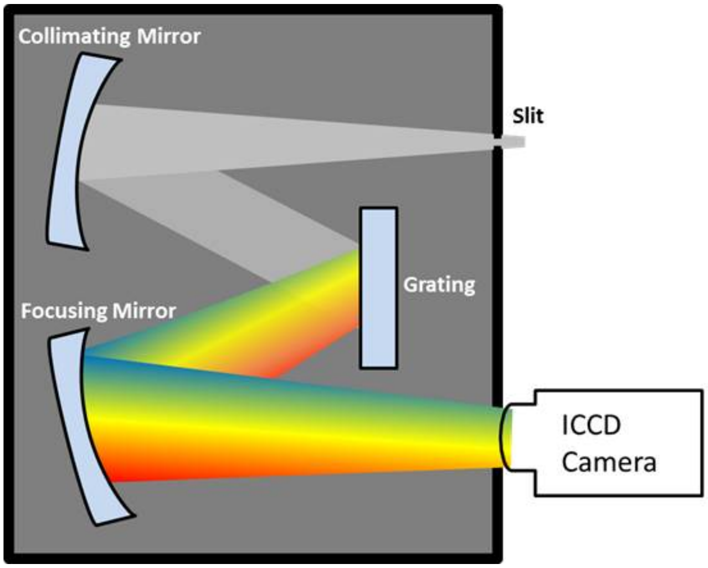

Figure 3.8: Sketch of a Czerny-Turner spectrometer with two concave mirrors.

The resolution of this spectrometer depends on several components. The spectrometer slit width usually dominates the instrument resolution, and a smaller slit improves the resolution at the expense of signal. The grating determines the dispersion of light. Higher grooved gratings result in greater dispersion and thus better resolution, again at the expense of signal. The ICCD camera digitizes the signal with a resolution that depends on the pixel size.

The gratings used on these experiments were reflective diffraction gratings. These gratings function similarly to a series of many narrow slits. And so both constructive and destructive interference cause multiple diffraction orders of the reflected light [42]. The reflective characteristics of these gratings are shown in Figure 3.9 and can be summarized

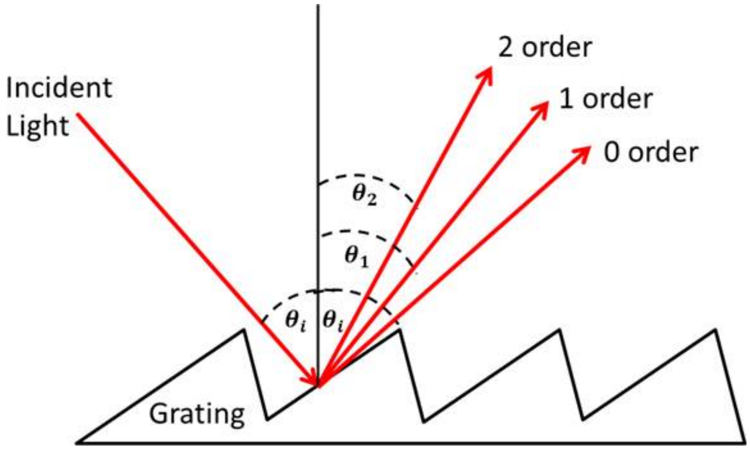

Figure 3.9: Sketch of a ruled and blazed diffraction grating.

with the grating equation [43],

$$sin\theta_i + sin\theta_r = \frac{m\lambda}{d}, \quad m = 0, \pm 1, \ \pm 2 \ldots \tag{3.2}$$

where θ_i and θ_r are the angles between the incident and reflected rays to the the grating, m is the diffraction order, d is the groove spacing, and λ refers to the incident wavelength. This equation shows that multiple orders can occur, and that at $m = 0$ the angle of incidence is equal to the angle of reflection and the grating behaves like a mirror.

Often ruled gratings are blazed at specific angles, forming saw tooth patterns, as depicted in Figure 3.9. This angle corresponds to a blaze wavelength at which the efficiency of the grating reaches its peak. A blaze wavelength of 500 nm was chosen for the ruled gratings in this experiment in order to maximize the collection efficiency in the visible spectrum.

For high resolution measurements, holographic, rather than ruled, gratings, are often used. They are formed by imprinting an interference pattern on a photosensitive material. This creates a sinusoidal patterned surface and very high density grooved gratings can be produced using this method. However, the efficiency of these gratings is typically worse when compared to ruled gratings [41]. For the magnetic field measurements a high resolution was required to measure the spectral line splitting. As a result a 2400 groove/mm holographic grating, optimized for visible wavelengths, was chosen.

3.5.1 Fiber Array Setup

In order to spatially resolve the spectroscopic measurements, a 150 mm achromatic lens imaged the diode anode plasma onto the fiber array. The array was oriented at 45 degrees to the diode as shown in Figure 3.10. The lens coupled fiber array was placed on a stage that allowed for the rotation and translation of the array to account for jitter in the diode alignment. The distance from the anode surface that the array images depends on the fiber alignment. The edge of the fiber array is aligned to the anode surface and this axial alignment is accurate to within about 0.25 mm.

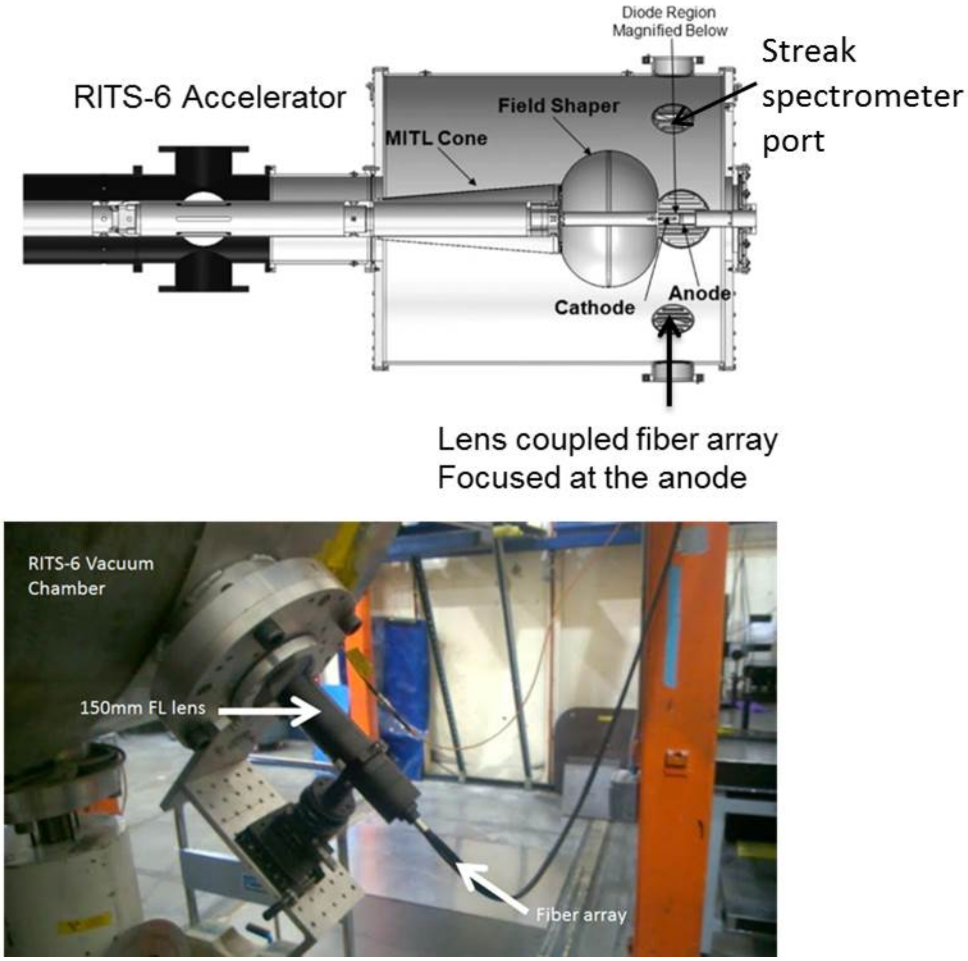

Figure 3.10: Top: RITS-6 Accelerator with the location of the fiber array [5]. Bottom: Photograph of the lens coupled array on the accelerator

Two different fiber arrays were used in these measurements. The single row array, in Figure 3.11, imaged the majority of the SMP diode experiments, and it consists of a single row of 11, 200 μm fibers. Each fiber was imaged to a 1 mm spot diameter and so the total length of the focused array was about two centimeters long at the anode. This was positioned so that about 1 cm was on either side of the beam axis. In order to align this array to the SMP diode, the fibers were backlit with a neon or bright LED light source, the lens coupled array was rotated so that Fiber 6 (out of 11 fibers) was centered on the cathode, and the array was then translated to the anode. Since the cathode has a smaller diameter than the anode, the array is more tightly focused at the cathode edge than at the anode edge, and consequently it is easier to adjust the positioning relative to the cathode.

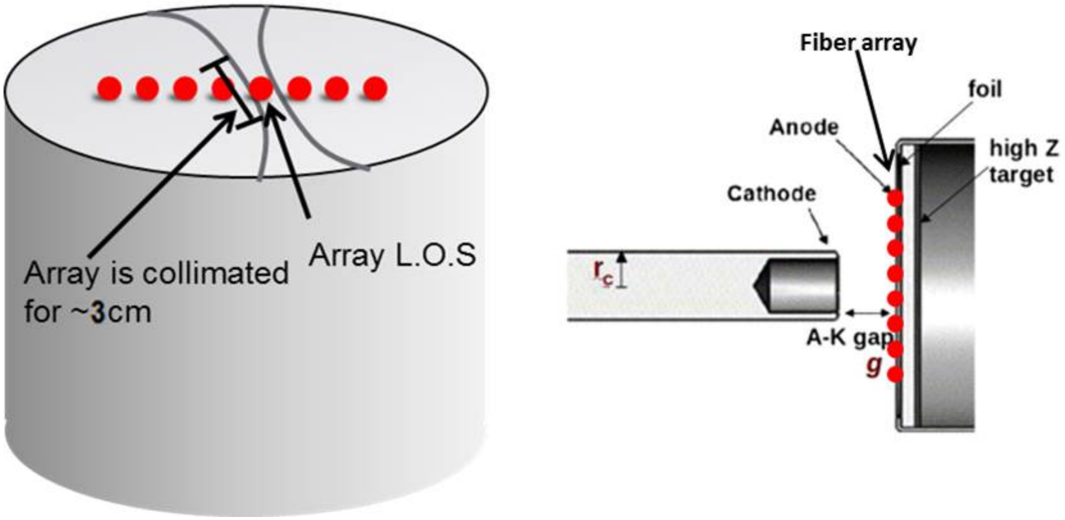

Figure 3.11: Left: Perspective view of the region imaged onto the single row fiber array. Right: Side view of the diode with the focused fibers (Figure from [5]). For clarity only 8 fibers are shown.

The double fiber array has an additional row of fibers that extend further into the AK gap, pictured in Figure 3.12. This array contains 13, 100 μm fibers in each row, resulting in 26 spectra per shot. The two rows are arranged into a single row at the spectrometer input. In addition, between each of these fibers is another 100 μm fiber. These fibers can connect to avalanche photodiodes (APDs) to monitor light emission as a function of time across the SMP diode. Additionally, two fibers on either side of the array measure the Cherenkov signal during the radiation pulse. One of these fibers can connect to an APD and the other connects to the spectroscopy array. This is useful for determining how much of the continuum is due to fiber scintillation from x-ray emission.

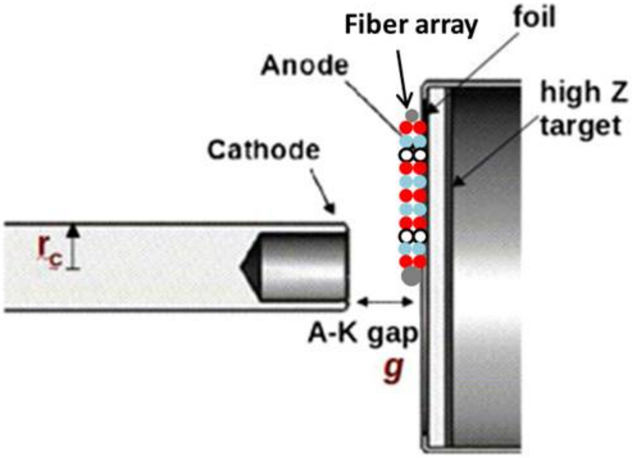

Figure 3.12: The double row fiber array. Only a few fibers are shown here for clarity. In total there are 52 fibers. 26 go to the spectrometer (red), 24 can connect to APDs (blue), and two are the Cherenkov fibers (grey). The white spots are spacing fibers used to extend out the array, and between these fibers are an additional 16 rows of alternating APD and spectroscopy fibers.

Except for the 200 μm Cherenkov fiber that connects to the spectrometer, these fibers have a diameter of 100 μm, and were imaged to a 0.5 mm diameter across the anode with a 150 mm focal length (FL) lens. The length of the focused array was only 13.5 mm, about half the size of the single row array. As a result, the double fiber array was focused by backlighting the bottom APD fiber in Figure 3.12, aligning it to the cathode axis, and translating it to the anode. This meant that the bottom spectroscopy fiber was usually just off the beam axis. Unfortunately, this configuration does not reveal the symmetry of the field measurements that the longer array shows, but it was necessary to prevent continuum from dominating half or more of the array.

The fibers (manufactured by Polymicro Technologies$^{\text{TM}}$) in both arrays have a standard numerical aperture of 0.22 and a high OH silica core in order to maximize UV-VIS transmission. Because the fiber arrays have a finite positive diameter they can accept light that is outside the calculated object distance of the lens. And since dopants have not been added in localized regions for these initial shots, the collected spectra are assumed to be line integrated.

3.5.2 Streak Spectrometer System

In a streak camera system, shown in Figure 3.13, in light passes through a slit and is focused to a narrow line at the photocathode. The emitted electrons travel through two sweep electrodes which apply strong electric fields to deflect the electrons. These electrons then hit a microchannel plate (MCP) which amplifies the signal according to the set gain. A phosphor screen converts the amplified signal into an optical image, and a CCD camera reimages the screen [44]. In the case of a streak spectrometer, the incident light on the streak camera contains spectral, rather than spatial, information.

The streak spectrometer system used on RITS-6 is a 0.5 m SpectraPro 500i Czerny-Turner spectrometer [45] with a 150 g/mm grating, coupled to a streak camera (NSTec Model L-CA-24). Two HeNe lasers, one at 532 nm and the other at 632.8 nm were connected to the spectrometer with a fiber optic cable. The laser light, after exiting the spectrometer, was imaged onto the streak camera, and was intense enough to streak. The two lines were then used to calibrate the wavelength of the streaked spectra. Since the laser lines have a sub-angstrom line width, they can also characterize the instrument resolution, as the line broadening of the line will be due entirely to the instrument. Using a spectrometer slit width of 100 μm, the system gave a 1.5 nm resolution, determined from the width of a HeNe laser line. The streaked spectra in this thesis have not been calibrated for relative intensity and are therefore only useful for line identification and timing purposes.

Comb and impulse signals, produced by two 800 nm lasers, determine the timing of the image. Comb fiducials consist of a column of points, with each point separated by about 10 ns. The impulse signal appears as a bright spot along the combs in the streaked spectra

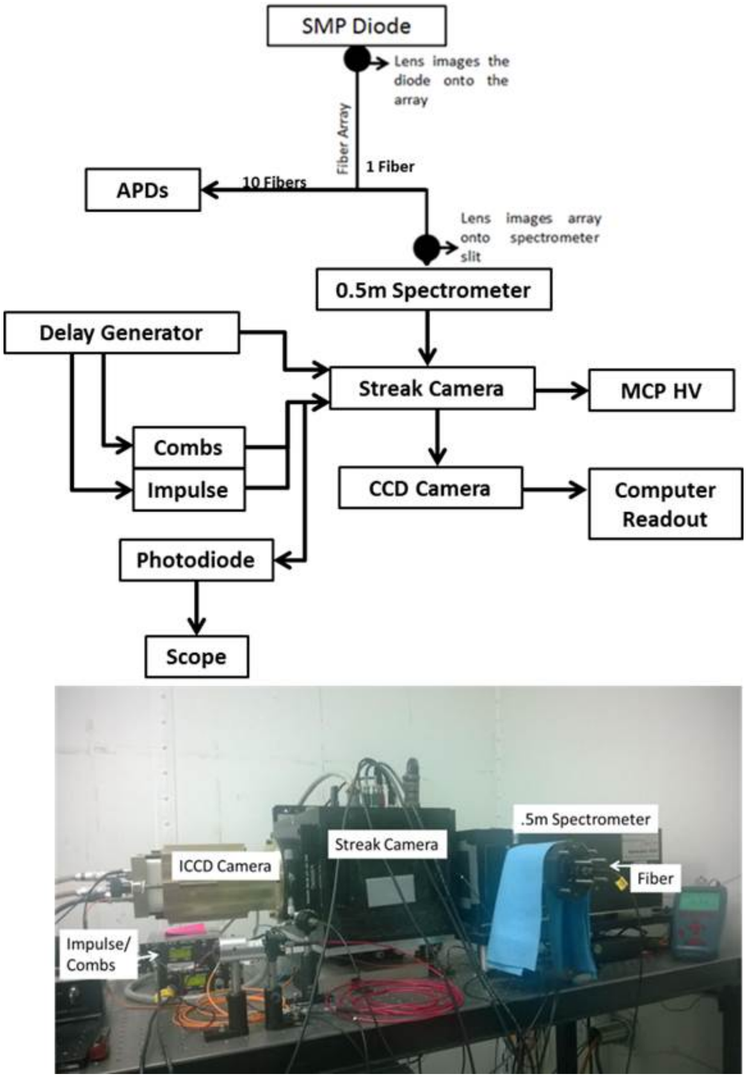

Figure 3.13: Top: Block diagram of the streaked spectrometer setup. Bottom: streak camera system photograph.

and locates the streaked spectrum in time with regards to the start of the radiation pulse, once cable delays have been accounted for. The combs are used to determine the temporal linearity of the streak image and track the timing along the image.

In these experiments, the laser output from the comb and impulse generators were split using a fiber optic splitter, and half the laser light was sent to a photodiode and recorded on a scope, while the other half was coupled into the streak camera. A delay generator triggered the streak sweep, comb, and impulse. The CCD was gated for 0.1 seconds during the shot, while the MCP gain was held constant at about 650 V, and the sweep duration was set to 240 ns. A single fiber from a 200 m, 11 fiber array, was focused to a 1 mm diameter across the anode, using the same optics outlined in Section 3.5.1. This fiber also looked along a chord across the anode using a top port on the RITS vacuum chamber, marked in Figure 3.10. Fiber 4, located about 4 mm from the axis (with Fiber 6 on the beam axis), was typically coupled into the system, in order to obtain strong spectral lines that are not dominated entirely by continuum.

3.5.3 Time Gated Spectroscopy Setup

The experimental configuration for the time gated spectroscopic measurements in this thesis consisted of either a single or double row fiber array, discussed in Section 3.5.1, which imaged the SMP diode anode surface plasma. An achromatic lens pair focused the fiber array output onto a spectrometer slit. The spectrometer was coupled to a time gated Intensified Charge Coupled Device (ICCD) camera, as shown in Figure 3.14. The scope monitored the ICCD output for timing purposes.

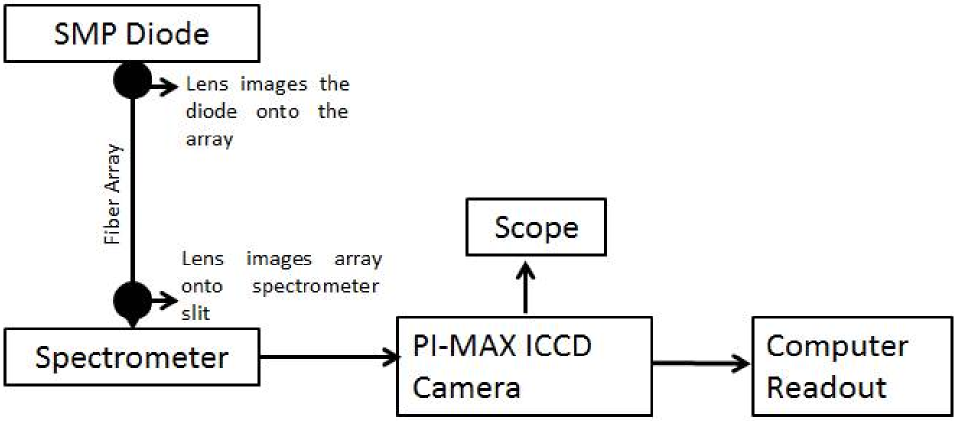

Figure 3.14: Block diagram of the setup for time gated spectroscopic measurements.

Initially, a low resolution Czerny-Turner spectrometer (Princeton Instruments SP-2150) with a focal length of 0.15 m and an aperture ratio of f/4.0, was fielded in order to characterize the plasma in the diode and identify spectral lines that may be useful for Zeeman splitting measurements. With a 150 g/mm grating and 50 μm spectrometer slit width this spectrometer had a resolution of about 5 nm, as determined from a mercury calibration lamp. The spectrometer setup is shown in Figure 3.15.

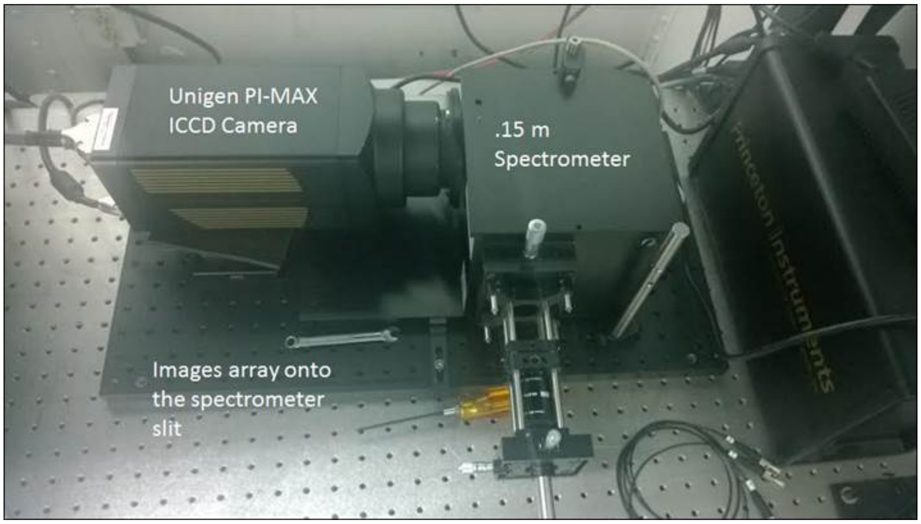

Figure 3.15: Low resolution spectrometer setup.

Light that enters through the entrance slit is separated into wavelengths by a ruled diffraction grating. A collimating mirror turns the beam, and in this particular spectrometer, a toroidal focusing mirror corrects for some of the astigmatism due to the optics. The light is then focused to a plane and imaged with an ICCD camera. Due to the relatively poor spectral resolution and small f-number a wide spectral range and large signal to noise ratio is obtained using this setup.

For high resolution spectroscopy (<0.1 nm), required for measuring Zeeman splitting, the IsoPlane SCT-320 with a 2400 g/mm grating was used. Typically, this setup, presented in Figure 3.16, generates a resolution of about 0.065 nm. The spectrometer is a Schmidt-Czerny-Turner, and it reduces some of the image aberrations that occur in a standard Czerny-Turner spectrometer, such as spherical aberrations, coma effects, and astigmatism [46]. These corrections increase the effective resolution of the spectrometer.

For the first spectroscopy shot run, each of the Al-MgF2 coated mirrors and gratings had an approximately 87% reflectivity. The second run used a silver coating instead. The silver coating improves the reflectivity per mirror and grating by about 10% [45], and increases

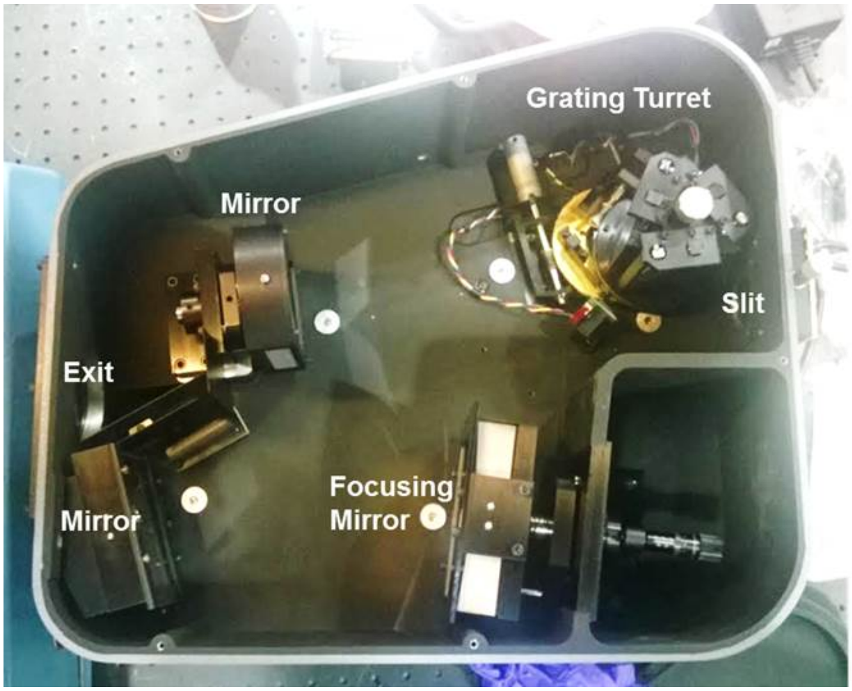

Figure 3.16: The IsoPlane 320 spectrometer.

the total light throughput by about 50% within the 500-600 nm wavelength window.

3.6 SMP Diode Spectrum Calibration and Corrections

3.6.1 Wavelength Calibration

Spectral data needs to be calibrated for the wavelength and the detectors spectral response. In order to calibrate the wavelength a gas discharge tube spectrum was taken on every shot. These tubes contain gases and metal vapors which produce distinct, narrow lines. Due to their low electron densities and temperatures the width of these lines is limited by the spectrometer slit width, grating, and detector resolution.

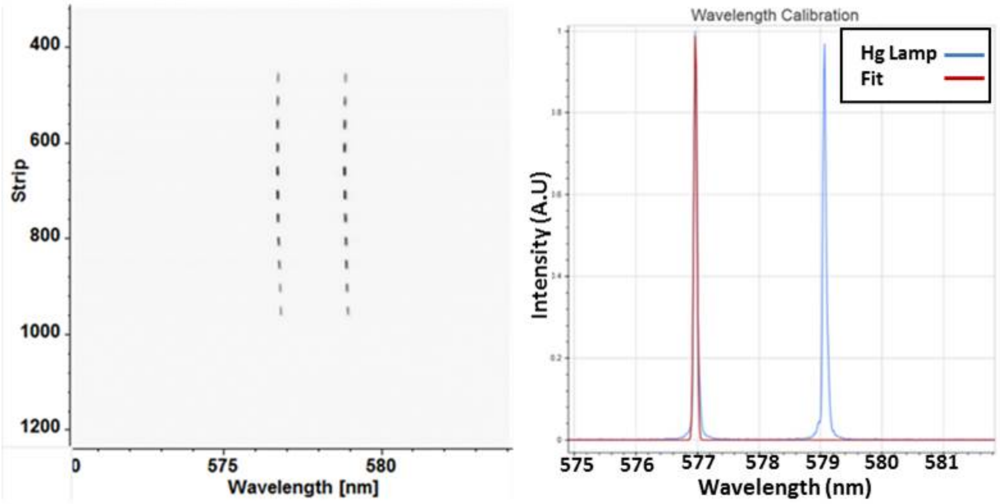

Figure 3.17: Left: Hg calibration lamp raw spectrum with a spectrometer slit width of 50um. Right: Hg spectrum lineout (blue) fit with a Gaussian profile (red).

An example from a mercury tube spectrum, using a high resolution (0.32 m focal length, 2400 g/mm grating, 50 um slit width) spectrometer, is given in Figure 3.17. In this configuration the spectrometer has a resolution of about 0.065 nm. In addition, the known Hg I lines at 576.96 and 579.07 calibrate the wavelength for this shot.

3.6.2 Intensity Calibration

All cameras have varying responses with wavelength. For these experiments PI-Max cameras were used with two different coatings. The quantum efficiencies for these coatings are plotted in Figure 3.18 [47]. The quantum efficiency is a measure of the percentage of incident photons that are converted to electrons in a CCD camera. For the initial spectroscopy run on RITS-6 an ICCD camera with a Unigen II coated photocathode, which extends into the infrared and ultraviolet wavelengths, was used. Later runs, however, used an HBf coated ICCD photocathode to maximize the efficiency of light collection in the visible spectral range.

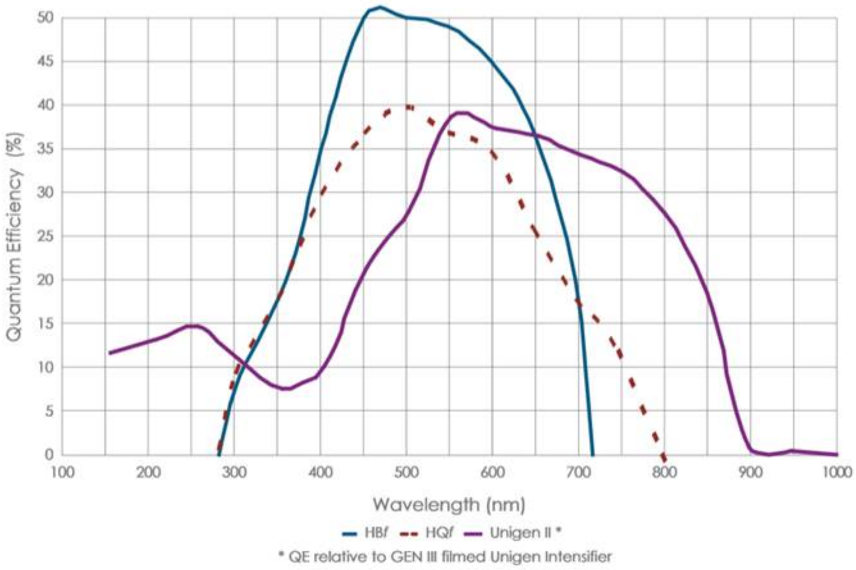

Figure 3.18: Princeton Instruments response curves for different ICCD camera coatings [47]

Calibration of the spectral response of the camera is required for an accurate measurement of the electron temperature and is also needed to assess the optical depth of the plasma. A tungsten calibrating lamp, pictured in Figure 3.19, with a known radiance across the visible spectrum was used to calibrate the response of the ICCD cameras.

This lamp consists of a hollow sphere that scatters light from a tungsten source. Multiple reflections within the sphere result in a uniform light source at the output. Preferably, this calibration would use the same gate width as typically used on an actual shot. However, for these experiments the ICCD was gated for only about 10-15 ns, which is too short to obtain enough signal from this type of blackbody calibration source. Therefore, the lamp

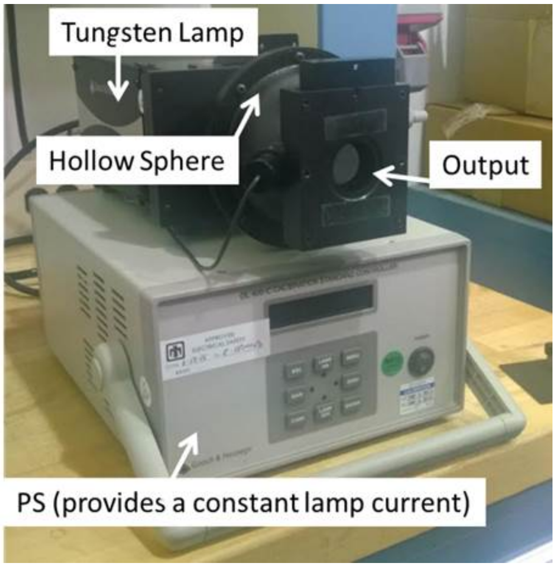

Figure 3.19: Tungsten calibrating lamp using an integrating sphere. This is used to calibrate the spectral response of the ICCD camera

was gated for about 5ms.

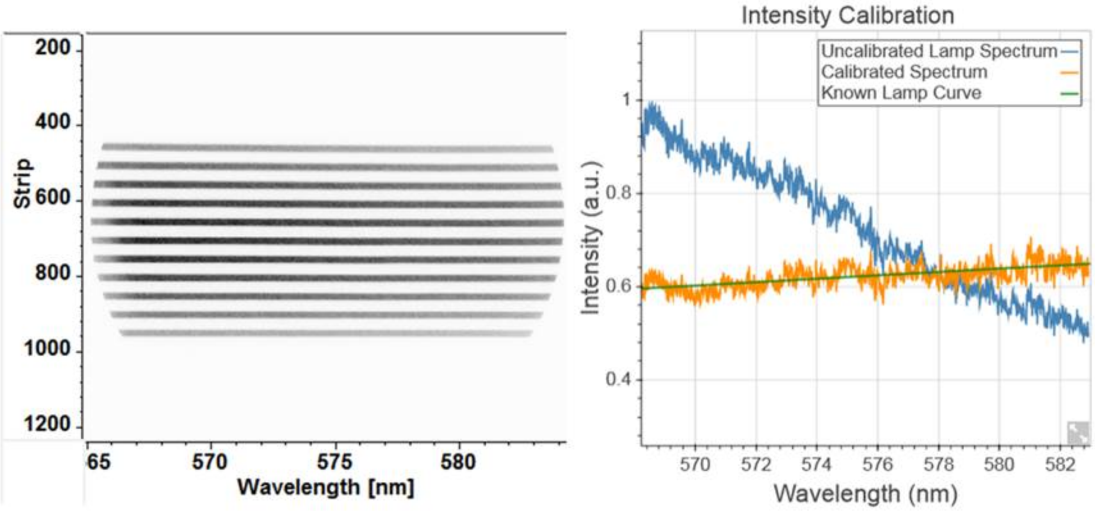

Figure 3.20: Left: Raw spectrum from the tungsten calibrating lamp. Left: Uncalibrated linout of fiber 5 (blue) and the spectrum corrected for shape (orange)

The fiber array was focused to the lamp output using the same optics as those used on an actual shot and the resulting spectrum was calibrated to match the shape of the lamp radiance, shown in Figure 3.20. These factors are then used to calibrate the shot data. Although this lamp can also be used to calibrate for absolute intensity by accounting for the exposure time and intensifier gain settings, only the spectral shape was calibrated in this thesis.

The calibration procedure is applied to data from Shot 1920, shown in Figure 3.21. The Unigen PI-Max camera has a steep intensity decay with increasing wavelength in this spectral range, also apparent in Figure 3.20. The intensity calibration procedure adjusts the sharp decrease in intensity with wavelength and reflects a much more accurate continuum shape which should be relatively flat over the 20 nm wavelength window.

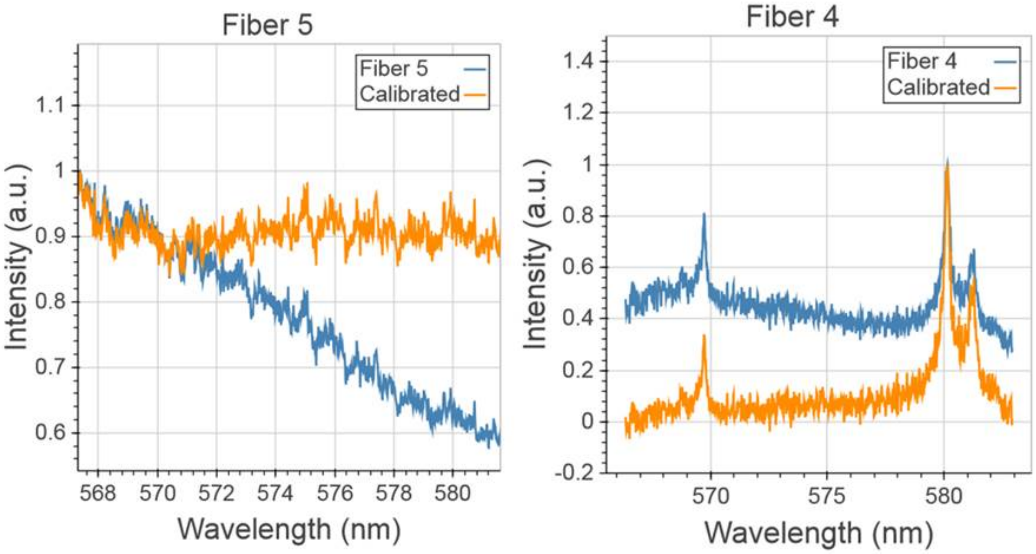

Figure 3.21: Normalized intensity calibration for Shot 1920 on a fiber 1.1 mm from the beam axis (Fiber 5) and 3.1 mm from the axis (Fiber 4)

3.6.3 Fiber Position

It is difficult to align the fiber array so that the center fiber of the array is always on the electron beam axis for several reasons. The beam can move and is not always centered on the anode plate. Initially, the array was aligned by eye. Later shots also used a digital video camera positioned on the bottom of the RITS vacuum chamber, 45 degrees to the array. This enabled a more precise positioning of the fiber array with respect to the anode.

The radial location of each fiber must be known in order to determine the current density within the diode. The central ten pixels on each fiber spectrum within the red bars in Figure

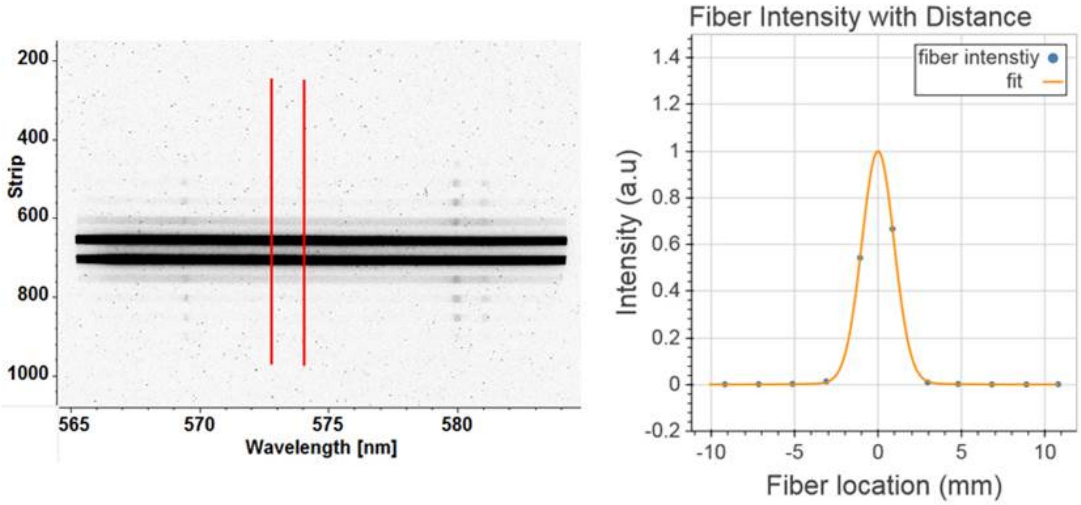

Figure 3.22: Left: Raw spectra with red lines to represent the lineout region. Right: Average intensity of each fiber in the ROI fit with a Voigt profile.

3.22 are averaged and plotted as a point. This lineout is then fit with a Voigt profile, which fits the data better than a standard Gaussian profile. The peak of this profile is considered to be the beam axis. For the 200 μm single row array, each fiber is imaged to a 1 mm diameter circle at the anode surface, and so the resulting radial position of the measurement is associated with a ± 0.5 mm error. Similarly, for the 100 μm array, the radial error is estimated to be ± 0.25 mm. For Shot 1920 in Figure 3.22 the beam axis is between the two central fibers, which is a common occurrence with this array alignment technique and the continuum falls off rapidly with distance from the axis.

However, this is only an approximation for the plasma intensity distribution. X-ray source spot size measurements using a time integrated camera, suggest that the source is not a simple Voigt or Gaussian distribution, and often times it is not perfectly symmetric. Additionally, as will be discussed in later chapters, these measurements of relative intensity are still line-integrated across a chord. To obtain a measurement of the intensity as a function of radius an Abel inversion of the data needs to be performed.

Typically, the fit to the fiber array has a larger FWHM than the spot measurements, since the anode plasma is excited by both the electron beam, close to the axis, and thermally, further from the axis. Still, for simply determining the beam axis, this is a reasonable method, since the intensity of the continuum should scale with distance from the axis, and the bright continuum on the central fibers is likely due to a dense plasma caused by the electron beam impact at the target surface.

3.6.4 Depth of Field

Depth of field is defined as the distance between two objects that appear on the detector in acceptable focus. A point source that is not on the object plane of the lens will be imaged with some diameter. This diameter is called the circle of confusion (CoC). In these spectroscopy measurements, a single point within the anode plasma at a defined distance cannot be imaged alone since the CoC is the diameter of the fiber.

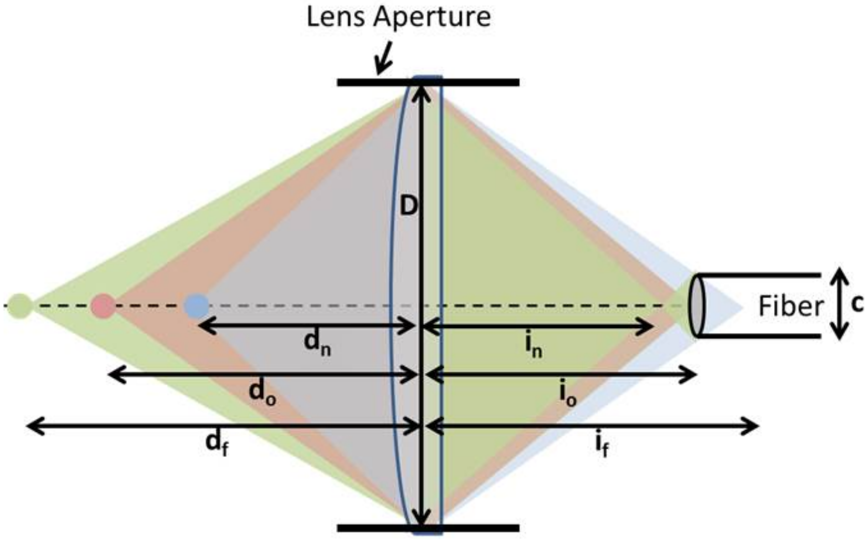

Figure 3.23: The light collection of an optical fiber due to the depth of field of the lens.

As shown in Figure 3.23 and Figure 3.11, there is a spatial range from which light can enter the fiber. This effect, can be quantified using the thin lens equations to estimate the lens depth of field [48]. The thin lens equation is:

$$\frac{1}{f} = \frac{1}{d_o} + \frac{1}{i_o} \rightarrow i_o = \frac{d_o f}{d_o - f} \tag{3.3}$$

Where f is the focal length of the lens, d_o is the object distance (the anode location), and i_o is the image distance (the fiber optic location). Likewise, for the far and near limits of the depth of field,

$$i_f = \frac{d_f f}{d_f - f}, \quad i_n = \frac{d_n f}{d_n - f} \tag{3.4}$$

From the ratios in Figure 3.23,

$$\frac{D}{i_f} = \frac{c}{i_o - i_f}, \quad \frac{D}{i_n} = \frac{c}{i_n - i_o} \tag{3.5}$$

where c is the circle of confusion, and D is the aperture for the lens. From these equations the far and near depth of field can be estimated.

$$s_f = \frac{D d_o f}{D f - c(d_o - f)}, \quad s_n = \frac{D d_o f}{D f + c(d_o - f)} \tag{3.6}$$

The aperture for these measurements is essentially the same as the diameter of the lens, 50 mm. The lens focal length is 150 mm, and the CoC is 200 μm for the single row fiber array. This results in a depth of field of about ± 1.7 cm from the object plane. As a result, light is collected across a chord of about 3.4 centimeter across the anode surface, and any spectral analysis has to account for the additional contribution of light along this chord. Although the depth of field is relatively large for the 200 μm array, in practice there is very little light outside the extent of the fiber array, and so the spectra from the fibers are assumed to be line-integrated along 2 cm chords. For the 100 μm double row fiber array the depth of field is ± 0.8 cm.

3.6.5 Abel Inversions

As discussed in Section 3.6.4 and shown in Figure 3.23, each fiber in the array collects light along a chord across the anode. As a result, the measured spectra contain integrated intensities along this line of sight. Figure 3.24 is a simplified representation of intensity gradients along a chord.

Chords close to the axis contain larger density, temperature, and intensity gradients.

Additionally, the curved field lines result in multiple magnetic fields and directions along the fiber line of sight. Qualitatively, because fibers close to the axis view more perpendicular to the magnetic field, they will have higher pi/sigma ratios. However, in order to calculate this ratio and deconvolve the spectrum, the relative intensity of a spectral line must be estimated as a function of radius. As long as the quantity being assessed is cylindrically symmetric and there are several chordal line integrated measurements, the radial distribution can be determined using a procedure known as Abel inversions. This procedure is described in depth in [10] and summarized here.

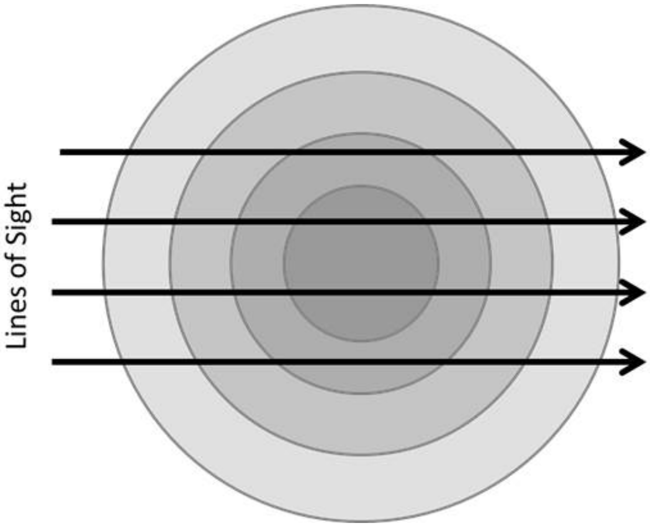

Figure 3.24: Simplified sketch of the radial intensity gradients along the fiber array lines of sight.

A cylindrically symmetric, line integrated value, such as the intensity in the SMP diode, can by quantified using the Abel transform,

$$I(y) = \int_{-\sqrt{a^2-y^2}}^{\sqrt{a^2-y^2}} i(r)\,dx \tag{3.7}$$

where $I(y)$ is the line integrated intensity, and $i(r)$ is the local radial intensity. In cylindrical coordinates,

$$I(y) = 2\int_{y}^{a} \frac{i(r)r}{\sqrt{r^2-y^2}}\,dr \tag{3.8}$$

The inverse of this gives $i(r)$ as a function of the line integrated intensity measurement.

$$i(r) = -\frac{1}{\pi}\int_{r}^{a}\frac{dI}{dy}\frac{1}{\sqrt{y^2-r^2}}\,dy \tag{3.9}$$

where y is the direction across the fiber array, r is the radial distance from the axis, and a is the radius, clarified in Figure 3.25.

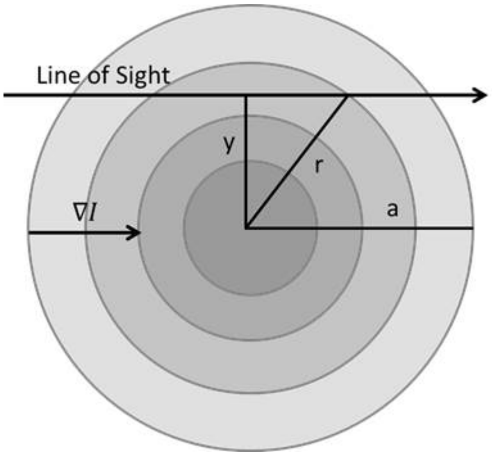

Figure 3.25: Geometry of the Abel inversion along a fiber line of sight.

Using the same procedure outlined in Section 3.6.3, a vertical lineout is taken across the array of fibers. The vertical lineout is taken along the spectral line rather than the continuum and unlike the continuum intensity which quickly drops to zero, line emission is often visible even at the edge of the array. Additionally, the continuum is subtracted from the line in order to obtain more accurate estimates of the relative line intensities. Once the Abel inversion has been performed on a dataset, these relative intensity values are used to weight the spectral profile calculations at discrete positions along the line of sight.

3.7 TRSD Measurements and Spot Size

The x-ray source spot size measurements are calculated by Dr. Timothy Webb, using the Time Resolved Spot Diagnostic (TRSD) [49]. The TRSD consists of a scintillating fiber array of 84 plastic fibers with a 2.7 ns response time. This is placed behind a tungsten rolled edge, which occludes a portion of the x-rays. The fibers are coupled to a streak camera and lineouts are taken across these fibers to obtain an edge spread function (ESF). A sketch of the TRSD and the raw data are shown in Figure 3.26

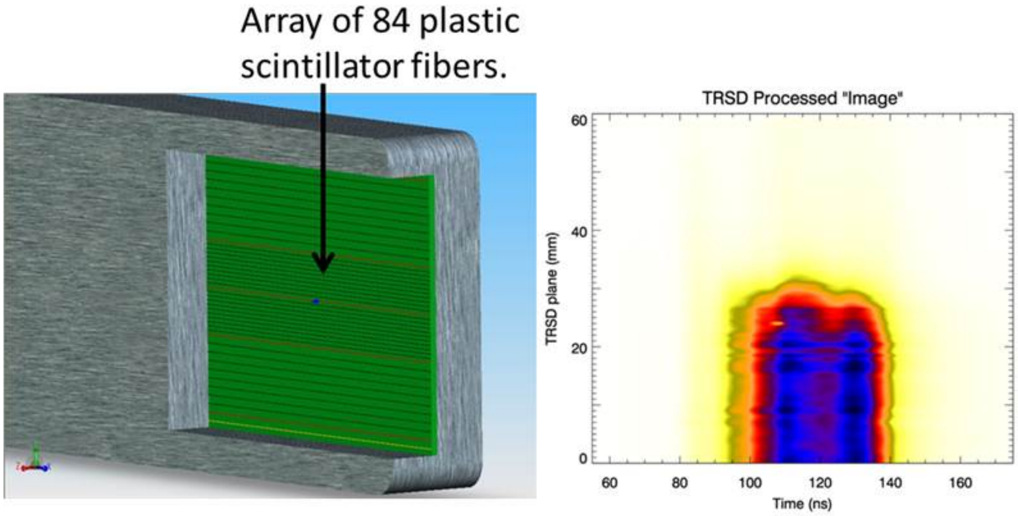

Figure 3.26: TRSD diagnostic (left). The scintillating fibers are coupled to a streak camera. A vertical line-out of the resulting image (right) gives the ESF, and the horizontal line-out gives the radiation pulse. Images are from T. Webb.

There are several definitions for the x-ray spot size. The Atomic Weapons Establishment (AWE) spot size, for instance, referenced in Figure 5.19, assumes a uniform disk source and is determined from taking the horizontal separation between 25% and 75% of the maximum of the ESF, multiplied by 2.5. Spot motion is determined from offsets in the ESF fit [50]. Typical AWE spot sizes are less than 3 mm in diameter for a standard SMP diode configuration. For a Gaussian spot profile, the AWE spot size is related to the Gaussian FWHM by [51]

$$d_{AWE} = 2.082\frac{FWHM}{2\sqrt{2}} \tag{3.10}$$

In Section 5.5 the C IV line intensity profile is fit to a Gaussian function in order to perform the Abel inversion. In contrast, the x-ray spot is more closely related to two superimposed Gaussian profiles [52]. One profile forms a narrow core, and the other forms the broad wings. However, the intensity of C IV, which is measured at diameters greater than

4 mm and is in the visible range, does not necessarily correspond to the x-ray spot intensity. Typically, the current density is estimated by assuming that all of the diode current, measured from the cathode B-dots, is enclosed within the AWE spot diameter. However, as will be shown in Section 5.7.2, this assumption diverges from magnetic field estimates from Zeeman split lines.

CHAPTER 4

Electron Density and Temperature Measurements on the SMP Diode

Characterizing the anode surface plasma can provide insight into the effect these plasmas have on the SMP diode dynamics. For instance, simulations [5, 53] suggest that the anode plasma is responsible for a falling impedance due to plasma expansion into the gap. The dense surface plasma may also cause the beam to defocus [7, 8] at the target. Several spectral lines will be analyzed in this chapter to determine electron temperature and density profiles. They are summarized in 4.1.

Electron densities can be determined from Stark broadening, a type of pressure broadening due to charged particles that produce an electric field near the radiator. The electric fields perturb the radiator in what is known as the Stark effect. The Stark effect, like the Zeeman effect, splits the atomic structure into additional energy levels. Since many perturbations of differing magnitudes occur due to the varying location of the charged, perturbing particles, the Stark effect results in line broadening rather than line splitting. Several methods have been developed over the past few decades to determine densities from the widths of various spectral lines. Due to the complexities of the Stark width calculations, calculated line shapes can often differ from other analytic models and experimental values, depending on the approximations used.

The semi-classical approximation [55], for example, assumes classical paths for the perturbing particles and quantum mechanical wave-functions and energy levels for the radi-

Table 4.1: Spectral lines analyzed in this section. Wavelengths and terms are from the NIST Atomic Spectra Database [54]. Although the H-alpha line consists of several lines, they are not individually resolved in these experiments.

Line	Wavelength (nm)	Term	
		Lower	Upper
H I (H-alpha)	656.28	$2^2\mathrm{S}_{1/2}$	$3^2\mathrm{P}_{1/2}$
		$2^2\mathrm{S}_{1/2}$	$3^2\mathrm{P}_{3/2}$
		$2^2\mathrm{P}_{1/2}$	$3^2\mathrm{S}_{1/2}$
		$2^2\mathrm{P}_{3/2}$	$3^2\mathrm{S}_{1/2}$
		$2^2\mathrm{P}_{3/2}$	$3^2\mathrm{D}_{5/2}$
		$2^2\mathrm{P}_{3/2}$	$3^2\mathrm{D}_{3/2}$
		$2^2\mathrm{P}_{1/2}$	$3^2\mathrm{D}_{3/2}$
		$1^2\mathrm{P}_{1/2}$	$3^2\mathrm{D}_{1/2}$
C IV	580.13	$3^2\mathrm{S}_{1/2}$	$3^2\mathrm{P}_{3/2}$
	581.198	$3^2\mathrm{S}_{1/2}$	$3^2\mathrm{P}_{1/2}$
C III	569.59	$3^1\mathrm{P}_1$	$3^1\mathrm{D}_2$
C II	657.81	$3^2\mathrm{S}_{1/2}$	$3^2\mathrm{P}_{3/2}$
	658.29	$3^2\mathrm{S}_{1/2}$	$3^2\mathrm{P}_{1/2}$
Al III	569.66	$4^2\mathrm{S}_{1/2}$	$4^2\mathrm{P}_{3/2}$
	572.273	$3^2\mathrm{S}_{1/2}$	$4^2\mathrm{P}_{1/2}$

ator. The semi-empirical [20] and modified semi-empirical [56] approximations use Gaunt factors to correct for quantum effects when the energy levels for a particular transition are not well known. However, these two methods do not take ion dynamics into account. More recently, in 1984, with the aid of computer simulations, ion motion was included in models to correct the theoretical line shape of the hydrogen Lyman lines [57]. Plotted in Figure 4.1 are estimates of Stark widths for an electron density of 10^{18} cm^{-3} for C IV and Al III from a few different investigations including PrismSPECT simulations, Yitzhak Maron's calculations, and several other methods.

Electron temperatures can be estimated by comparing relative line intensities of the same ion or subsequent ionization states. If Local Thermodynamic Equilibrium (LTE) is a valid approximation of the plasma, then the ratio of lines from the same ion is given by [19]

$$R = \frac{\lambda_{nm} A_{ki} g_k}{\lambda_{ki} A_{nm} g_n} exp\left(-\frac{E_k - E_n}{kT}\right) \tag{4.1}$$

where where n and k represent the upper levels, m and i represent the lower energy levels,

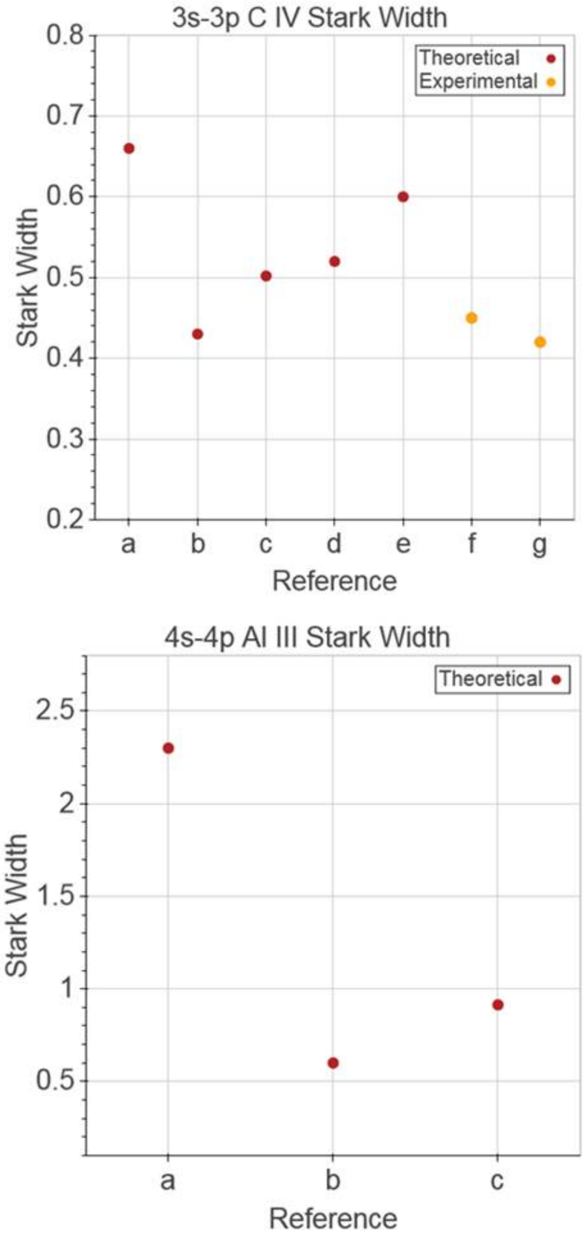

Figure 4.1: Figure 4.1 Top: C IV Stark width for electron density of 1×10^{18} cm^{-3} and electron temperatures of 6-6.3 eV. a: PrismSPECT width, b: Dr. Maron's calculation [58], c: [59] (ion effects are an order of magnitude less than electron impact widths and are not plotted), d: [60], e: [61], f: [62] (scaled linearly), g: [60]. Bottom: Al III Stark width for an electron density of 1×10^{18} cm^{-3} and electron temperature of 3 eV. a: PrismSPECT width, b: Dr. Maron's calculation [58], c: [63].

g is the statistical weight and A is the Einstein coefficient of the levels, E is the energy of the level, and T is the electron temperature. Since Equation 4.1 uses line ratios from the same ion or atom the energy separation between the upper levels is often small, and so the ratio may be a weak function of temperature. In order to increase the energy separation, the ratio of lines from subsequent ionization states can be used to determine the electron temperature [19]

$$R = \frac{\lambda_{nm} A_{ki} g_k}{\sqrt{\pi}\lambda_{ki} A_{nm} g_n} (4\pi N_e a_o^3)^{-1} \left(\frac{kT}{E_H}\right)^{3/2} exp\left(-\frac{E_n + E_\infty - E_k + \Delta E_\infty}{kT}\right) \quad (4.2)$$

where N_e is the electron density, a_o is the Bohr radius, E_H is the ionization energy of hydrogen, E_∞ is the ionization energy of the ion, and ΔE_∞ is a correction to this energy given by

$$\Delta E_\infty = 2zE_H a_o/\rho_D \quad (4.3)$$

The Debye length is represented by ρ_D, and a_o is the Bohr radius. The LTE approximation, however, is only valid for dense plasmas in which collisional processes dominate radiation processes, and this is a particularly difficult condition to meet for higher ionization states. A necessary but inadequate condition for LTE to be valid is given by the McWhirter criterion [64]

$$n_e(cm^{-3}) > 1.6 \times 10^{12} T^{1/2} (\Delta E)^3 \quad (4.4)$$

where T (in K) is the electron temperature, and ΔE (in eV) is the largest energy gap in the atom or ion, which for C IV is 29.5 eV. At an electron temperature of 6.1 eV, for instance, the density would have to be greater than 1.1×10^{19} cm^{-3} to meet this condition. A more precise determination of the validity of the LTE approximation can be found by using a collisional-radiative (CR) code. PrismSPECT, which solves rate equations for various atomic processes was used to calculate the CIII/CIV line ratio for an optically thin plasma. This ratio as a function of density is plotted in Figure 4.2 at 6.1 eV and compared with the LTE ratio calculated using Equation 4.2.

As determined from the C IV doublet width in Section 4.2.2, the electron densities range from about 1-5$\times10^{17}$ cm^{-3}. At 10^{18} cm^{-3} the non-LTE C III/C IV ratio, in 4.2 is about a factor of 3 larger than the LTE ratio. LTE is a valid approximation only at electron densities above 10^{19} cm^{-3}, which agrees with the McWhirter criterion. Consequently, the

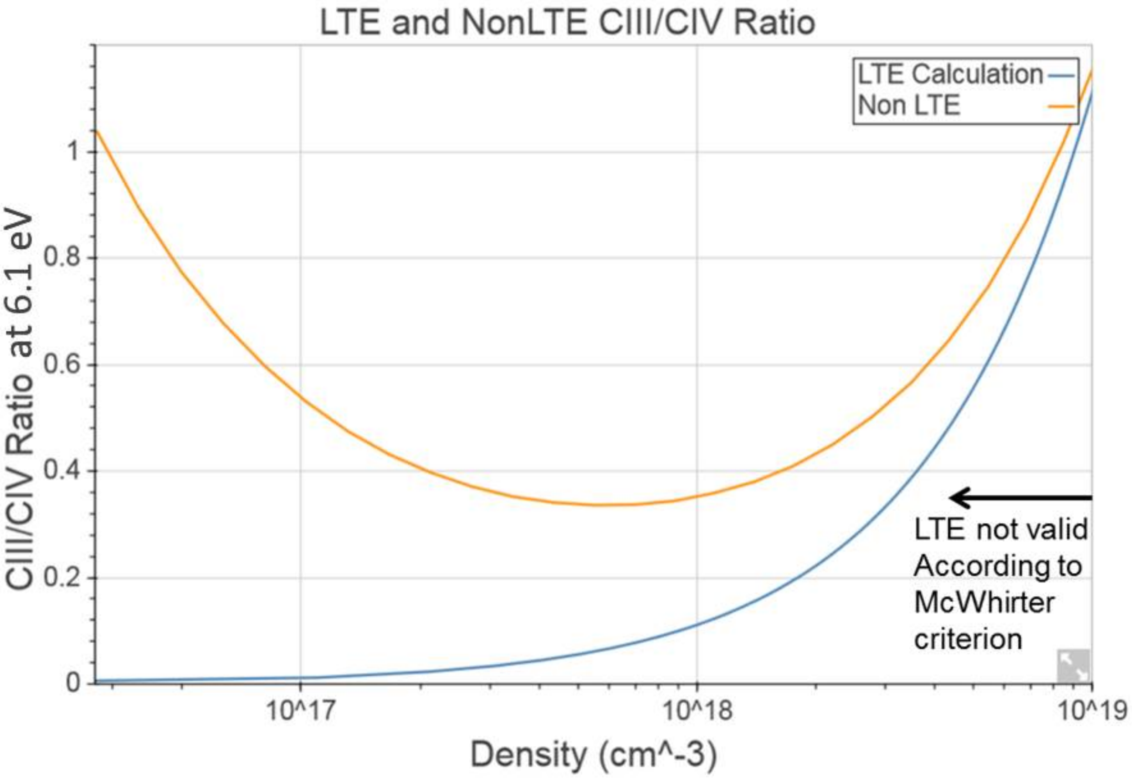

Figure 4.2: Non-LTE and LTE CIII/CIV ratio as a function of electron density at an electron temperature 6.1 eV.

LTE approximation is not used in this thesis to determine the electron temperature using the C III/C IV line ratio.

Due to the parabolic shape of the non-LTE C III/C IV ratio at 6.1 eV, an estimate of the electron density is required to determine the electron temperature. The electron density is calculated in Section 4.2 from the FWHM of the spectral line. These measurements, in conjunction with the measured C III/C IV ratio, are used to estimate the electron temperature. The C III/C IV ratios as a function of electron temperature for several densities are given in Figure 4.3.

4.1 SMP Diode Temperature Estimates

In order to determine electron temperatures, C IV and C III lines are fit with Voigt profiles, and the ratio of the two lines are compared to a PrismSPECT non-LTE, optically thin model for a pure carbon plasma. Line ratios as a function of temperature for several electron densities are shown in Figure 4.3.

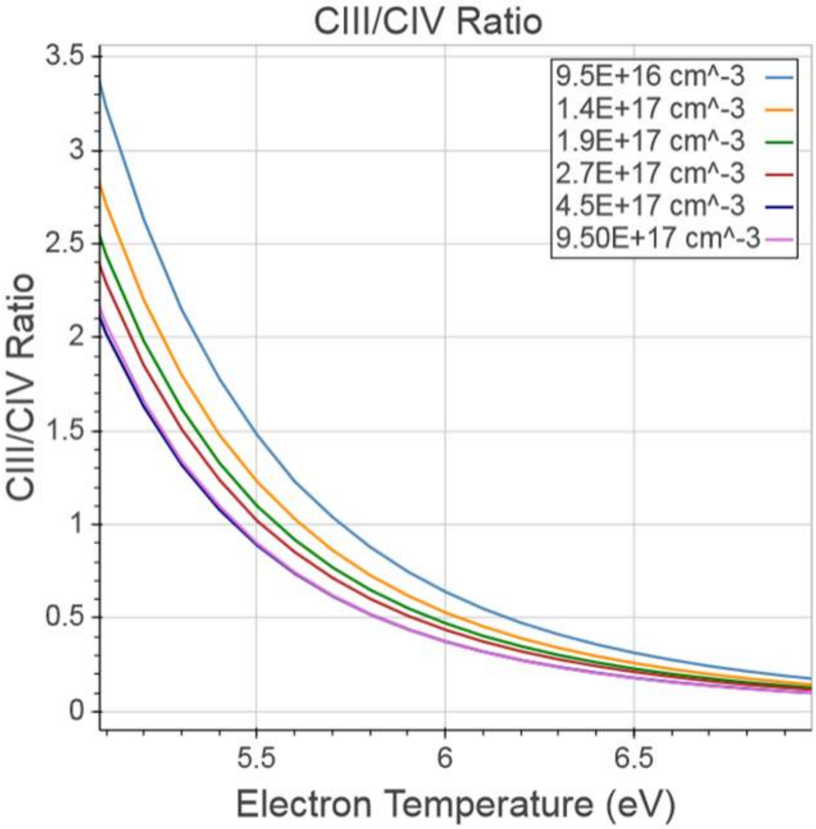

Figure 4.3: CIII/CIV ratio as a function of electron temperature calculated in PrismSPECT.

As mentioned in Chapter 3 the spectra represent an integrated measurement across the anode surface and the measured lines likely contain a gradient of temperatures and densities. As a result, temperature and density profile plots across the surface are measurements that are a function of the fiber position, which may not represent the radii at which the ions are present. One way to determine whether the C IV doublet and the C III line are from the same location is to estimate the electron density due to Stark broadening from the Lorentzian component of the fit for both lines. In a cylindrically symmetric plasma comparable densities would suggest that both lines are from ions located at similar radii. However, in this case the C III line is asymmetric close to the axis, as shown in Figure 4.4. Additionally, there are few experimental and theoretical tabulations for the Stark width of this line and they vary by up to a factor of 2.4 [65]. As a result, no attempt is made to determine the electron density from the C III line, and so the temperature estimates are from a 1 mm diameter chord across the anode, assuming a uniform plasma along the chord.

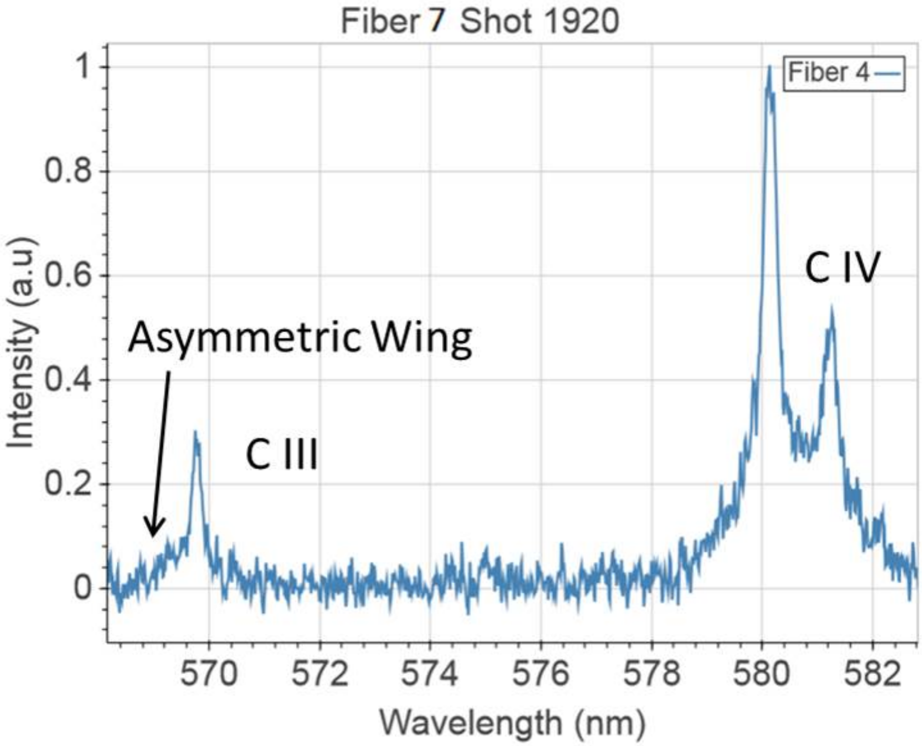

Figure 4.4: Spectrum from Fiber 7 on Shot 1920 which had a Si-coated tantalum converter. The C III line appears to be asymmetric.

Electron temperatures from Shots 1920, 1959, and 1960, summarized in Table 5.1, have been determined from the C III/C IV line ratio. The spectrometer ICCD was gated for 15 ns toward the middle of the current pulse. B-dot traces and gate timings are given in Figure 5.14. Shots 1959 and 1960 were standard SMP Al-foil shots, with the beam current rising from about 125 kA to 140 kA over the ICCD gate. Shot 1920 had a Si-coated tungsten convertor, with currents of 130-150 kA. The electron temperature profiles for the three shots are plotted in Figure 4.5.

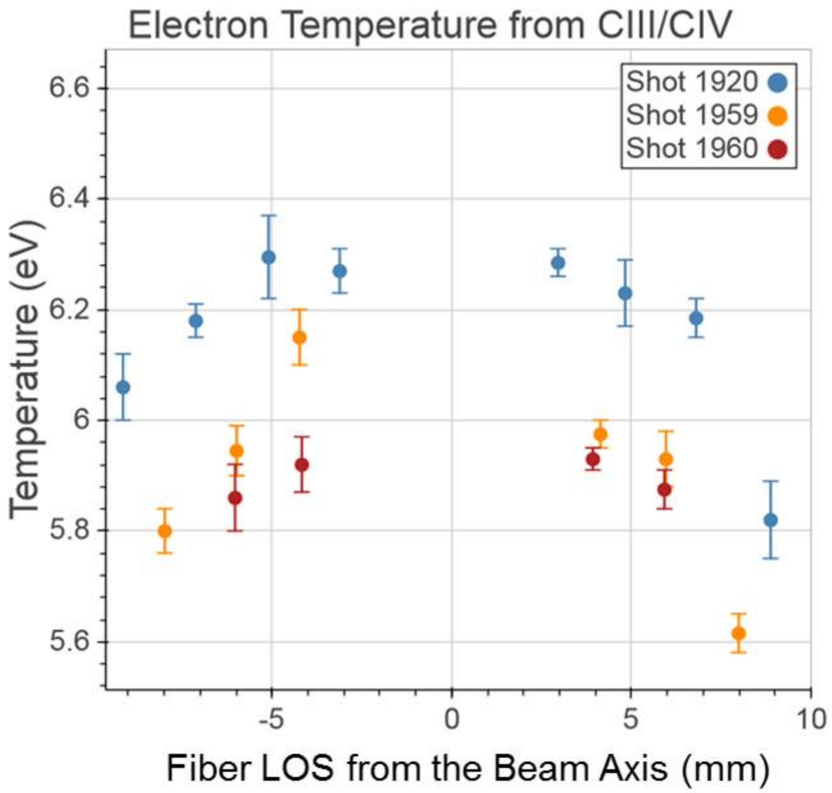

Figure 4.5: Electron temperature profiles for the SMP diode anode surface.

The electron temperature rises slightly toward the beam axis and is between about 5.6-6.2 eV for Shots 1959 and 1960 and about 5.8-6.4 eV for Shot 1920. It takes more time to thermally ionize the foil surface, which is offset from the convertor, and so it is reasonable that the foil surface is colder than the convertor surface. Additionally, Shot 1920 had slightly higher current measurements by the end of the spectrometer ICCD gate than 1959 and 1960. The errors in Figure 4.5 are determined from uncertainty in the density measurements, discussed in Section 4.2, and from the uncertainty in the intensity of the C III and CIV lines due to noise.

4.2 SMP Diode Electron Densities

4.2.1 Electron Densities from H-alpha at 656.28 nm

The Hα line at 656.28 nm is often used in Stark broadening density calculations because of its line strength and sensitivity to electron densities. Theoretical hydrogen line profiles have been calculated according to what is known as Griem's standard theory (ST) and the widths are tabulated in Griem's book [20]. The theory assumes an impact approximation for the electron field and a quasistatic approximation for the ion field. In the electron impact approximation the system is perturbed by weak collisions that occur on time scales that are short compared to the time between collisions. Additionally, the path of the perturbing particle is unchanged after the collision in this approximation. The quasistatic approximation assumes that the electric field produced by stationary ions is a constant perturbation [66]. The two effects occur independently in this model.

The tabulations assume a Maxwellian distribution for the perturbing electrons. LSP simulations suggest the SMP electron beam density is 3-4 orders of magnitude smaller than the surface plasma density [4]. Therefore a Maxwellian distribution should still be a valid approximation for the SMP diode. In Griem's tabulations [15] the Stark widths for the hydrogen lines are given using the reduced wavelength parameter, α,

$$\alpha = \frac{|\lambda - \lambda|}{F_o} = \frac{\Delta\lambda}{2.6eN_e^{2/3}} \tag{4.5}$$

where $\Delta\lambda$ is the wavelength shift from the center, N_e is the electron density, and F_o is the Holtzmark electric field. The FWHM of the Hα line is calculated from Griem's fractional intensity width ($\alpha_{1/2}$) using Equation 4.6 and is plotted in Figure 4.6. These tabulations are estimated to be accurate to within 10% [20].

$$\Delta\lambda_{fwhm}[nm] = 0.2(1.25 \times 10^{-9})\alpha_{1/2}(N_e[cm^{-3}])^{2/3} \tag{4.6}$$

The electron density, estimated from the Stark width of the spectral line, is weakly de-

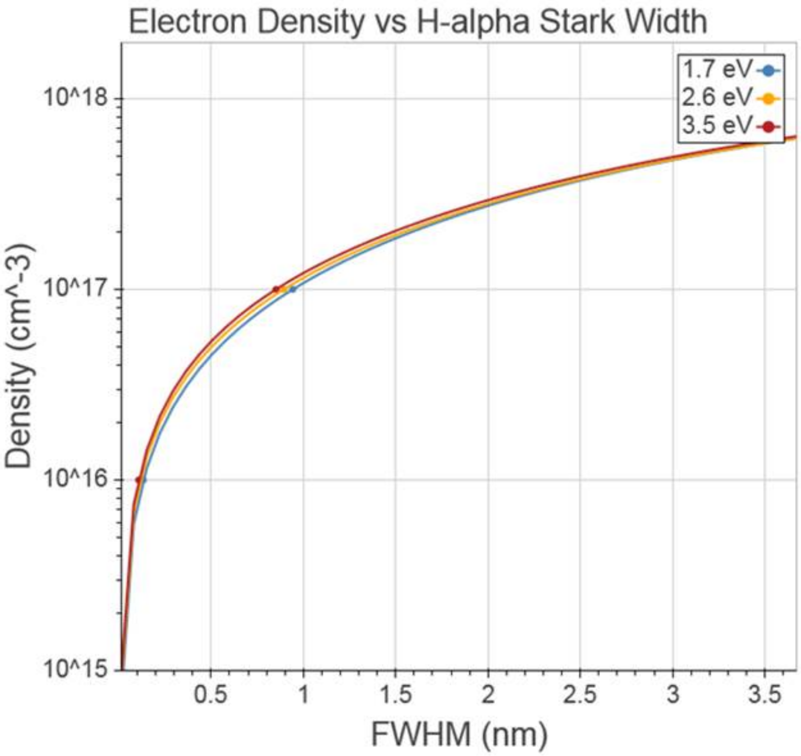

Figure 4.6: Electron density calculated using Griem's tabulations [15] as a function of FWHM of the H-alpha line.

pendent on temperature. For instance, a temperature range of 3-5.2 eV results in an error of about ± 5% (after extrapolating Griem's tabulations) for the H-alpha density measurements between 10^{16}-10^{17} cm^{-3}. This is much smaller than the error resulting from the fit, which can be as high as approximately ± 40%.

Measurements of the H-alpha line were taken using the IsoPlane SCT-320 with an 1800 g/mm grating, resulting in an instrument resolution of about 0.094 nm, determined by fitting Gaussian profiles to a neon calibration lamp spectrum as discussed in Chapter 3. The single row fiber array, with 11, 200 μm fibers, was used for all H-alpha measurements. At this resolution the H I line and C II lines are resolved, and so all three lines are fit with Voigt profiles. Figure 4.7 shows an example of a spectrum taken with this setup for Shot 1950, which had an Al-coated tantalum target.

As mentioned in Chapter 4, these measurements are integrated across the line of sight. Therefore multiple density regions form the spectrum. This effect is indicated by broad

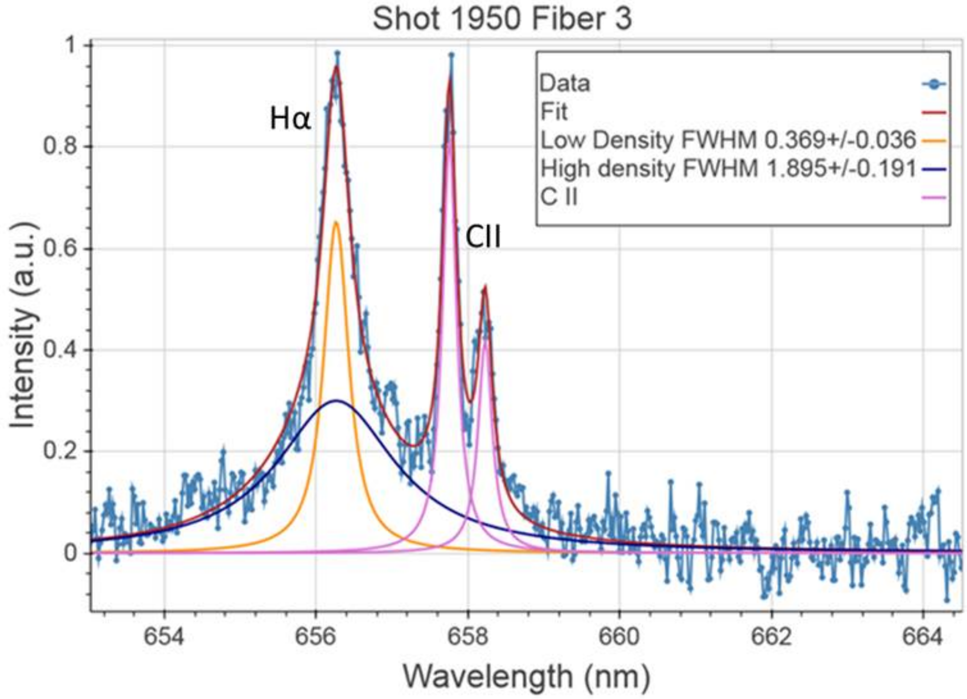

Figure 4.7: Spectrum from Shot 1950. H I is fit with two Voigt profiles to account for high (dark blue) and low (orange) density regions in the plasma. The C II lines are fit (purple) as well.

lower intensity wings that are superimposed onto narrower lines which reflect lower densities. The resulting line shape does not resemble a single Voigt profile, but rather, a combination of profiles. In actuality, there is a continuous range of densities across the line of sight, axially and radially. However, in this analysis, only two densities are approximated which would represent the average of a higher density and lower density region in the diode. In Figure 4.7, the high density component of the fit is shown with a dark blue curve. Figure 4.8 shows the electron density profile calculated from the H-alpha and CII lines for three shots. Figure 4.9 gives traces from the cathode B-dots which measure the beam current.

The electron impact parameters for C II at 658 nm have also been tabulated in Griem's work and are estimated to have an accuracy of $\pm 0.25\%$ [20]. Typical Stark widths of the C II line are between 0.2 and 0.45 nm for these measurements, corresponding to densities ranging from 2×10^{16} cm^{-3} to 4.6×10^{16} cm^{-3}, using tabulations at 3.5 eV. Due to the smaller

Stark widths of the C II lines and merged doublet lines, the higher density component of C II is not clear and therefore not included in the fit. Therefore, it is likely that the C II line and the lower density component of the H I line are from similar locations in the diode, as shown in Figure 4.8.

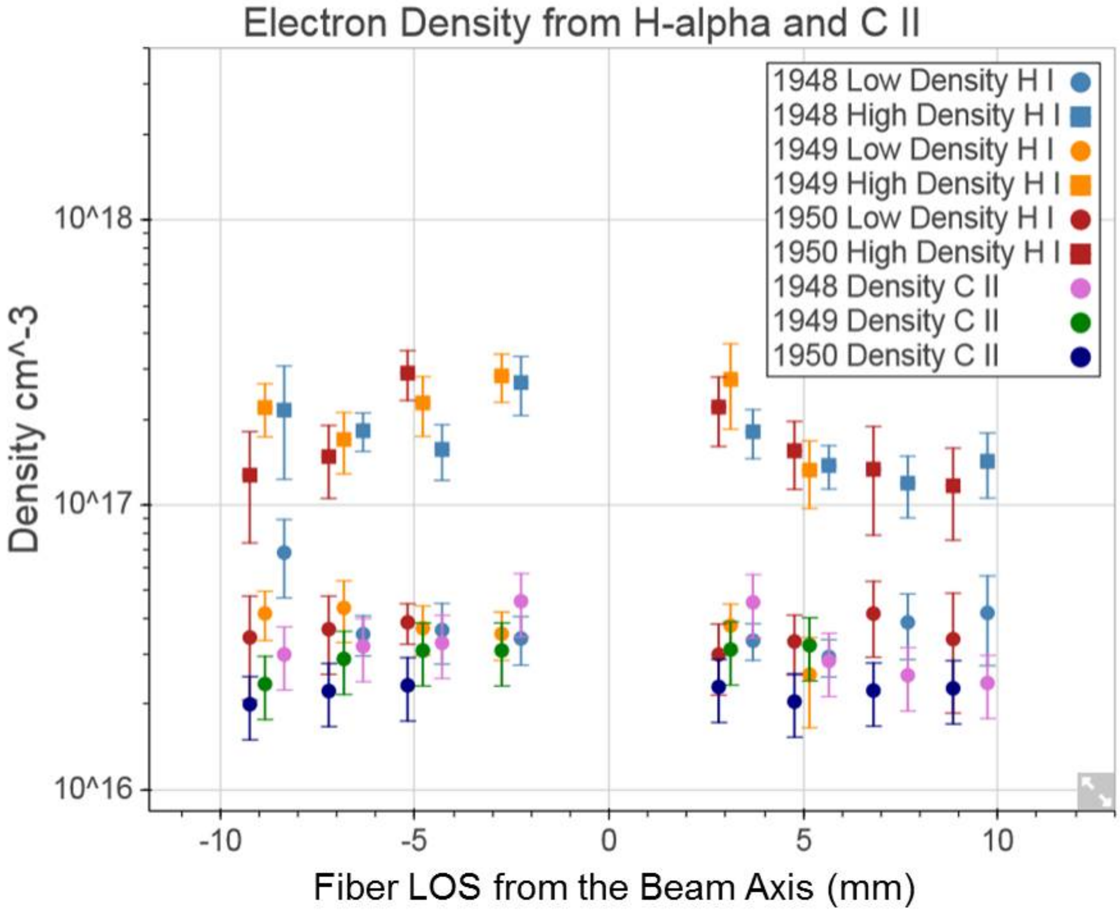

Figure 4.8: Density measurements from the H-alpha and CII line at 656.28 nm and 658 nm, respectively, as a function of radius. All fits of this data are given in Appendix A.

Shots 1949 and 1950 were taken on Al-coated tantalum convertors, and the B-dots measured an average of 130 kA for both of these shots. Shot 1948 was taken on a bare tantalum convertor and the currents were 20-40 kA higher over the duration of the ICCD gate, and yet the measured electron densities are comparable between the three shots. This discrepancy could be explained with TRSD spot size measurements. If the current density

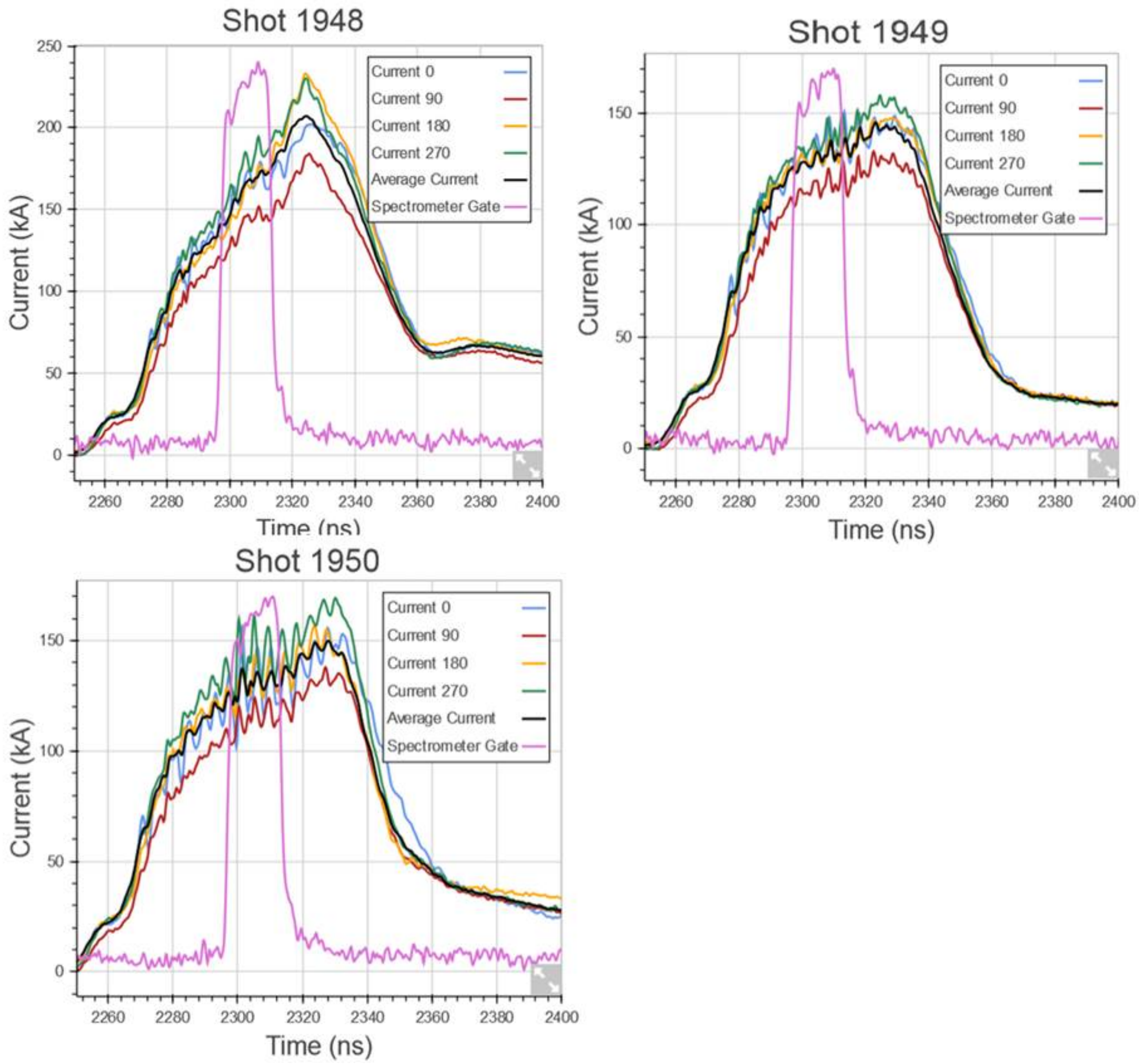

Figure 4.9: Beam current B-dot measurements and ICCD gate timings for the three shots in Figure 4.8.

is proportional to the ratio of the total beam current divided by the x-ray source spot size then the maximum current density for Shot 1948 was about 33% larger than Shot 1950 and 25% larger than Shot 1949. However, by the end of the ICCD gate the source spot diameter for Shot 1948 expanded to about 5.5 mm. In contrast, the spot expanded to 3.5 mm for Shot 1950 and 2.8 mm for Shot 1949. As a result the average current density, from peak to the end of the ICCD gate, for Shot 1948 was within 15% of 1950 and 1949. Consequently, the electron density profile from Shot 1948 is within the errors of the electron density profiles of Shots 1949 and 1950.

While electron temperatures were obtained from C III/C IV in Section 4.1, neutral hydrogen may be located in colder regions further from the axis than the C III or C IV ions. Although the wavelength window used for the H-alpha measurements in these shots did not encapsulate C III at 569.6 nm or C IV at 580.1 nm, both C III and C IV lines are usually visible on bare or coated convertor shots. Therefore it is likely that these ions are present in the diode and so an upper bound on the temperature can be estimated for Figure 4.8. Figure 4.10 gives the ratio of line intensities for C II/C III calculated in PrismSPECT for a non-LTE, zero width plasma.

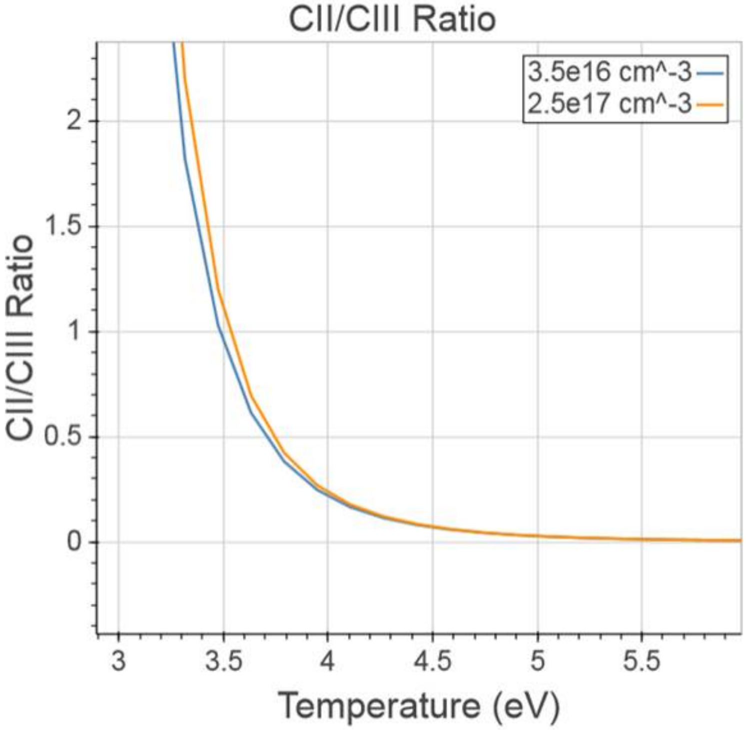

Figure 4.10: CII/CIII ratio for two different electron densities that correspond to measurements from H-alpha and measurements from C IV, in the next section.

The CII line strength is almost negligible at around 5 eV when compared to C III. This is in contrast to the estimates from the C III/C IV line ratio which gives electron temperatures of about 5.5-6.5 eV. Since C II and low density H-alpha Stark widths yielded similar densities, they are likely located at similar radii, and so the 5 eV upper bound on the electron temperature is also applicable to the H-alpha measurements. Since C IV and H I are probably located in different regions, electron density measurements from H-alpha may not be applicable to the C IV lines on which Zeeman splitting has been measured. H-alpha is likely located further from the axis, in a lower density region. Therefore, calculating C IV line widths using these electron densities would result in magnetic field estimates that are too high. Consequently, densities are obtained directly from the C IV profile fits in the next section.

4.2.2 Electron Density from C IV

Table 4.2: Electron densities are found from the broadened C IV doublet from these shots.

Shot Number	Anode Type	Fiber Array Type	B-dot measurements during ICCD gate (kA)
1919	C-coated Ta	Single Row 200 μm	130-155
1920	Si-coated W	Single Row 200 μm	125-155
1959	Standard SMP diode with Al-foil	Single Row 200 μm	125-140
1960	Standard SMP diode with Al-foil	Single Row 200 μm	125-140
2028	Al-coated Ta	Double Row 200 μm	115-120
2029	Na-coated Ta	Double Row 200 μm	130

Since each of the Zeeman components is broadened by the electron density, the magnetic field is also included in the C IV fits. Due to the sensitivity of the hydrogen line profile to Stark broadening, the few Tesla magnetic fields observed on RITS would not be visible on the H-alpha line, and so it was not necessary to include an external B-field in the fits for H-alpha. The spectra discussed in this section are all shots that have been analyzed for Zeeman splitting, and will be discussed further in Chapter 6. The experimental setup for these shots involved several different targets and arrays and they are summarized in Table

4.2. An example of a deconvolved C IV spectrum is also shown in Figure 4.11 for Shot 1920 which had a Si-coated, tungsten convertor plate.

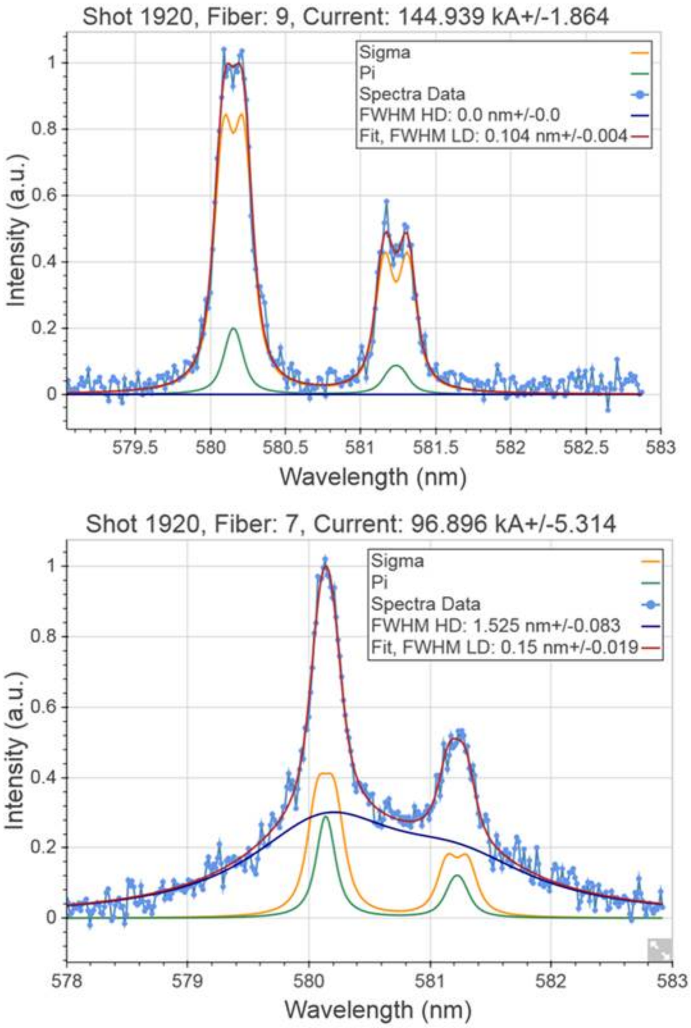

Figure 4.11: Spectral line fits for Shot 1920 of the C IV doublet lines. The pi (green) and sigma (yellow) contributions to the total line (red) are also plotted. Fiber 7, at 3 mm has broad wings that are fit with a higher density component (dark blue).

The C IV line profiles are deconvolved according to the procedure outlined in Section 3.6. Like the H-alpha line profiles, in the preceding section, the C IV lines also have a high density component. But in contrast to hydrogen, a high density component is not required to fit the C IV doublet lines at radii greater than 4-5 mm. For example in Figure 4.11, Fiber 9 does not have the broad lower intensity wings that Fiber 7 shows. Once the FWHM of the Lorentzian components have been determined, the electron density can be calculated.

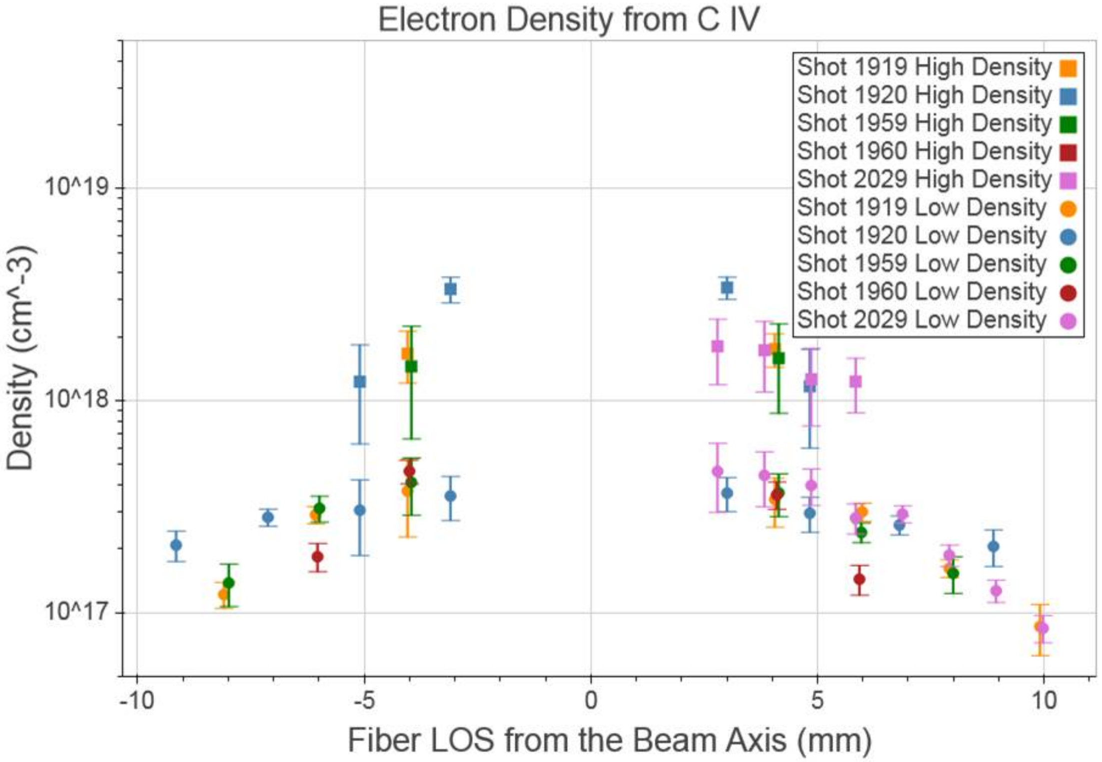

Figure 4.12: Electron densities from C IV. All fits of this data is given in Appendix C.

A code [58] developed at the Weizmann Institute generates fields produced by both electrons and ions that move according to classical trajectories, while the radiator is treated quantum mechanically. Using this method, Professor Y. Maron performed calculations of the C IV Stark width, and determined it to be 0.43 nm for an electron density of 10^{18} cm^{-3} at 6.2 eV, which scales linearly with density. This value is used to determine the density from the Lorentzian width of the C IV lines. The electron density profiles from the C IV lines for the shots listed in Table 4.2 are plotted in Figure 4.12.

The low density component from the C IV doublet is around 10^{17} cm^{-3} at about 10 mm from the axis and rises to mid-10^{17} cm^{-3}. The high density component, superimposed on the spectrum at radii less than 4-5 mm, also rises toward the beam axis with electron densities between $1\text{-}5\times10^{18}$ cm^{-3}.

Shots 1959 and 1960 were taken on a standard SMP diode anode, with an Al-foil placed in front of the bremsstrahlung convertor. The foil was initially glued 0.8 mm from the convertor, but as the glue dried this gap shrank and the foil became recessed. Consequently, the edge of the anode blocks the fibers from focusing along the foil surface. In order to image the surface for Shots 1959 and 1960 the fibers were moved just off the anode edge and angled toward the surface, as shown in Figure 4.13.

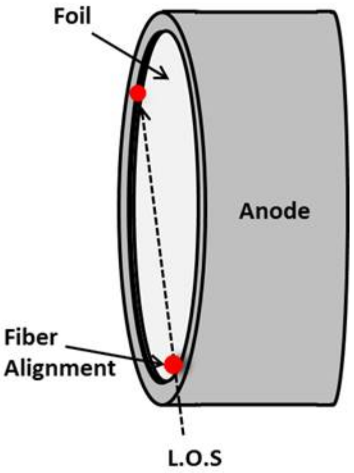

Figure 4.13: Sketch of the alignment for Shots 1959 and 1960. The fibers were backlit, moved past the anode on the front side, and angled toward the inside lip of the anode to image the foil surface.

Typically standard SMP shots show continuum on the central fibers, 2-3 mm from the beam axis, and the C IV lines are either absent or very weak on the outer fibers. The Al-foil is thought to limit plasma expansion into the AK gap as it should take more time to ionize the foil surface than the converter plate. Therefore, densities on the foil surface should be lower than on the bare or coated convertor surface for similar currents and timings.

This does not appear to be the case in Figure 4.12. Shots 1959 and 1960 have very similar electron densities and density profiles to the other shots which used coated converters without a foil. However, due to the angle of the line of sight, the fibers imaged more of the foil surface for the back half of the anode in Shots 1959 and 1960. In contrast, the other 3 shots imaged parallel to the converter with the bottom of the array aligned to the surface. Consequently, the spectra from Shots 1959 and 1960 may suggest that the foil surface plasma has electron densities that are comparable to regions that are further off the solid converter surfaces.

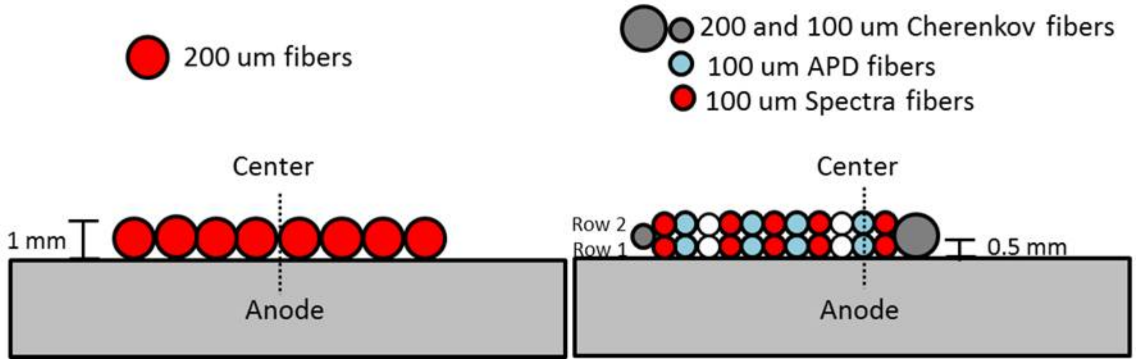

Figure 4.14: On the left is the single row array which consists of eleven 200 um fibers. Only 8 fibers are shown for clarity. On the right is the double row fiber array. Two fibers are used to measure the Cherenkov light (grey). The white circles represent spacing fibers used to extend out the array, and between these spacing fibers are an additional 16 rows of alternating APD (blue) and spectroscopy fibers (red).

In order to separate the high density surface region and a lower density region offset from this surface, a double row, 100 μm array was used in Shot 2029. The difference between the 100 μm array and 200 μm array is described in Chapter 3 and pictured again in Figure 4.14. This array is focused to half the diameter of the single row array (0.5 mm instead of 1 mm), and it separates the higher density surface from lower density regions further from the anode surface. The row of fibers closest to the surface will be referred to as Row 1, and the adjacent row will be called Row 2.

Spectra from the two rows are convolved together in shots that use the single row array. Unfortunately, for Shot 2029 the fibers were likely aligned slightly too far from the anode surface, resulting in very weak lines on Row 2, as shown in Figure 4.15. The electron density profile for this shot is therefore calculated from Row 1 and is similar to Shots 1919-1960 in Figure 4.12.

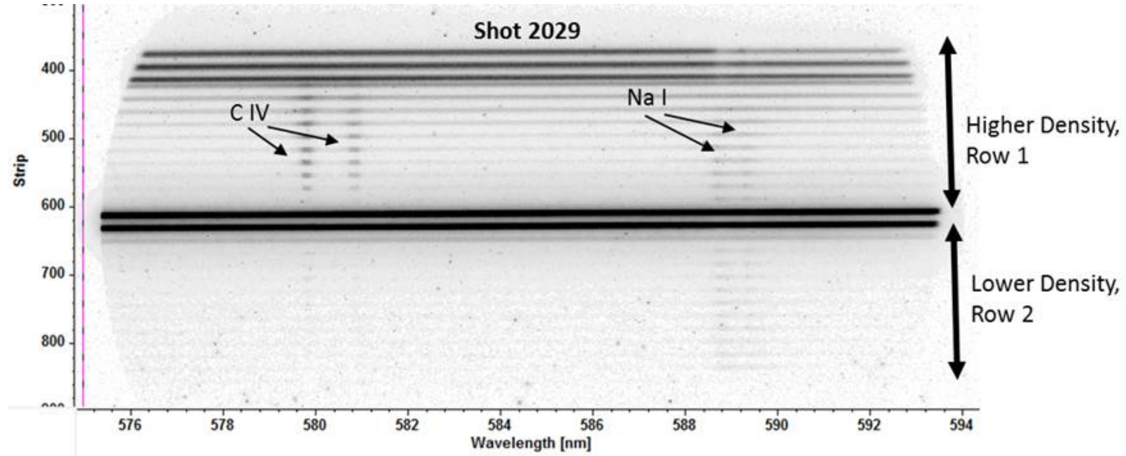

Figure 4.15: Raw spectral data for Shot 2029 using the double fiber array. The higher density spectra are from the bottom row of fibers, closest to the surface, and the lower density spectra are from the top row.

4.2.3 Densities from Al III

Spectra for Shot 2028 were also taken using the double row array on an Al-coated tantalum convertor. The spectra show strong Al III lines on both rows as shown in Figure 4.16, and so the electron density for both rows can be estimated from the Stark broadening of the Al III lines. The raw spectral data can be separated into three regions. Row 2 is fit with a single density. Row 1, which shows more broadening and therefore higher densities than Row 2, is fit with a two density approximation on fibers close to the beam axis (less

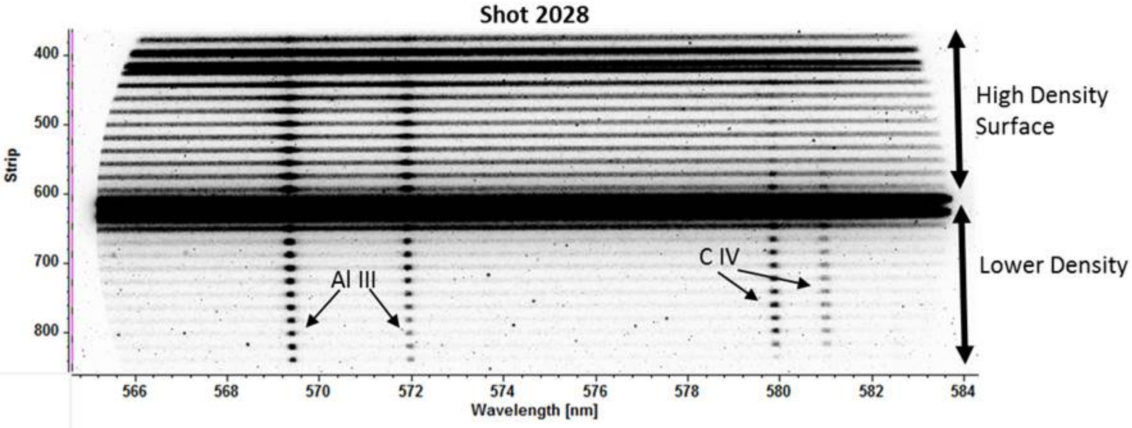

Figure 4.16: Raw spectral data for Shot 2028. Strong Al III and C IV lines are visible. The Al III lines are visibly broader on the fibers closest to the anode surface.

than 7.5 mm), and a single density further from the axis.

Figure 4.17 shows a lineout of spectra from Row 1 and 2 located 3.7 mm from the axis. Fiber 5, from Row 1, contains a high and low density component, suggesting that there are large density gradients within a 0.5 mm axial distance from the anode surface. Fiber 18, from Row 2, measures further into the AK gap (0.5-1 mm) where the densities are lower than on the anode surface. The Stark width here is about half the width of the low density component of Fiber 5.

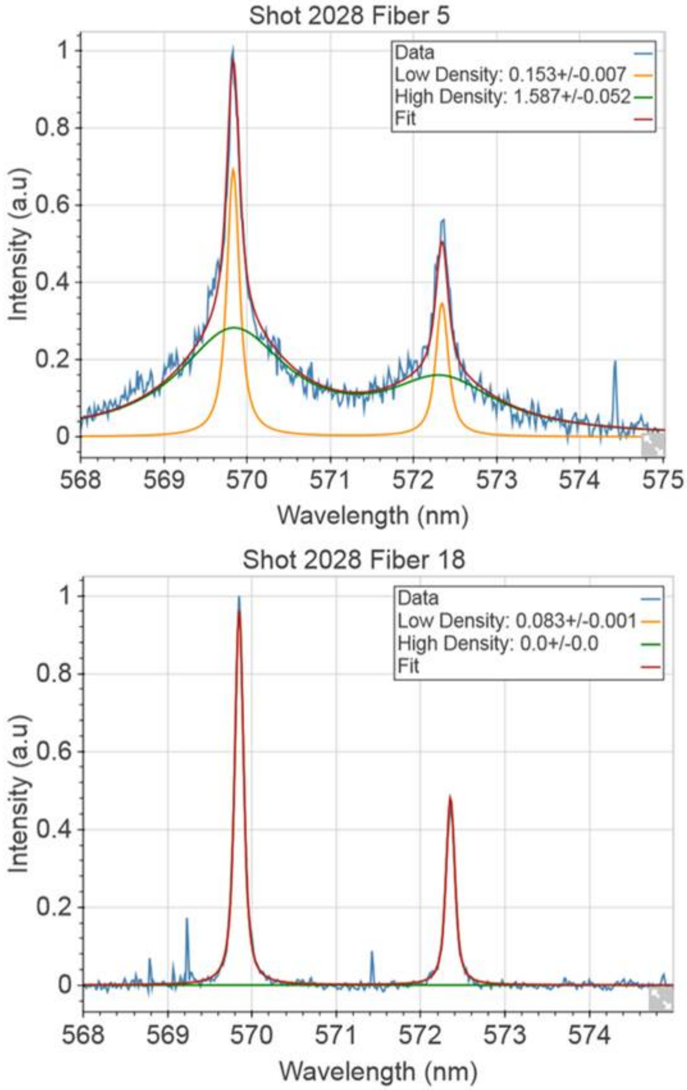

Figure 4.17: Al III fits. Both fibers are located 3.7 mm from the axis. Fiber 18 is 0.5 mm further into the AK gap then fiber 5.

Prof. Marons calculation, 0.6 nm for the Al III Stark width at an electron density of 10^{18} cm^{-3}, is used to estimate the density from the Al III lines. The density profiles from Shot 2028 are shown in Figure 4.18. The electron densities from C IV lines on Row 2 are also presented for comparison.

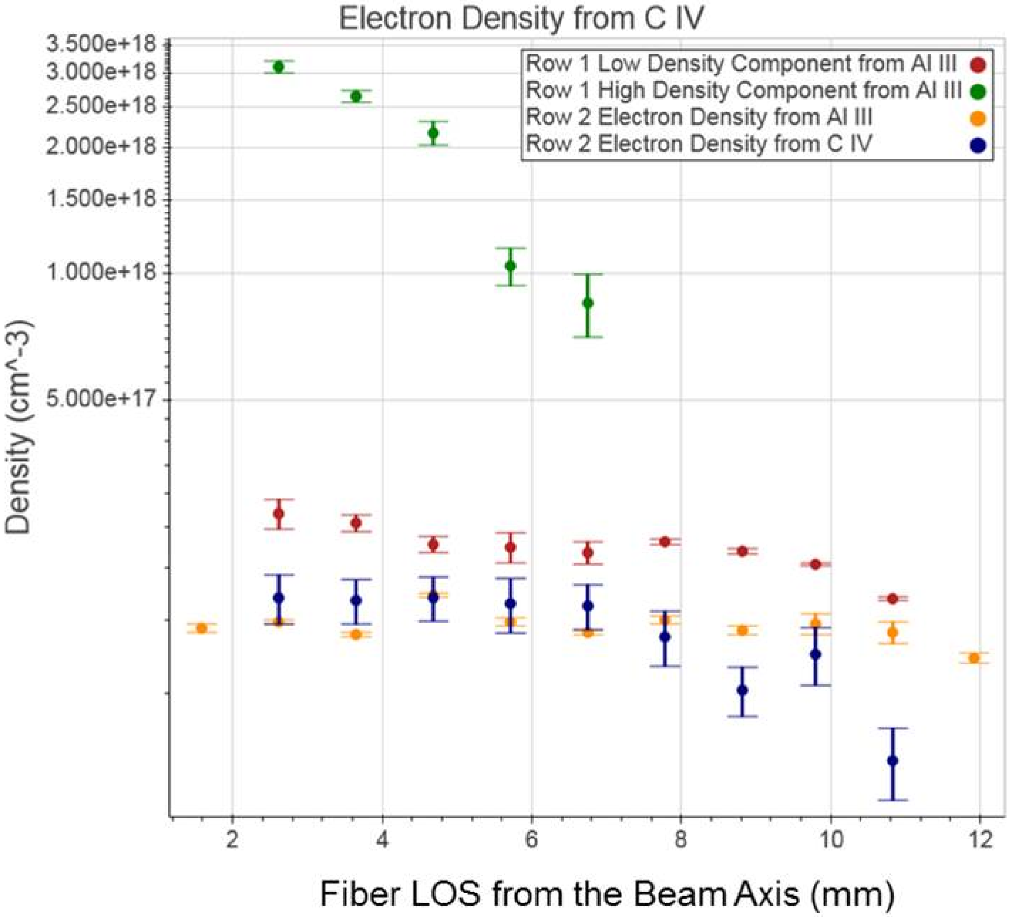

Figure 4.18: Electron densities for Shot 2028 calculated from Al III and C IV lines. Row 1 is closest to the anode surface and Row 2 is offset from the surface by about 0.5 -1 mm. All fits of this data are given in Appendix A.

Row 1 shows the largest density gradient. Within the 0.5 mm diameter of the fibers, the electron density increases by a factor of 5-10 from the low density components to the high density components that form the wings of the spectra. The high density component decreases almost linearly with distance from the axis, and is not required to fit the spectrum at radii larger than 7 mm. The low density component of Row 1 is within a factor of 2 of

Row 2, suggesting the density gradient decreases as the axial distance from the anode surface increases.

Within an 8 mm radius the electron densities calculated from Al III and C IV on Row 2 are between 2-3$\times 10^{17}$ cm^{-3}, suggesting that the two lines are from similar locations both axially and radially. However, electron densities from C IV begin to fall at about 8 mm from the axis, while the electron densities from Al III remain at around 2×10^{17} cm^{-3}. This could be caused by two effects. Spectra from Row 2 show splitting on the C IV lines, particularly at radii greater than 7.75 mm. Line splitting is not visible on the Al III lines for this shot, except possibly at radii greater than 9.5 mm, likely because the Stark width for Al III is about 40% larger. Consequently, an external magnetic field is included for the C IV fits but not the Al III fits. However, as the density and therefore Stark width decreases, Zeeman splitting forms a larger fraction of the total line width. By using the current estimates from C IV line splitting on Fiber 25 (at 10.8 mm), and applying it to the Al III doublet, shown in Figure 4.19, the electron density calculated from these two lines becomes nearly identical (6.7$\times 10^{16}$ cm^{-3} from Al III and 6.9$\times 10^{16}$ cm^{-3} from C IV).

Additionally, C III at 569.59 nm corresponds to the location of the Al III 3/2-1/2 transition. This line is most likely present because the Al III doublet ratio is greater than 2 at radii larger than 7 mm. C III would add to the Al III 3/2-1/2 transition, leading to larger Lorentizian widths.

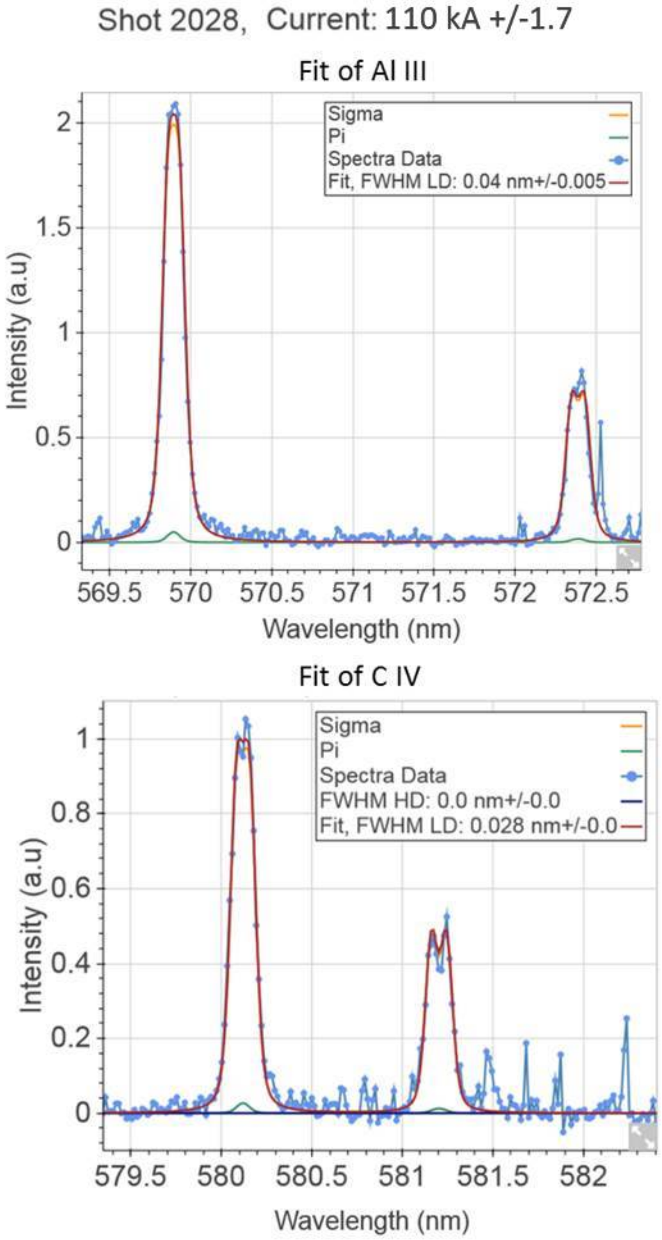

Figure 4.19: Fit of the Al III line (Left) using the current estimated from the CIV line (Right). The Lorentzian FWHM of the Al III fit is about 0.04 nm. Without including a magnetic field the FWHM is 0.84 nm.

4.3 Comparison of Electron Densities from H I, C IV and Al III

In Section 4.2.1 electron densities, estimated from H-alpha, are between 2-4$\times10^{16}$ cm^{-3} for the low density component and 1-3$\times10^{17}$ cm^{-3} for the high density component. In contrast, electron densities from C IV are 1-4$\times10^{17}$ cm^{-3} for the low density component and 1-4$\times10^{18}$ for the high density component. Furthermore, the high density component is necessary to fit the H-alpha wings across the entire fiber array. The C IV line fits only require a higher density component at radii less than 5-6 mm. Examples of C IV and H-alpha line fits at 8.1 mm and 8.35 mm, respectively, are given in Figure 4.20. The C IV doublet is fit with a single density. H-alpha, measured at a similar fiber position, has a wider base and the line profile is fit more accurately with a two-density region approximation.

The anode is about 5 cm in diameter, while the array covers a 2 cm diameter. Since the spectral intensity is integrated along the line of sight of the array, it is possible that the H-alpha line is measured further from the axis where the plasma is colder than the location at which C IV and Al III lines are present. In addition, Figure 4.8 shows uniform electron density measurements across the anode, particularly for the low density components, that do not appear to increase with decreasing radii. This suggests that the measurements from H-alpha originate from comparable locations along the line of sight, despite the position of the fibers. The high density component rises slightly for the H-alpha line, suggesting that the higher densities are measured closer to the beam axis than the low density component.

Since electron densities estimated from C IV continue to increase toward the axis, it is likely that C IV is present for radii between 2-12 mm. High density wings for the C IV lines are not present at radii greater than 5-6 mm. If, at large radii, the dense surface plasma is colder than the region just off the surface, than the broad C IV wings may only be present close to the axis. Further from the axis, only C IV from a less dense but higher temperature region would be seen in the spectra. Because H-alpha is a neutral line it continues to be

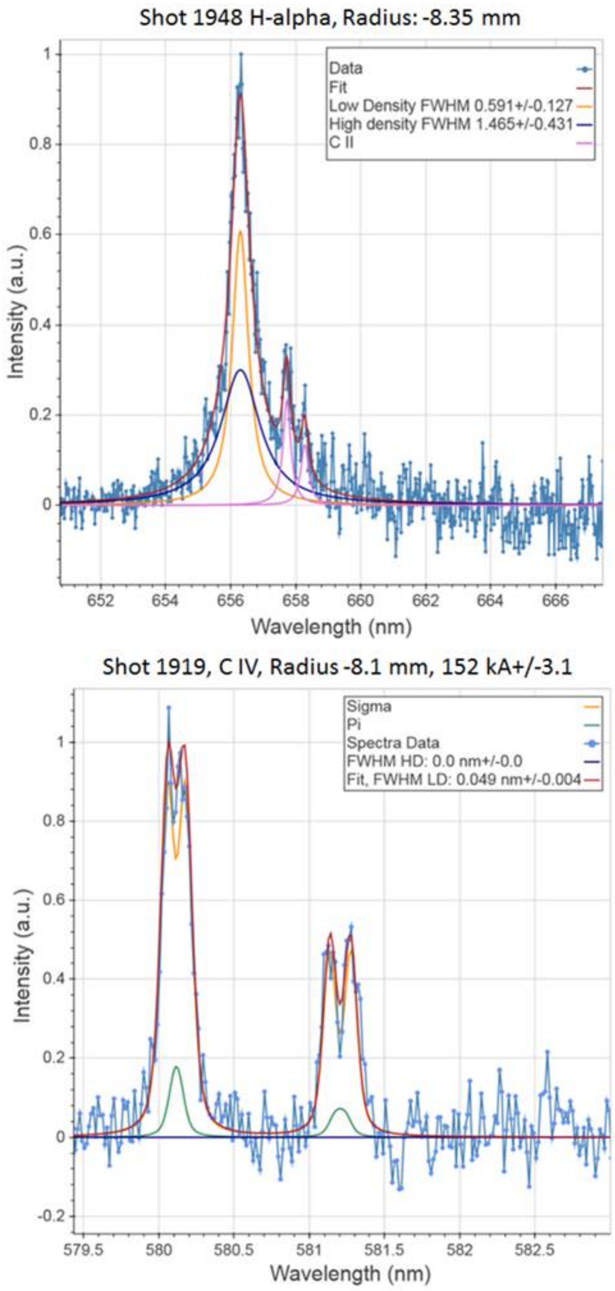

Figure 4.20: Comparison of an H-alpha line fit to a C IV line fit at similar locations. Shot 1948 was on a bare tantalum convertor and shot 1919 was on a C-coated tantalum convertor.

present near the colder surface, and so the higher density wings are present even at large radii. Finally, fitting the Al III line for Shot 2028 confirms a high electron density surface, with large density gradients within 0.5 mm of the convertor surface, as shown in Figure 4.18. A qualitative representation of the different density regimes on the anode surface is shown in Figure 4.21 for this analysis.

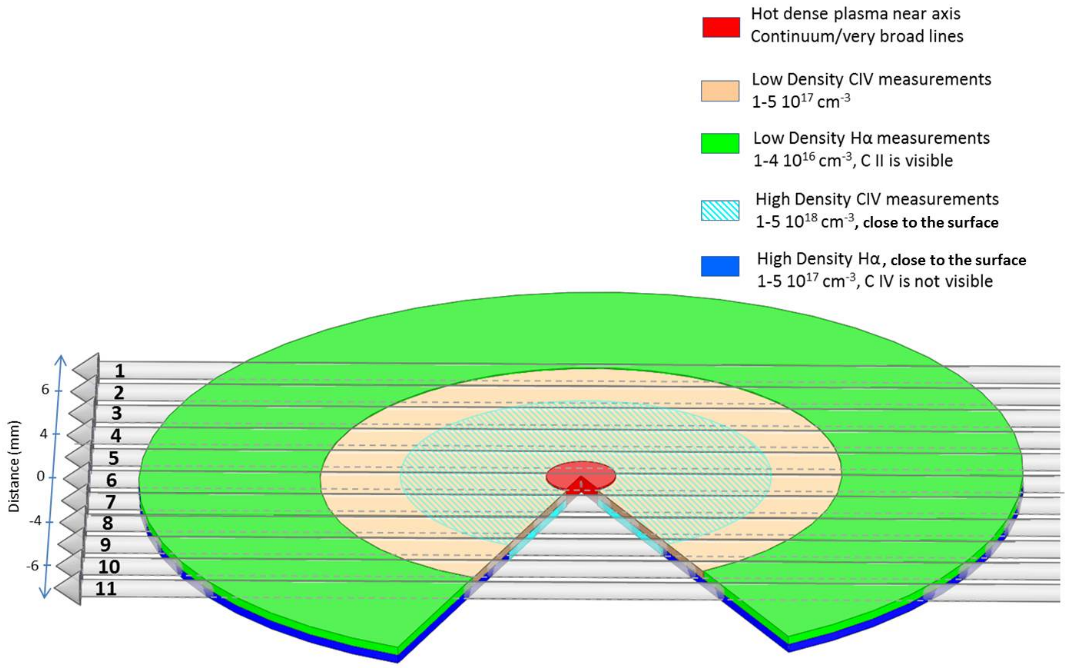

Figure 4.21: Sketch of the different density regions that may be present on the SMP anode surface to form the spectra discussed in Section 4.2. The arrows represent the fiber line of sight for the single row 200 μm fiber array.

For the 200 μm fiber array, 11 fibers view through the diode plasma which has varying densities and temperatures. The fibers would observe both H I and C IV depending on the wavelength window. For example, the outer fibers (1, 2, 10, 11) would measure only a low density C IV component if the surface plasma is too cold at these radii for C IV to be present. The inner fibers (3, 4, 8, 9) would measure both a low and high density C IV component, since the plasma temperature is higher closer to the beam axis. The central three fibers, would measure continuum and/or extremely broad lines due to the high densities on axis. A wavelength window centered on H-alpha would result in spectra in which the H-alpha low density width is essentially constant across all the fibers. The high density component may increase slightly since it extends closer to the beam axis, as is seen in Figure 4.8. When using the double row array, the two regions would be decoupled. However, based on Figure 4.18, the higher density region is probably very close to the anode surface (within 0.5 mm), with density gradients that become less sharp as the distance from the surface increases.

CHAPTER 5

Current Profile Measurements on the SMP Diode

The goal of these measurements is to determine the current distribution within the SMP diode. The framing camera takes time-gated images of the diode self-emission and is used to evaluate the symmetry of the anode plasma formation which is critical to the analysis of the Zeeman-split lines. A 0.5 m spectrometer coupled to a streak camera measures the spectrum of the diode plasma as a function of time at a single location. Initially, a time-gated 0.15 m spectrometer surveyed the composition of the diode plasma. This was later replaced with a higher resolution 0.32 m spectrometer in order to resolve line splitting from which the magnetic field and current profiles are estimated. Finally, B-dot probess monitor the current along the MITL and provide a comparison to the Zeeman splitting measurements. The results of these diagnostics will be discussed in detail in this chapter.

5.1 Framing Camera Images

A single-frame camera was used to image the SMP diode AK gap. As the electron beam pinches onto the anode, plasmas form on the surface and expand into the gap. Typically, the anode plasma forms symmetrically, with the highest density plasma occurring on the beam axis. The anode surface further from the axis is ionized thermally resulting in lower electron densities. An ion current from this plasma streams back toward the cathode, and partially neutralizes the electron beam, leading to stronger beam pinching [5].

Often, on poor shots, the camera images indicate dense plasma formation that has spread out along the anode surface, as in Shot 1967 in Figure 5.1. This may be due to poor pinch dynamics during the shot or significant beam motion. Shot 1967 had a Si-coated Al-foil on an otherwise standard SMP diode. The asymmetric plasma formation suggests the beam never pinched to a small spot and/or it rapidly expanded during the pulse. This is confirmed with the TRSD measurements which suggest a large minimum spot size followed by rapid beam expansion early in the pulse. In addition, the radiation pulse length was sub 20 ns on this shot, about 20-25 ns shorter than a standard SMP diode shot.

Shot 1959 had a standard SMP diode geometry with an Al-foil that is offset by less than one millimeter from the anode surface. Usually, on these shots radiation pulses between 40-50 ns FWHM are achieved, and symmetric plasma formation near the beam axis is visible on the framing camera images.

On standard SMP shots, the impedance continues to decrease during the radiation pulse due to plasma expansion. On poor shots, the radiation pulse ends early and the current often rapidly increases, suggesting an early impedance collapse. Although it is still not well understood why some dopants on the anode result in full radiation pulses and others cause the pulse to end early, recent simulations [5] have suggested two mechanisms that can cause the impedance to collapse in the diode. Plasmas that expand into the AK gap can decrease the gap width over time. Additionally, ions with sufficient momentum perpendicular to the axis can escape the high electron densities near the axis, and cause an increase in the ion space charge around the outer cathode surface, which would lead to another source for the electron current.

In Shot 1967 the intense emission along the anode surface suggests higher electron densities further from the axis when compared to Shot 1959. Therefore it is possible that the greater number of ions far from the axis on Shot 1967 traveled axially along the electric field, leading to a buildup of space charge on the outer cathode which would increase the

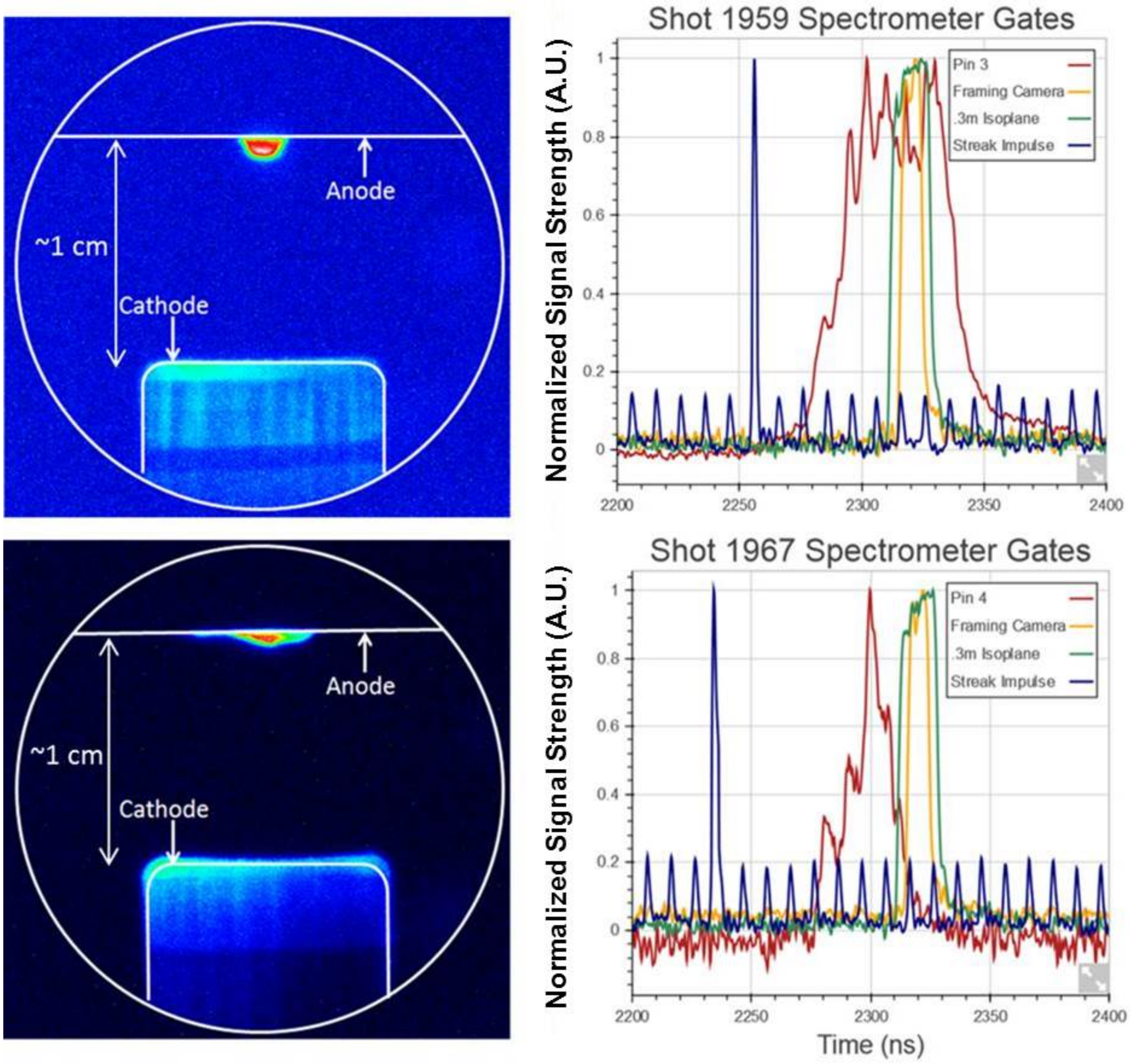

Figure 5.1: Top: (Shot 1959) Symmetric anode plasma formation on a standard SMP diode configuration with an Al-foil. Bottom: (Shot 1967) Asymmetric plasma formation on a diode with a Si-coated Al foil. The timing of the framing camera image (yellow) for both shots is shown on the right relative to the radiation pulse (red).

current and lead to impedance loss.

5.2 Streak Spectrometer Data

Time resolved spectra of the SMP diode would help determine when the strongest spectral lines appear during the radiation pulse, and when they become too broad to use for meaningful Zeeman splitting measurements. In Figure 5.2, two images are shown. Shot 2017 consisted of a standard SMP diode shot with an aluminum foil over a tantalum converter. Shot 2027 had an aluminum-coated tantalum converter plate, rather than a foil. The row of dots on the left are spaced 10 ns apart. The bright spot is the impulse signal, used to calibrate the timing relative to the radiation pulse. Both images were taken using fibers that were aligned about 4 mm from the anode center. Spectra from fibers closer to the axis quickly become dominated by continuum. Further from the axis, the signal strength drops.

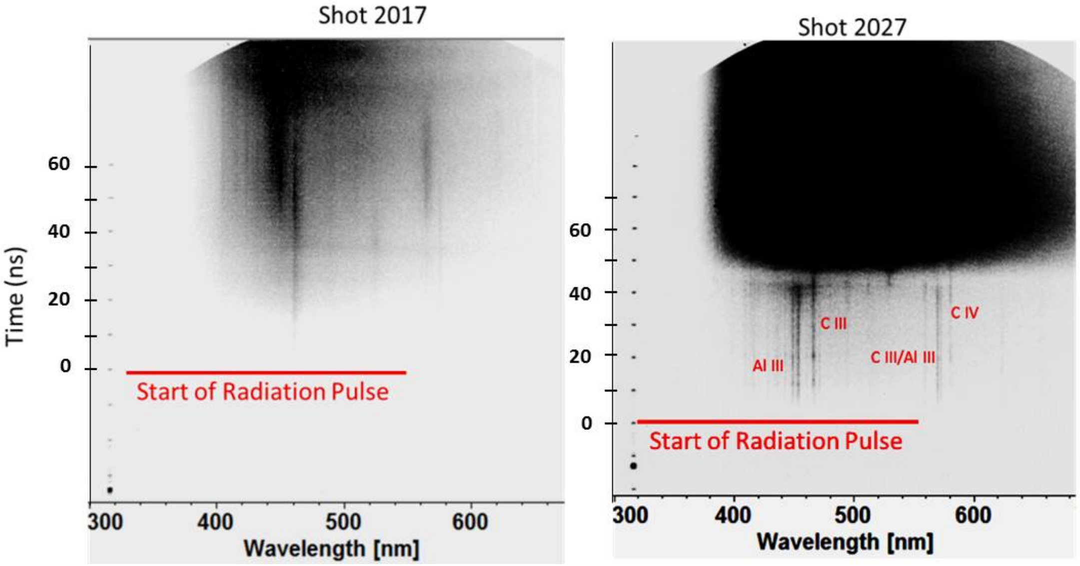

Figure 5.2: Top: Streaked spectra from a standard SMP diode configuration with a foil. Bottom: Streaked spectra from Al coated Tantalum converter, without a foil.

Shot 2017 shows much less continuum throughout the 60 ns, while Shot 2027 becomes dominated by the dense plasma within 45 ns. On Shot 2017 CIII lines are visible relatively early, within 10 ns of the start of the radiation pulse. However, most of the line emission in the mid visible spectral range occurs much later, 30 ns after the start of the radiation pulse. Additionally, these lines are weaker than in the no-foil configuration. Strong aluminum and carbon lines are visible approximately 10 ns after the start of the radiation pulse on the Al-coated converter shots.

The foil is mostly transparent to the electron beam, and is thought to limit the anode plasma expansion into the gap. However, foil shots typically result in noisy spectral data during the pulse since it takes some time for the offset foil to thermally ionize. As a result, most of the shots in which splitting was measured used a bare or coated anode converter plate.

5.3 Low Resolution Spectral Data

Initially, a low resolution spectrometer was fielded on RITS-6 to characterize the SMP diode spectrum over a wide wavelength window, as discussed in Section 3.5.3 and pictured in Figure 3.15. This initial survey of the anode plasma was undertaken during the radiation pulse on the standard SMP diode to understand what contaminants are present in the diode and what lines would be good candidates for Zeeman splitting measurements.

These survey measurements were made with a Princeton Instruments, SP-2150 [45], spectrometer. With a 150 g/mm grating and a 50 μm slit width this spectrometer gave a 5 nm spectral resolution. The spectral data from Shot 1816 are shown in Figure 5.3. These spectra were taken at the end of the radiation pulse. This late in the radiation pulse the foil has ionized and aluminum lines are visible. The carbon and hydrogen lines are likely a contaminant from the hydrocarbons from the oil that is brushed onto the field shaping knob to prevent field emission of electrons. Because the vapor pressure of oil is greater than the vacuum chamber pressure, the oil can potentially coat the electrode surfaces. Spectra from fibers on or close to the beam axis typically only show continuum in this spectral range. This continuum is due mainly to bremsstrahlung radiation, radiative recombination, and line broadening from the high densities and temperatures at these locations.

The time-gated evolution of the C IV lines (at 580.13 nm and 581.20 nm) during the

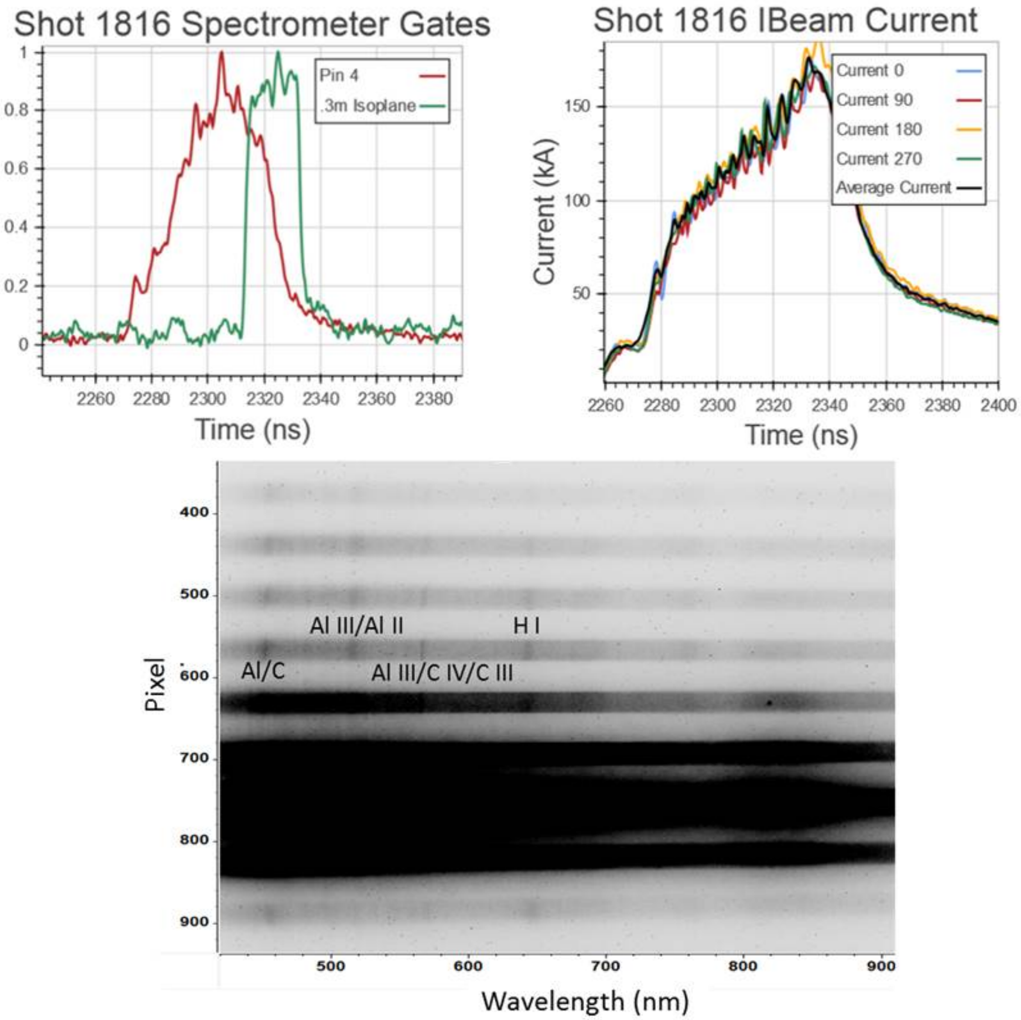

Figure 5.3: Top Left: Spectrometer ICCD gate timing (in green) with respect to the radiation pulse (in red). Top Right: Current as measured from the diode B-dots. Bottom: Raw spectral data for a typical SMP diode geometry.

radiation pulse is shown in Figure 5.4. The fibers are located approximately 4 mm from the beam axis, determined by the method outlined in Section 3.6.3. These spectra were taken using the low resolution, 0.15 m spectrometer with a 1200 g/mm grating and 50 μm slit width, resulting in a resolution of about 0.4 nm. Initially, the signal to noise ratio is very small and the CIV doublet is barely visible and comparable to the noise levels. By mid-pulse, the CIV doublet is visible, along with the CIII line at 569.59 nm. By the end of the radiation pulse the CIV lines are well above the noise, and the CIII/CIV ratio has decreased, indicating an increase in electron temperature.

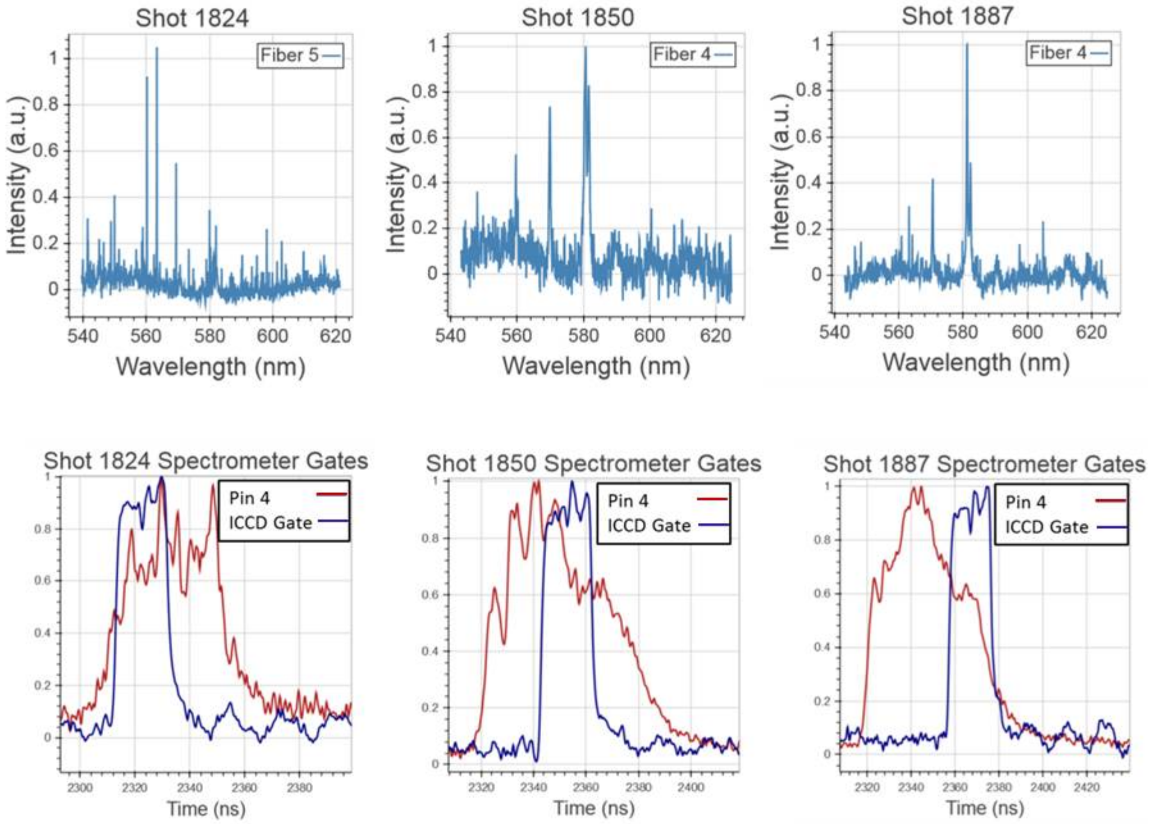

Figure 5.4: Time evolution of the C IV (at 580.13 nm and 581.20 nm) line using a 0.15m spectrometer. Top: Calibrated spectra approximately 4mm from the beam axis. Bottom: Corresponding x-ray radiation pulse (red) and width of the ICCD gate (blue).

To accurately resolve the Zeeman effect, a high signal to noise ratio is required in order to prevent noise fluctuations from obscuring the fine structure splitting due to the modest magnetic fields in the diode. As a result, all of the spectra analyzed for Zeeman splitting were taken toward the middle-end of the radiation pulse. Additionally, because it takes time to thermally ionize the aluminum foil which is offset from the high Z convertor plate, the signal to noise ratio during the radiation pulse can be further improved by removing this foil and using a bare or coated anode plate, as discussed in Section 5.2. However, this usually reduces the radiation pulse width, and is less useful for radiographic purposes because the dose decreases as the pulse width shrinks.

5.4 High Resolution Spectral Data

Unfortunately, with the setup discussed in Section 3.5.2, it is not possible to directly measure time resolved line splitting, particularly on the standard SMP diode shots, using the streak spectrometer system. The spectrometer has an f/6.5 aperture ratio, and is therefore not conducive for making high resolution measurements with the light intensity levels measured on the SMP diode so far. Additionally the streak camera disperses the spectra in time, resulting in even lower signals, and the camera photocathode has a low quantum efficiency (5% at 550 nm). Therefore, in order to increase the signal to noise and accurately measure line splitting, a time gated ICCD camera coupled to a smaller f-number (f/4.6) spectrometer was used. This allowed for spatially resolved measurements at several locations across the anode surface, rather than a time resolved measurement at a single location.

After characterizing the anode plasma composition during the radiation pulse, the low resolution spectrometer, discussed in Section 5.3, was replaced with a larger, higher resolution spectrometer. Figure 5.5 shows the resolution required to measure visible splitting on the C IV doublet for a line of sight parallel to a 3 T magnetic field, in the absence of noise.

In Figure 5.5, the electron densities are related to the Stark width, or the FWHM of the Lorentzian component of a spectral line. The instrument resolution is the FWHM of a Gaussian profile. The requirements for the spectral resolution increase as the Stark width increases since high electron densities cause pressure broadening to dominate the line profile. Because the magnetic fields in the diode are small, in order to resolve splitting rather than simply line broadening due to the magnetic fields, a resolution of less than 0.1 nm is required for Stark widths less than 0.1 nm. However, the actual resolution must be slightly higher than this plot would suggest due to random noise in the collected spectra, particularly for measurements far from the axis where the C IV line intensity is low. Thermal Doppler effects due to the electron temperature have not been accounted for in this plot.

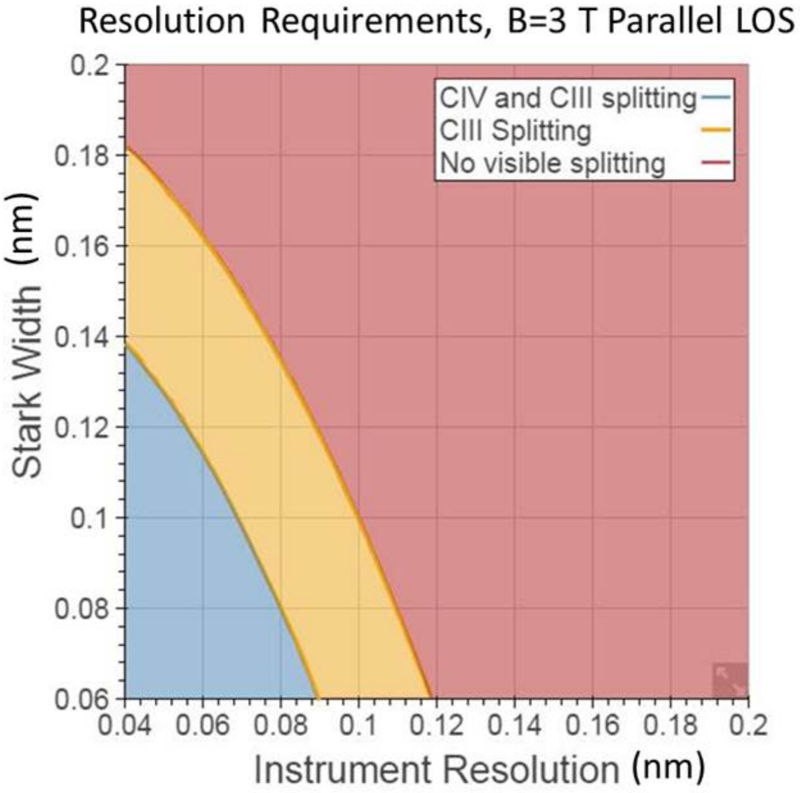

Figure 5.5: The resolution requirements for a given electron density in the parallel line of sight for a 3 T magnetic field.

However, for the electron temperatures typically measured from the CIII/CIV line ratios, the effect of Doppler broadening is about half the instrument resolution.

For a line of sight that is perpendicular to the magnetic field, the required spectrometer resolution must be further increased since the central pi lines are visible in this orientation. However, polarization optics, when measuring normal to the magnetic field, may be used to extract the sigma components which are linearly polarized perpendicular to the field. Unfortunately, the spectral line intensities are not large enough to use linear polarizers which would reduce the light intensity by about 50%.

As discussed in Section 2.2 the $^2\mathrm{P}_{1/2} -^2 \mathrm{S}_{1/2}$, at 581.20 nm, transition is slightly broader when compared to the $^2\mathrm{P}_{3/2} -^2 \mathrm{S}_{1/2}$, at 580.13 nm, transition [31] due to the fact that the Zeeman components do not have equal intensities. The pi/sigma ratio on the 1/2-1/2 transition is smaller, and this transition also has a slightly larger energy shift in the presence of a magnetic field. This effect is also exemplified in Figure 5.5, where there is a band in which only the $^2\mathrm{P}_{1/2} -^2 \mathrm{S}_{1/2}$ line appears split. Since all other broadening mechanisms, Stark, Doppler, and the instrument resolution, are essentially the same this effect is a clear indication of the presence of a magnetic field. The Isoplane-320 spectrometer with a 2400 g/mm grating and a 50 μm slit width has a resolution of about 0.065, but the contribution of pi components along the line of sight and higher densities closer to the beam axis obscure the line splitting. Consequently, several of the measurements presented here fall above the required threshold to resolve Zeeman splitting. However, at this resolution the $^2\mathrm{P}_{1/2} -^2 \mathrm{S}_{1/2}$ line is often visibly broader then the $^2\mathrm{P}_{1/2} -^2 \mathrm{S}_{1/2}$ line, which indicates an external B-field. Additionally, line broadening due to a magnetic field can yield a fairly distinctive spectral line shape with a flat-top profile and so these profiles can still be fit by assuming a B-field.

Figure 5.6 shows spectra from two shots using a fiber aligned 5.9 mm from the axis. These spectra represent an integrated intensity across a chordal line of sight. Both were taken at about 130-140 kA as measured from the diode B-dots. However, Shot 1960, with the standard SMP diode configuration has a lower SNR, when compared to Shot 1919, since the foil takes some time to ionize.

The current rapidly increases (~50 kA in 25 ns) in Shot 1919 at about 2310 ns. This is indicative of impedance collapse, in which the diode shorts probably due to AK gap closure [5]. At this point the radiation pulse ends, and usually on SMP diode shots in which a foil is not used, the pulse ends about 10-15 ns earlier.

The majority of the spectroscopy shots taken with the high resolution spectroscopy set up were taken during the flat part of the current pulse, just before the impedance collapses, to prevent averaging over large current changes during the spectrometer gate width and to obtain a large C IV signal. Both shots in Figure 5.6 show evidence of Zeeman splitting. Shot 1919 shows broadened lines; this is particularly visible on the $^2\mathrm{P}_{1/2} -^2 \mathrm{S}_{1/2}$ transition, at 581.20 nm. Shot 1960 shows clear line splitting that is also more pronounced on the 1/2-

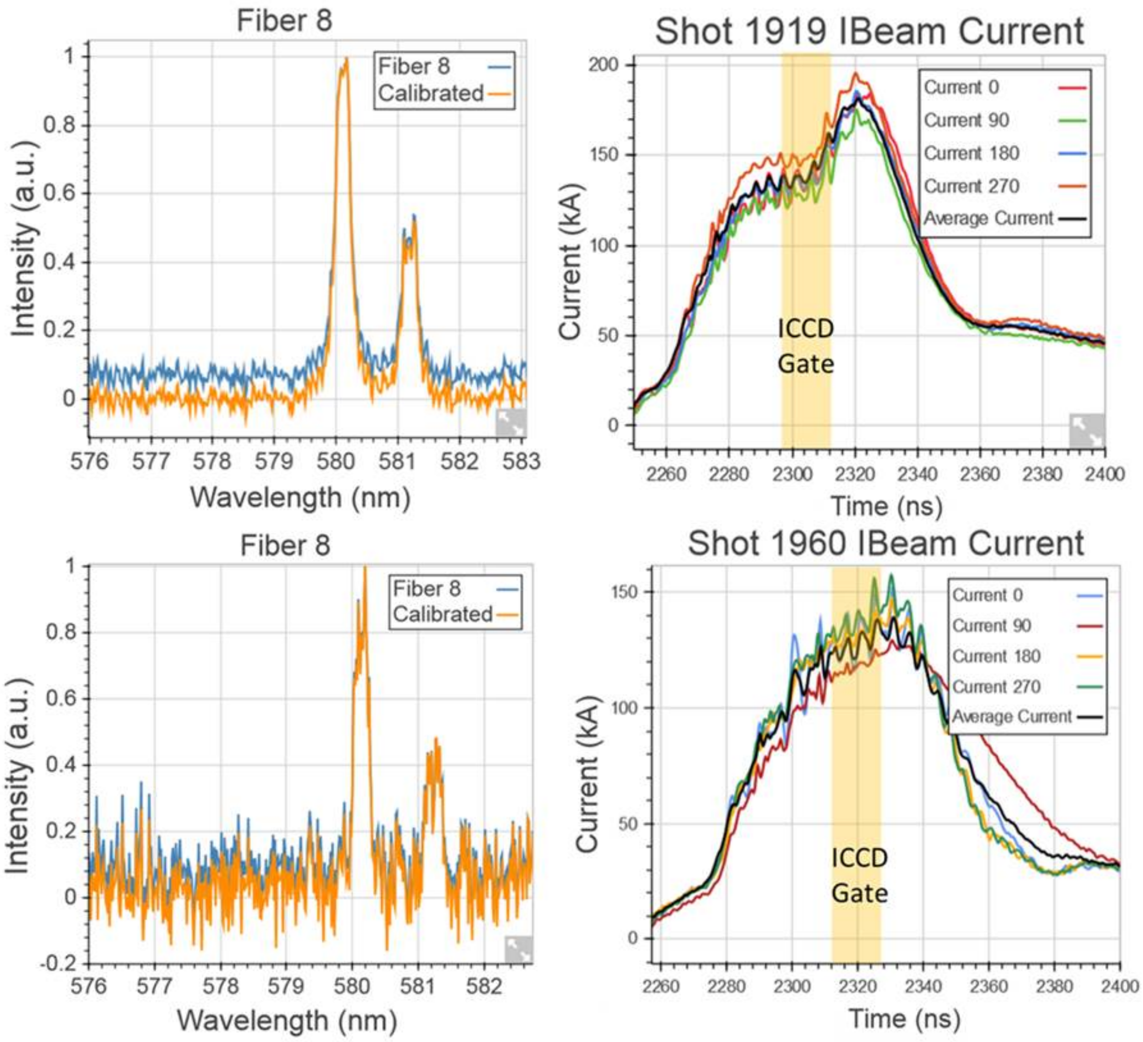

Figure 5.6: Top: CIV spectrum taken on the SMP diode without a foil. Bottom: CIV spectrum taken on the diode with an Al foil.

1/2 transition. Several shots are analyzed for Zeeman splitting on the CIV line as a result of the beam current, and the setup for each of these shots is summarized in Table 5.1.

Table 5.1: Summary of shots for which CIV line splitting was fit.

Shot Number	**Anode Type**	**Fiber Array Type**
1919	C-coated Ta plate	Single Row 200 μm
1920	Si-coated W plate	Single Row 200 μm
1959	Standard SMP with Al foil	Single Row 200 μm
1960	Standard SMP with Al foil	Single Row 200 μm
2028	Al-coated Ta	Double Row 100 μm
2029	Na-coated Ta	Double Row 100 μm

5.5 Spectrum Deconvolution

5.5.1 Magnetic Field

Since the spectra are line integrated along chords across the anode surface, both pi and sigma components are visible in the Zeeman splitting measurements, though Stark broadening obscures their individual contributions. As a result, the multiple magnetic fields and field angles to the line of sight need to be deconvolved from the spectrum in order to recover the enclosed current. Additionally, the contributions along the line of sight must be weighted by intensity to account for the line intensity decay with distance from the axis. This can be achieved using Abel inversions, discussed in Section 3.6.5.

The fitting algorithm involves discretizing the line of sight into multiple points and calculating the magnetic field, relative intensity of the spectral line, and the angle of the B-field to line of sight, at each point to simulate a spectrum. Each Zeeman component is estimated to be a Voigt profile with Stark broadening forming the Lorentzian part, and thermal Doppler plus instrument broadening composing the Gaussian portion. The sum of the discretized calculated spectra is then fit to the data with a LevenbergMarquardt curve fitting algorithm in the SciPy [67] Python library.

Figure 5.7 illustrates the surface of the anode with discretized points along the line of sight. The semi-circles represent lines of constant magnetic fields. Along the line of sight, at 6 mm from the axis, tangent lines to these field lines are plotted to exemplify the angles between the magnetic field and line of sight.

The magnetic field at each point on the circle is calculated using Amperes law,

$$B = \frac{\mu_o I}{2\pi r} \tag{5.1}$$

where I is the enclosed current and r is the distance from the axis to a point along the line of sight, illustrated as red points in the above figure. The fine structure splitting due to an

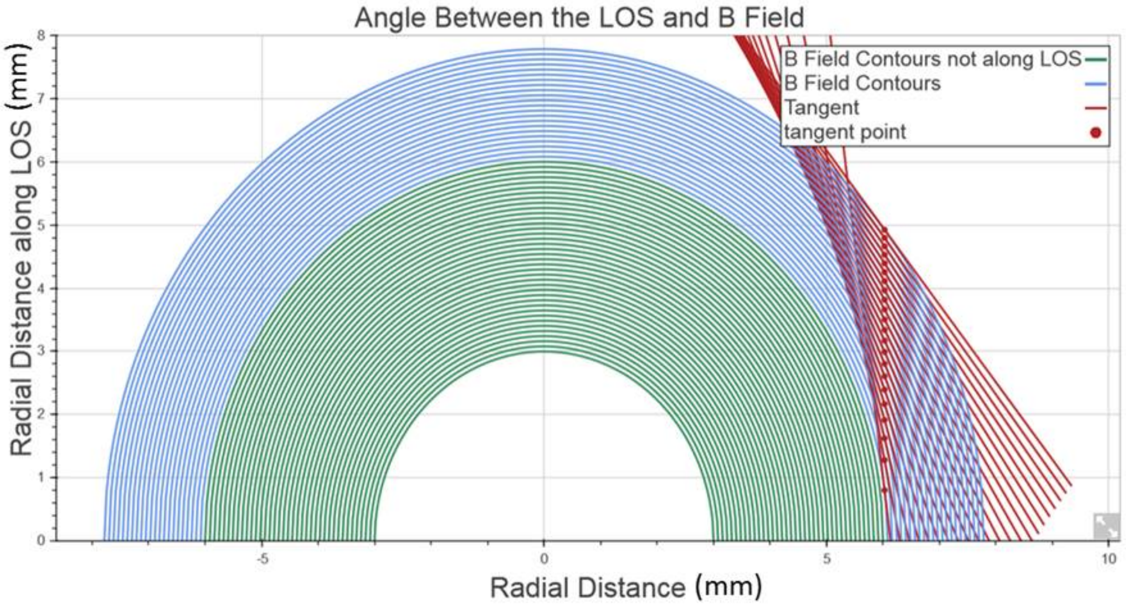

Figure 5.7: Schematic showing constant magnetic field lines (green and blue) and angles to the line of sight at 6mm. The green semi-circles represent magnetic fields that do not affect the spectrum. For clarity only a 1 cm chord (0.5 cm on either side of the axis) is shown. In the actual fits a 2 cm chord is used, with 1 cm on either side of the axis.

external B-field in the weak field Zeeman approximation is [24],

$$\Delta E = g\mu_B m_j B \tag{5.2}$$

where g is the Lande g-factor factor, μ_B is the Bohr Magneton, m_j is the magnetic quantum number, and B is the magnetic field.

Accordingly, this method assumes cylindrical symmetry of the electron beam and current. This is a reasonable assumption because visible framing camera images and time integrated spot images (as measured from an x-ray pinhole camera) are usually fairly symmetric. Additionally, the four B-dots placed symmetrically around the cathode measure similar currents. Since each shot results in several usable spectra along the anode surface the current distribution can be estimated across the anode, and if all the current is concentrated close to the axis, the magnetic field should decay as 1/r with distance from the axis.

5.5.2 Magnetic Field Angles and Zeeman Component Intensities

As discussed in Section 2.2 Zeeman components do not have equal intensities. The pi to sigma ratio depends on the quantum numbers, m and J. Additionally, the intensities of these components should be adjusted to account for the angle between the magnetic field and the line of sight. When measuring parallel to the B-field, the pi lines are not visible, and when measuring perpendicular to the B-field, both the pi and sigma lines are visible. For intermediate angles the relative intensities can be adjusted by calculating the Stokes parameters for polarized light [30]. The Zeeman transitions, relative component intensities and angle adjustments can be found in Table 5.2 for the CIV doublet transition at 580.13 nm and 581.20 nm.

Table 5.2: Summary of Zeeman transitions for a 2P-2S transition, with the relative intensities of the components [28] and the L.O.S. angle correction [30]

λ_0**=580.13 nm**					
$\mathbf{J \rightarrow J^0}$	$\mathbf{g \rightarrow g^0}$	**Comp.**	$\mathbf{m_j \rightarrow {m_j}^0}$	**Relative Intensity**	**B-field Angle Correction**
3/2 → 1/2	4/3 → 2	σ_-	3/2 → 1/2	$\frac{1}{4}(J+m_j)(J+m_j-1) \propto \binom{1.5}{0.5} I_o$	$I_{\sigma_-} \propto \binom{1.5}{0.5}(1+cos^2\theta)I_o$
			1/2 → -1/2		
		π	1/2 → 1/2	$J^2 - m^2 \propto \binom{2}{2} I_o$	$I_\pi \propto \binom{2}{2}(sin^2\theta)I_o$
			-1/2 → -1/2		
		σ_+	-3/2 → 1/2	$\frac{1}{4}(J-m_j)(J-m_j-1) \propto \binom{1.5}{0.5} I_o$	$I_{\sigma_+} \propto \binom{1.5}{0.5}(1+cos^2\theta)I_o$
			-1/2 → 1/2		
λ_0**=581.23 nm**					
$\mathbf{J \rightarrow J^0}$	$\mathbf{g \rightarrow g^0}$	**Comp.**	$\mathbf{m_j \rightarrow {m_j}^0}$	**Relative Intensity**	**B-field Angle Correction**
1/2 → 1/2	2/3 → 2	σ_-	1/2 → -1/2	$\frac{1}{4}(J+m_j)(J-m_j+1) \propto 0.25 I_o$	$I_{\sigma_-} \propto 0.25(1+cos^2\theta)I_o$
		π	1/2 → 1/2	$m_j \propto \binom{0.25}{0.25} I_o$	$I_\pi \propto \binom{0.25}{0.25}(sin^2\theta)I_o$
			-1/2 → -1/2		
		σ_+	-1/2 → 1/2	$\frac{1}{4}(J-m_j)(J+m_j+1) \propto 0.25 I_o$	$I_{\sigma_{-+}} \propto 0.25(1+cos^2\theta)I_o$

The calculations assume an optically thin plasma across the anode surface. Opacity affects the stronger signal more and would reduce the relative strength of the 3/2-1/2 transition compared to the 1/2-1/2 transition. However, for the spectra analyzed here, the ratio of these transitions is usually two, equal to the ratio of their oscillator strengths. Thus, an optically thin plasma is a valid assumption.

5.5.3 Effect of Abel Inversions on the C IV Doublet

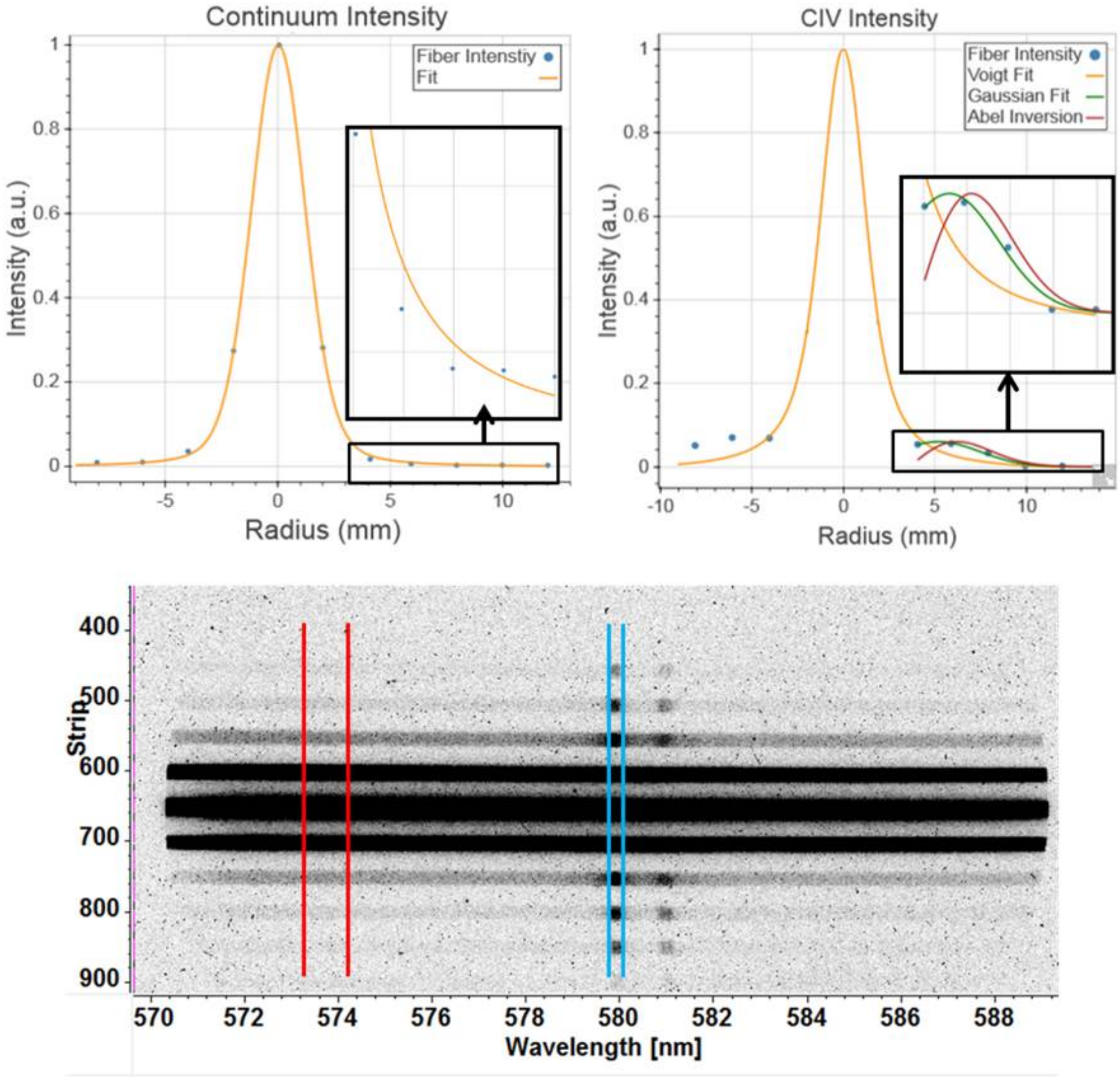

Figure 5.8: Top left: Shot 1919 Voigt fit of the line integrated continuum intensities using the procedure explained in Section 3.6.5. Top right: CIV relative line intensities fit with a Gaussian profile. For comparison a Voigt profile similar to the continuum fit is also shown. An Abel inversion is taken on the Gaussian fit. Bottom: Line-out regions for the continuum intensities (red) and the CIV intensities (blue).

By Abel inverting the data, intensity information can be extracted as a function of radius. This information is then used to weight the simulated Zeeman-split spectrum calculated using the method described in Sections 5.5.1 and 5.5.2. Figure 5.8 compares a lineout along wavelengths where only continuum emission is visible with a lineout taken along the C IV doublet, after the continuum has been subtracted. Since the C IV line may be significantly broadened and blended into the continuum on the central fibers, only spectra with clear C IV line emission are used for the Abel inversion. Unlike the continuum intensities, the C IV line integrated intensity appears to peak at around 6 mm from the beam axis and then begins to fall. Electron temperatures increase as the distance from the axis decreases, and higher ionization states may cause the amount of C IV ions at these locations to drop, leading to a decrease in the doublet intensity.

In order to perform the Abel inversion, the outer fibers are fit with a Gaussian profile. This profile is then Abel inverted and the resulting profile now represents relative intensities as a function of radius, rather than a line integrated measurement. At each discretized point in Figure 5.7 the simulated spectrum is multiplied by the Abel inverted relative intensity to account for the difference in C IV line strength across the anode. After the Abel inversion, the peak shifts slightly to larger radii, because higher intensity contributions to the line integrated measurements have been deconvolved from the spectrum.

Furthermore, the line intensity far from the axis contributes very little to the line profiles on the inner fibers. This suggests that the line of sight contains mostly parallel components of the magnetic field for a cylindrically symmetric beam, and therefore, the pi/sigma ratio will be small. For the 200 μm fiber array, the depth of field is 3.4 cm. Since the C IV line strength is very weak at this distance, in order to reduce computation time, the data are assumed to be line integrated over 2 cm chords.

5.6 Doppler Shifts

Motion in the direction of the line of sight can also cause a spectral line to appear split. When looking across the anode, if there is radial motion, then light from the plasma moving toward the fiber array will appear blue shifted. If the plasma is optically thin, then light from plasma moving away from the array will appear red shifted. The superimposed red and blue shifted spectrum would result in a C IV line that is split. Although a good measurement of radial velocity has not been performed on the SMP diode, an 8-frame camera has been fielded in the past by Mark Johnston. This camera takes 7-8 images, 10 ns apart during the pulse. A set of 8-frame camera images from Shot 1636 is shown in Figure 5.9.

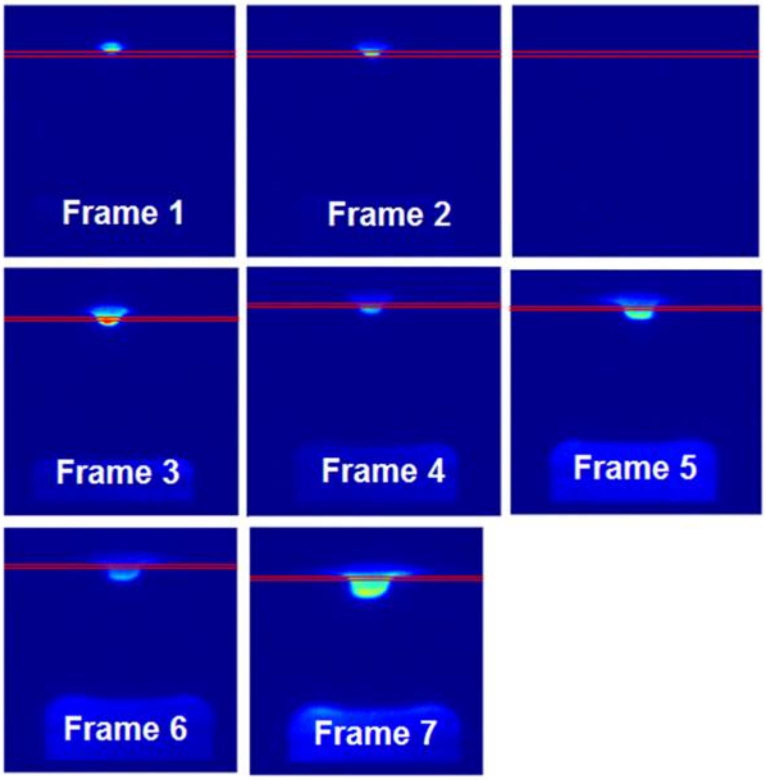

Figure 5.9: Shot 1636 A set of 8-frame camera images taken by Mark Johnston. The red line represents the lineout regions for which the radial plasma expansion rate was determined. Each frame is separated by 10 ns. Frame 8 is not visible for this shot.

This shot is typical of SMP shots, with symmetrically expanding anode plasma. The radial anode plasma expansion is plotted as a function of time to obtain a rough estimate of the radial plasma expansion velocity in Figure 5.10.

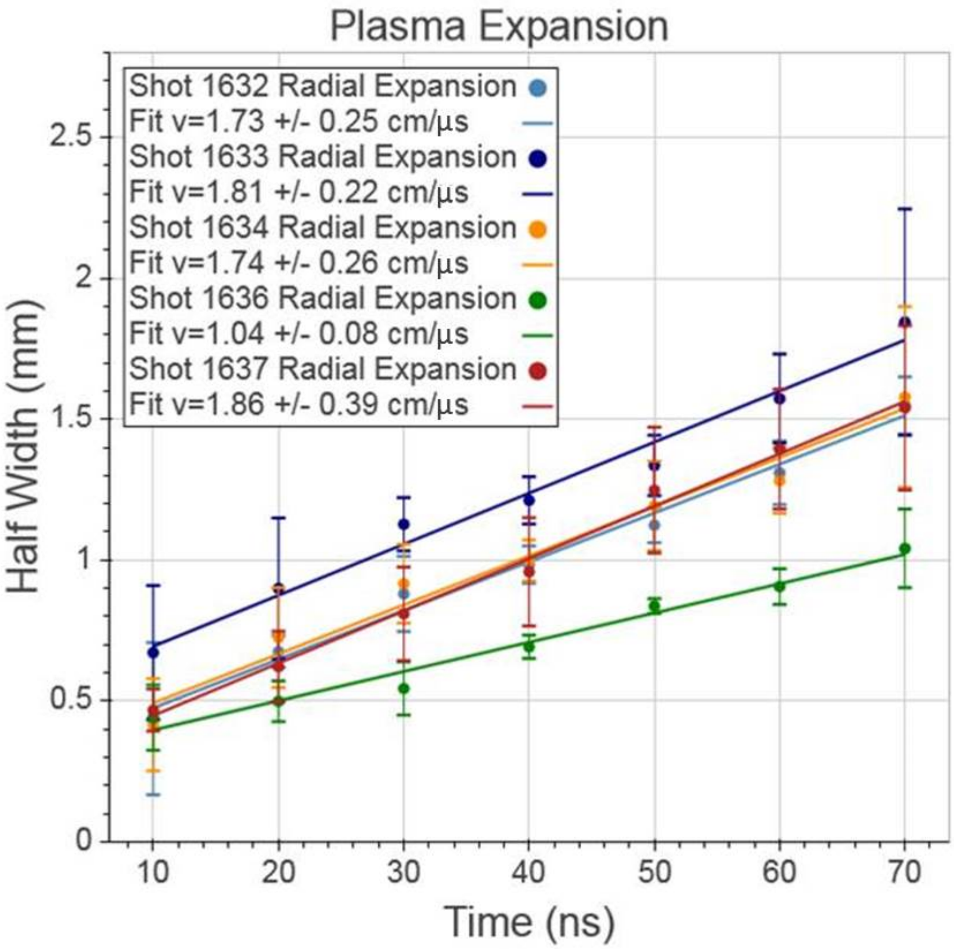

Figure 5.10: Radial plasma expansion and fit from several 8-frame camera image sets.

By fitting the radial expansion as a function of time with a linear fit, the radial velocity can be estimated from the slope of this line. This results in radial ion velocities averaging about 1.64 ± 0.24 cm/µs. But these values are only from the on-axis plasma visible on the 8-frame camera. The plasma in this region is very dense and only continuum emission is measured with spectroscopy. Line emission is measured at radii greater than 2 mm where the electron densities are lower. Still, it is unlikely that there is a large radial ion velocity across the anode when the electric field is mostly axial.

Additionally, this value is likely an over estimate since over time more of the anode surface area becomes thermally excited, and could appear as plasma expansion in the 8-frame camera images. Additionally, as the electron beam expands, a larger surface area is excited by the beam impact. The ion velocity for the most part should be axial, perpendicular to the line of sight, along the electric field direction. As suggested in Figure 4.5, electron temperatures are about 5.5-6.4 eV across the anode surface. For equal ion and electron temperatures the carbon thermal velocity would be about 1.2 cm/μs, which is slightly less than velocities calculated from the 8-frame camera.

The non-relativistic Doppler shift can be calculated using

$$\lambda' = \left(1 + \frac{v}{c}\right) \lambda_o \tag{5.3}$$

where λ' is the shifted wavelength, v is the velocity of the source along the line of sight for a stationary observer, c is the speed of light, and λ_o is the unshifted wavelength. In Figure 5.11 this equation is applied to a simulated C IV spectrum with a Stark width of 0.1 nm and an instrument resolution of 0.065 nm. Since the Doppler shift depends on the viewing angle of the observer, the same discretized algorithm discussed in Section 5.5.2 is used. As the line of sight moves closer to the axis there are more velocity components parallel to the line of sight. The line of sight in Figure 5.11 is located 2 mm from the axis. Even at this close distance, and relatively low Stark width, the Doppler shifts are indistinguishable from the Stark broadening for a 1.6 cm/μs radial velocity. Therefore, a 3.0 cm/μs radial velocity is plotted instead.

A radial plasma velocity on the anode surface would still contain velocity components that are perpendicular to the line of sight, particularly at larger radii. As a result, a spectrum along a chord across the anode would appear less shifted by radial motion than a spectrum produced from a line of sight purely parallel to the motion. The unshifted FWHM is about 0.13 nm for a Voigt profile which consists of a 0.1 nm Lorentzian component for the Stark width and a 0.065 nm Gaussian width for the instrument resolution. The addition of the 3 cm/μs radial velocity results in a FWHM of about 33% larger for a chordal line of sight

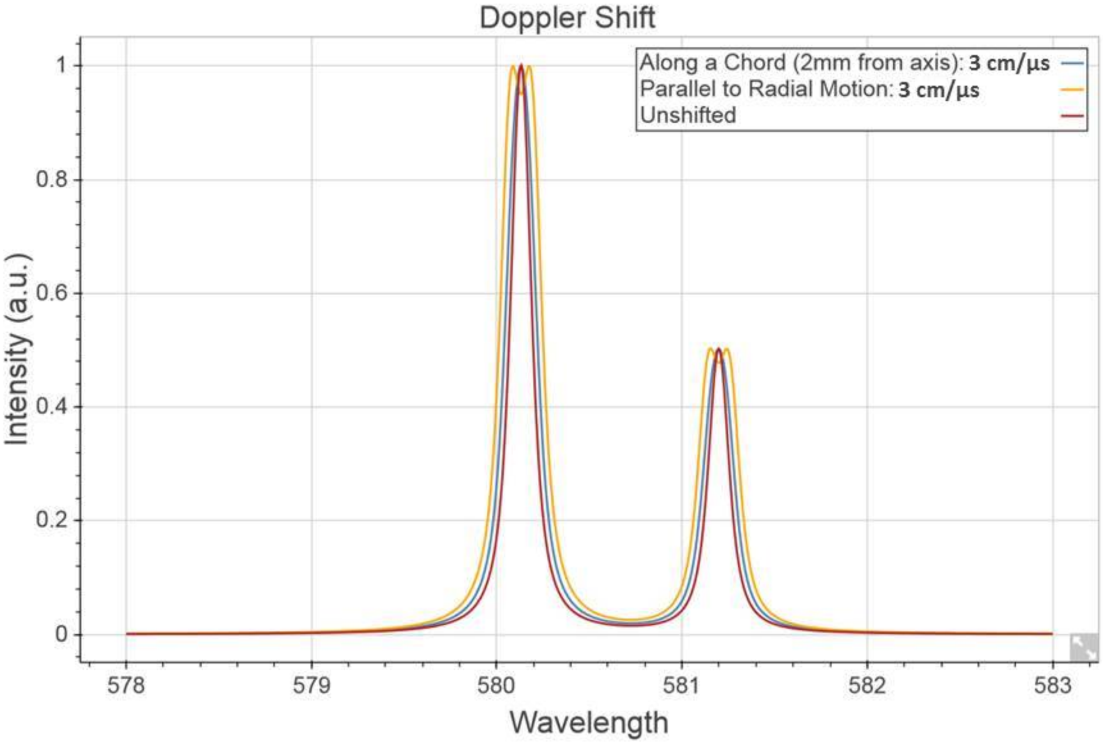

Figure 5.11: Simulated Doppler shifted C IV spectrum for a Stark width of 0.1 nm and an instrument resolution of 0.065 nm. The unshifted Stark broadened line (red) is plotted against a profile in which the line of sight is fully parallel to the radial motion (yellow). A spectrum across a chord in which the velocity is at an angle to the line of sight at discretized locations.

2 mm from the axis, and about 66% larger for a line of sight that is purely parallel to the motion. However, at a radius of 2 mm, Stark widths are greater than 0.15 nm (as estimated from fibers located 3 mm from the axis. At this Stark width and at a velocity of 1.6 cm/µs the FWHM of the unshifted line is indistinguishable from the Doppler shifted line.)

The 1/2-1/2 transition should have the same width as the 3/2-1/2 transition if the spectral line splitting is due entirely to Doppler shifts. However, in the spectral data from the SMP diode there is often a visible difference in the line width between these two transitions. Furthermore, since the outer fibers have smaller components of the radial velocity that are along the line of sight, a large radial velocity gradient would have to be present to account for the line splitting that is visible on these fibers. The outermost fibers would require a 8-10 cm/µs radial ion velocity to measure Doppler split lines along a line integrated chord, while the inner fibers would require 3-4 cm/µs to measurably differ from the larger Stark widths at this location. And so it is very unlikely that the splitting and broadening seen in the SMP spectra are due to Doppler shifted lines from radial motion of the anode plasma. For this reason, Doppler shifts are disregarded in this analysis of Zeeman split lines.

5.7 SMP Diode Current Profiles

5.7.1 Example Spectral Line Fits

The procedure discussed in Section 5.5 is used to fit spectra at discrete radii along the anode surface for multiple shots. Figure 5.12 shows the C IV doublet (at 580.13 nm and 581.20 nm) from Shot 1920 taken at two different radial locations. C IV is contaminant from the oil that is brushed onto the field shaping knob to prevent electron field emission. For comparison, the spectra are also fit without a magnetic field, using simple Voigt profile fit to the spectrum. On Fiber 9, located about 7 mm from the axis, this fit does not accurately replicate the line splitting.

A Voigt fit for Fiber 7, located about 3 mm from the axis, is also shown. The large density gradients present close to the beam axis, both radially and axially, can be approximated as two regions with differing electron density [31]. A fit without a magnetic field could be acceptable if a second higher density component is convolved with the lower density spectrum to accurately fit the wings of the spectral data, as in Figure 5.12. This procedure will be discussed further in the following section. However, on Fiber 7, the $^2\mathrm{P}_{1/2} -^2\mathrm{S}_{1/2}$ (at 581.20 nm) line is wider than the $^2\mathrm{P}_{3/2} -^2\mathrm{S}_{1/2}$ (at 580.13 nm), and as mentioned in Section 5.4, in an optically thin plasma, this effect can only be fit by assuming an external magnetic field, since density broadening is the same for both lines. The FWHM ratio for the $^2\mathrm{P}_{1/2} -^2\mathrm{S}_{1/2}$ to the $^2\mathrm{P}_{3/2} -^2\mathrm{S}_{1/2}$ transition on Fiber 7 in Figure 5.12 is about 1.15, and it is fit by including a magnetic field, as shown in the bottom, right plot.

Since the magnetic field is curved, the varying field angles along the line of sight

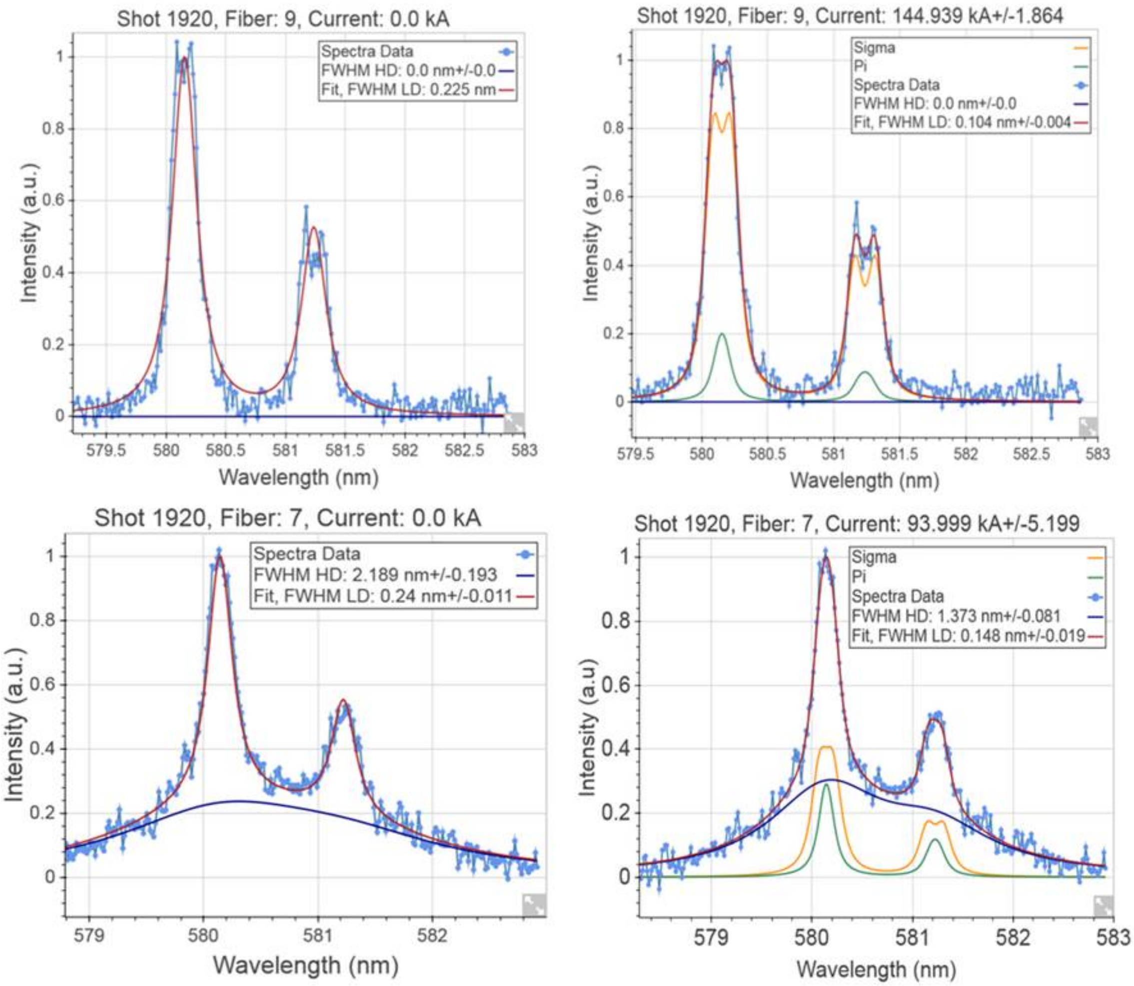
Shot 1920, Fiber: 9, Current: 0.0 kA

Shot 1920, Fiber: 9, Current: 144.939 kA+/-1.864

Shot 1920, Fiber: 7, Current: 0.0 kA

Shot 1920, Fiber: 7, Current: 93.999 kA+/-5.199

Figure 5.12: Spectral line fits for Shot 1920 of the C IV doublet lines, with a magnetic field (right) and without a magnetic field (left). The pi (green) and sigma (yellow) contributions to the total line (red) are also plotted. Fiber 9 is about 7 mm from the axis. Fiber 7 is about 3 mm from the axis, and is fit with a low and high density (dark blue) component.

cause both pi and sigma components to affect the spectrum. Further from the axis the field lines are more parallel to the line of sight and so fibers measuring at large radii will have smaller pi-to-sigma ratios when compared to lines of sight closer to the axis. This is also shown in Figure 5.12, where Fiber 7 shows a much larger pi-to-sigma ratio (~0.7 for the $^2\mathrm{P}_{3/2} - ^2\mathrm{S}_{1/2}$ transition) than Fiber 9 (~0.2). A purely parallel line of sight assumption would result in an underestimate of the current since only the outer sigma lines would be present.

Temperatures from the C III/C IV ratio are estimated to be between 5.5-6.5 eV across the anode, using the procedure described in Section 4.1. Thermal Doppler broadening, from Equation 5.4, caused by the random motion of emitting ions will add to the Gaussian instrument broadening.

$$\Delta\lambda_{Dop} = 2\sqrt{\frac{2ln(2)kT}{m_o c^2}}\lambda_o \tag{5.4}$$

The total Gaussian FWHM of the combined instrument and thermal Doppler profiles is given by

$$FWHM_{G,tot} = \sqrt{FWHM_{inst}^2 + \Delta\lambda_{Dop}^2} \tag{5.5}$$

The instrument width contribution is determined from fitting an Hg calibration lamp, described in Section 3.6.1. This instrument contribution to the Gaussian profile is on average 0.065 nm, while the Doppler contribution is about half this. The typical total Gaussian width contribution to the Voigt profile is around 0.071 nm. Although some of the shots analyzed here do not have temperature estimates from the C III/C IV line ratio, assuming a wide range of temperatures, between 2-7 eV, results in a very small error (5%) in the electron density, estimated from the Lorentzian component of the fit. Since the thermal Doppler broadening equation requires an ion temperature, and line ratio measurements give electron temperature, this error was incorporated in all density calculations, since it is possible the ion temperature is less than the electron temperature. Because external magnetic fields result in fairly distinctive line profiles, the small errors in the temperature estimates change the current measurements by less than 1%.

5.7.2 Current Profile Analysis

Once the spectra are deconvolved, the current profiles can be estimated. The current distribution, determined from the CIV doublet (at 580.13 nm and 581.20 nm) line splitting, is plotted in Figure 5.13 for the six shots summarized in Table 5.1.

A possible systematic error in this plot is due to the fact that Ampere's law, in which

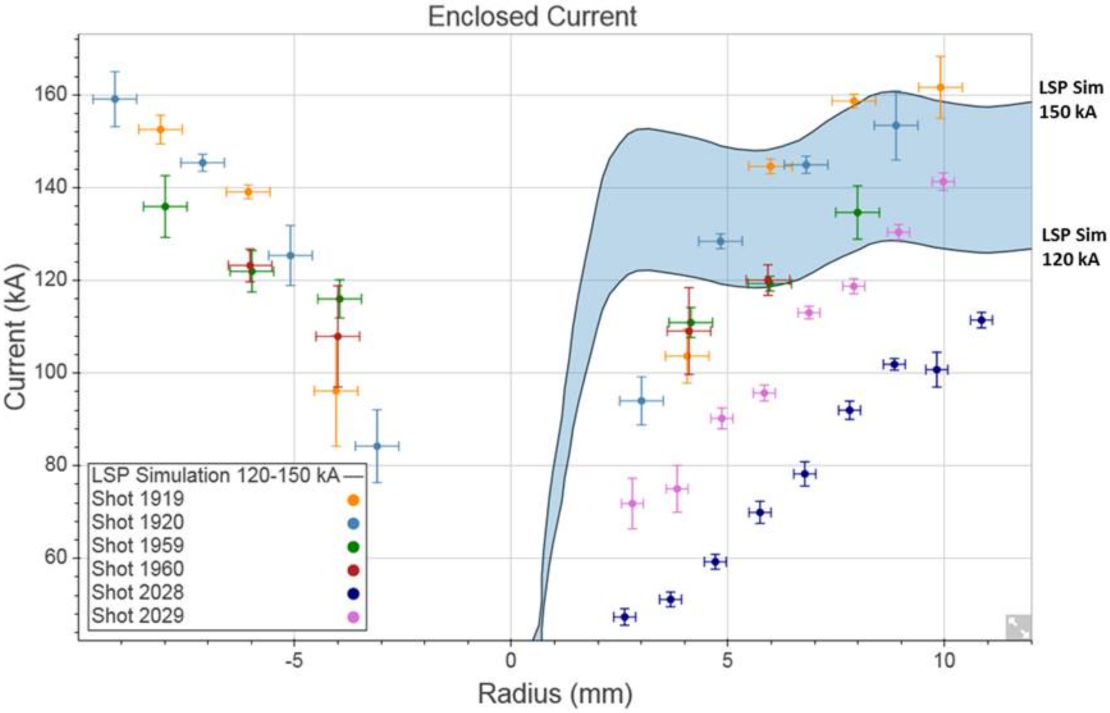

Figure 5.13: Enclosed current estimated from CIV line splitting. Also plotted is an LSP simulation (from Dr. N. Bennett) for a standard SMP diode geometry with an Al foil. The simulation is scaled to match the range of currents measured with B-dots for these shots (120 kA-150 kA). All fits of these data are given in Appendix B.

B scales as 1/r, was used to calculate the enclosed current at discrete points along the line of sight and the resulting profiles were summed (after being weighted by the Abel inverted intensity) at each fiber location, as discussed in Section 5.5. However, Figure 5.13 shows that the enclosed current increases with radius. As a result, C IV line profiles at larger radii along the line of sight may contribute more broadening to the line integrated spectral profile than expected. This would lower the current estimates at the locations shown in Figure 5.13. Consequently, Figure 5.13 represents the maximum enclosed current at each point. The inner fibers would be more affected by this effect since they measure larger magnetic field gradients. Additionally, because the C IV line intensity peaks at about 4-6 mm from the axis, fibers located at <6 mm would again be more affected.

A purely parallel line of sight is a poorer approximation, particularly for the inner fibers. Since the intensity of C IV peaks at 4-6 mm, the pi Zeeman components contribute significantly to the spectrum, as shown in Figure 5.12 for Fiber 7. A parallel line of sight would only contain the outer sigma components and so the spectral line fits would result in current measurements that are too low. However, without localized spectral measurements it is not possible to determine the current distribution more accurately than to calculate the maximum current at each point by assuming that the magnetic field scales as 1/r at each fiber location, which is independent of the measurements at the other locations.

The spectra for Shots 1919-1960 were taken using a single-row fiber array, and each 200 μm fiber was imaged to a 1 mm diameter across the anode surface. As a result, the high density surface plasma, particularly at small radii, is superimposed onto a lower density spectrum. Shots 2028 and 2029 used a double row fiber array, with 100 μm fibers imaged to a 0.5 mm diameter to separate out the high density surface plasma, as discussed in Chapter 4. Because the dimensions of the double array are about half the single fiber array, an edge fiber was aligned to the beam axis to prevent continuum from dominating a large fraction of the array. Therefore, a higher spatial resolution of the anode was achieved at the expense of measuring the radial symmetry visible with the single row fiber array.

These measurements suggest that the enclosed current increases almost linearly with radius. This contrasts with the expected result that all of the diode current is located within a few mm region close to the beam axis. The LSP simulation shows the current distribution at the end of the radiation pulse, and this has been scaled to match the B-dot measurements for these shots, plotted in Figure 5.14, which ranged between 120 kA-150 kA. The oscillating current in Figure 5.13. may be an artifact of the LSP simulation, in which the electron beam has rings of high and low electron densities with very sharp boundaries, leading to space charge effects [68]. The B-dot measurements for these six shots are plotted in Figure 5.14 (measured at position IBEAM in Figure 3.4. The corresponding voltage traces calculated using the method outlined in Section 3.3 are given in Figure 5.15.

Shots 1919 and 1920

Shot 1920 had a silicon-coated tungsten convertor. The Si III line at 574 nm was not

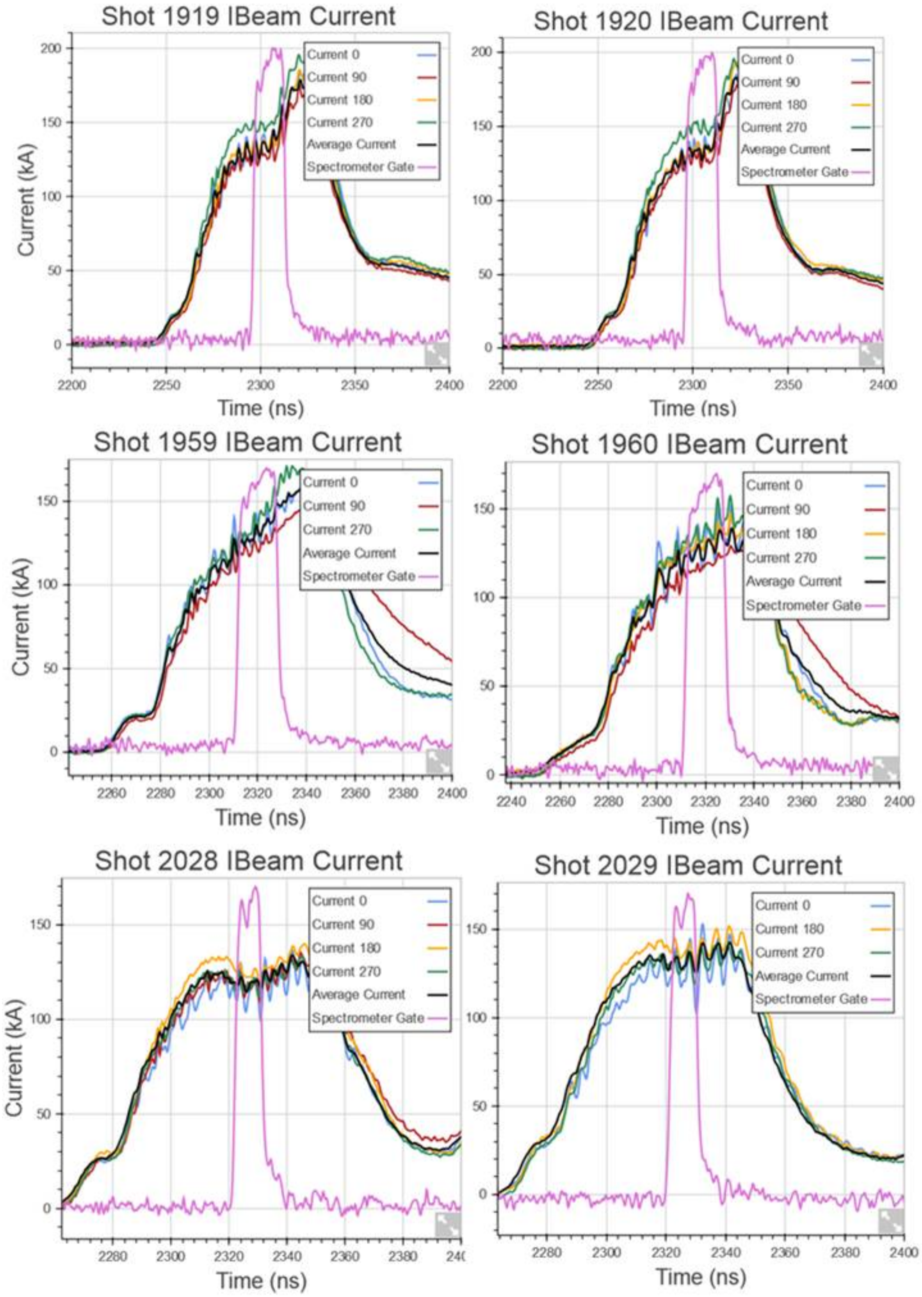

Figure 5.14: Current measured from B-dots (IBEAM) located behind the cathode.

present, most likely because the temperatures were too high in the diode. According to PrismSPECT, if the anode plasma contained similar amounts of silicon and carbon, the Si III line would have been comparable in intensity to the C IV line at 4 eV, and negligible at 5 eV. Shot 1919 had a carbon-coated tantalum convertor, without an Al foil. Yet this coating only marginally improved the carbon signal. For instance, the average of the peak

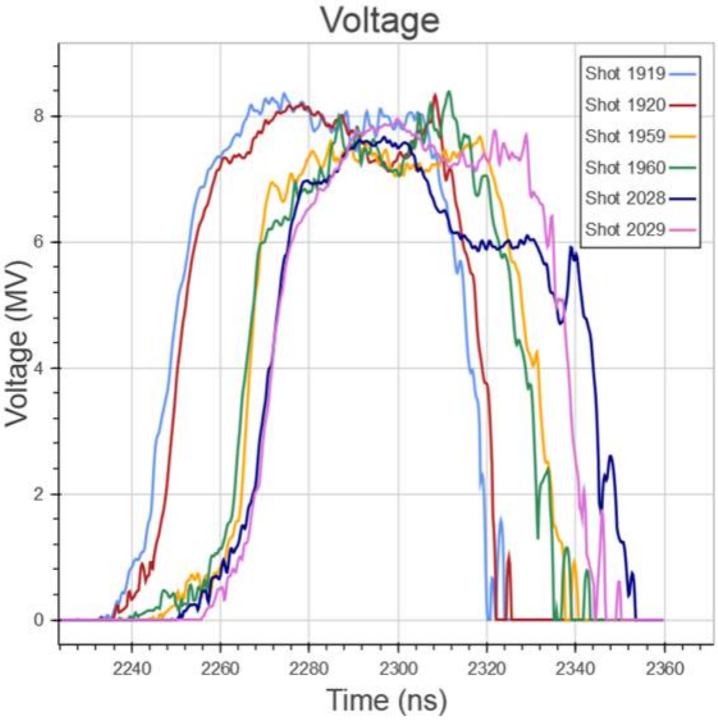

Figure 5.15: The corresponding voltage traces calculated using the method discussed in Section 3.3.

C IV count for Fiber 8 at 4.8 mm and 6.8 mm for Shot 1920 is 255 counts. The peak C IV count for Fiber 8 at 5.8 mm for Shot 1920 is about 290 counts, only about a 14% increase from Shot 1920. Therefore it is probable that much of the carbon signal was from contaminants on the diode surface. B-dots, located behind the cathode, measured currents around 130-155 kA within the spectrometer gate for both of these shots.

Shot 1959 and 1960

Shots 1959 and 1960 were on standard SMP diodes and B-dot traces showed currents between 125-140 kA, within the ICCD gate. Zeeman splitting measurements, also suggest that these Al-foil shots had slightly lower current densities than Shots 1919 and 1920. The lower signal-to-noise ratio on these shots prevented current estimates from the line splitting at larger radii.

Typically, B-dot traces suggest that bare or coated converters have slightly higher currents than the standard Al-foil SMP diode, as is shown in Figure 5.14, in which Shots 1919 and 1920 show 5-15 kA higher currents from the B-dot measurements than Shots 1959 and 1960 over the duration of the ICCD gate. Zeeman Current profile measurements, in Figure 5.13 also show that Shots 1919 and 1920 have an enclosed current that is 15-20 kA higher than 1959 and 1960 at 8 mm.

Additionally, Shots 1919 and 1920, exhibited rapid impedance collapse, during which the current increased sharply to 155 kA and the radiation pulse ended. Part of the ICCD gate for both shots was at the start of this impedance collapse, and the sharp increase in current may have also resulted in higher current densities, assuming that the beam expansion within the first 5 ns of the impedance collapse was not rapid enough to significantly lower the current density.

Shot 2028

Shot 2028 had an Al-coated tantalum convertor, without a foil. The results shown here were taken from the top row of fibers which are positioned about 0.5-1 mm from the anode surface. The spectra from this shot contained strong line splitting, even on fibers close to the axis due to the lower densities. Typically, these Al-coated anodes do not perform well. They usually have shorter radiation pulses (less than 40 ns) with current traces that indicate rapid impedance collapse.

However, in this shot the voltage dropped by nearly 2 MV, shown in Figure 5.15, for the second half of the pulse, and the current stayed flat at around 115-120 kA. This resulted in a full radiation pulse of 50 ns. Still, the current profile for this shot is significantly lower than the other five shots, as seen in Figure 5.13. TRSD data, discussed further in Section 5.7.3, showed an unusual amount of beam motion, and rapid spot expansion during the 10 ns spectrometer gate. The lower voltage and rapid spot expansion would result in a lower current density. Also, the beam motion that was integrated over the spectrometer gate may also have weakened the apparent line splitting, since multiple magnetic field strengths and a potentially asymmetric and changing current distribution, would be convolved into the spectrum.

Shot 2029

Shot 2029 had a NaCl-coated converter plate. This shot also used the double array, but in contrast to Shot 2028, the bottom set of fibers, closest to the anode, was fit for Zeeman splitting. Unfortunately, the array positioning is done by eye, and since the strong axial density gradients occur within a millimeter of the anode surface it is difficult to align every shot within a 0.5 mm axial distance. In this case, the array appears to have been offset further from the surface than in Shot 2028, and the second row of fibers had spectral lines that are too weak to fit. The comparison of the raw spectral data for Shots 2028 and 2029 is presented in Figure 5.16 and Figure 5.17.

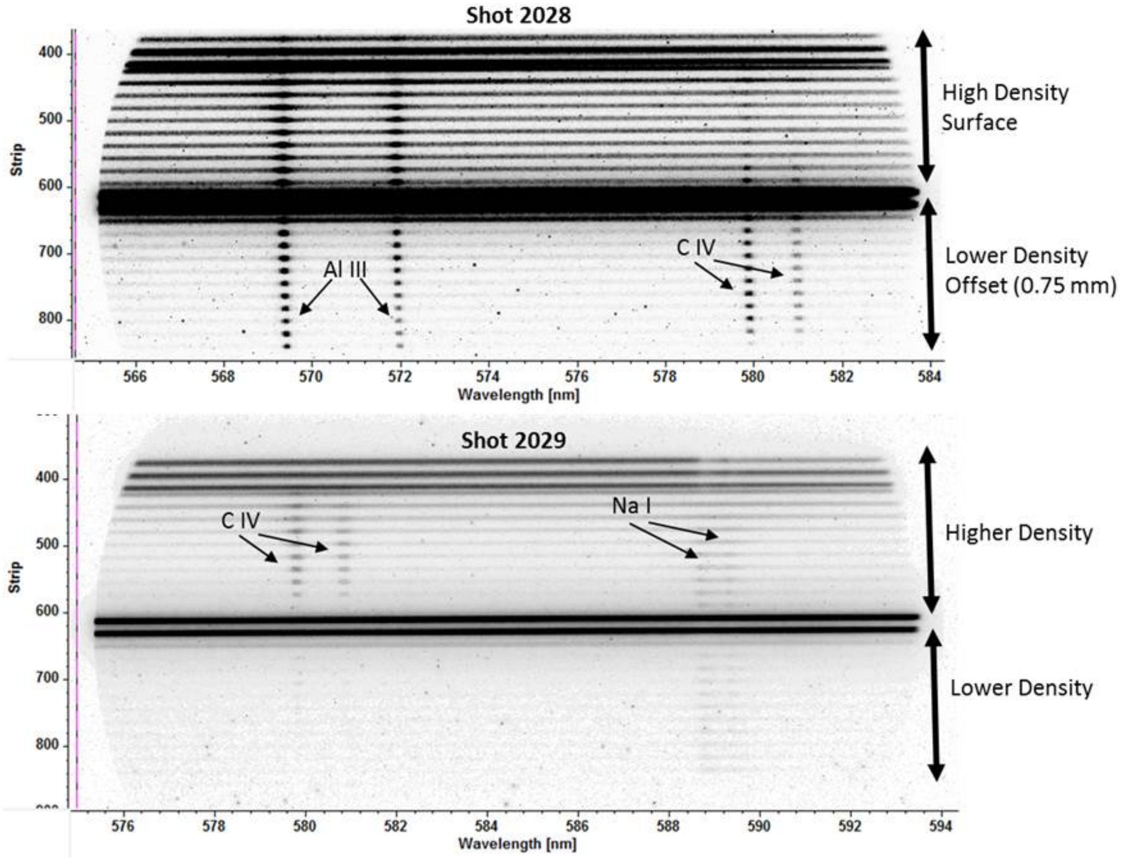

Figure 5.16: Raw spectral data for Shot 2028 and 2029. The lower density components of the spectra are further from the axis. The lower density CIV lines were used for the line splitting analysis in Shot 2028, and the higher density lines were used in Shot 2029. The fiber alignment for Shot 2029 may have been too far from the anode surface for strong lines on the fibers further from the surface.

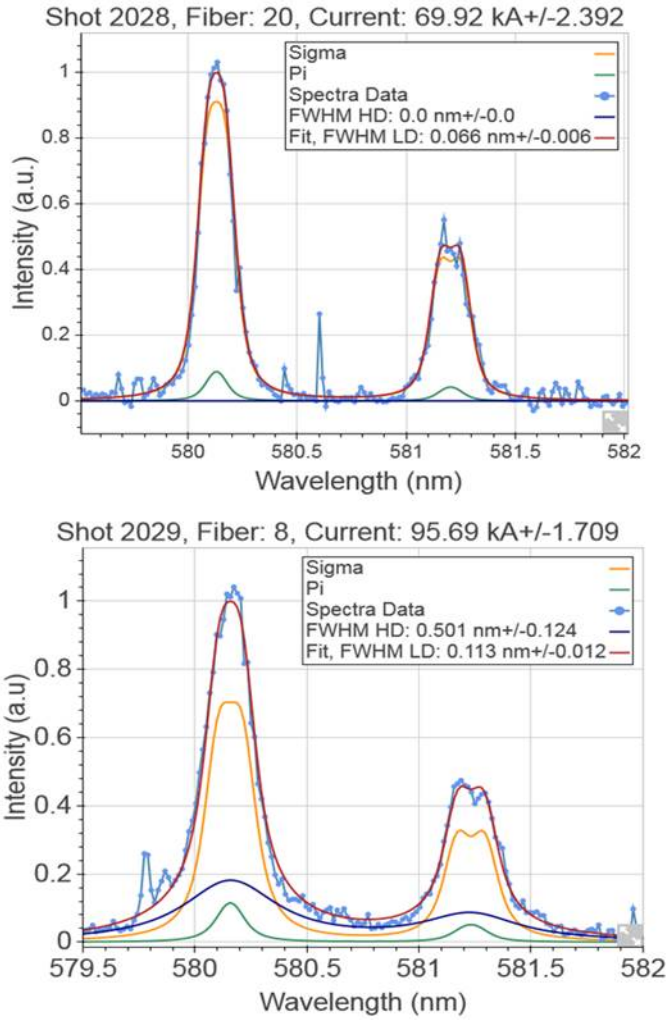

Figure 5.17: Comparison of Shot 2028 (Fiber 20 at 5.7 mm) and Shot 2029 (Fiber 8 at 5.9 mm). The spectra located further from the anode surface have a much lower density.

Shot 2029 performed extremely well, with a full (48 ns) radiation pulse. The few Na-coated diode shots on RITS-6 have all resulted in full radiation pulses. Current traces for this shot suggest the diode current was about 130 kA, similar to the Al-foil diodes, for the duration of the spectrometer gate. However, while the array imaged the Al-foil in Shots 1959 and 1960 at a slight angle to the surface, it imaged parallel to the bare convertor surface in Shot 2029. In addition, the spectra from Shot 2029 show similar electron densities to Shots 1919 and 1920, shown in Figure 4.12 despite the lower B-dot measurements. These three shots all measured the convertor surface with fibers imaging parallel to the surface. Since the array used in 2029 was smaller, it is likely that that the spectra were taken closer to the target surface, and it is possible that the beam defocuses close to the surface. Ions produced on the target would partially neutralize the electron beam, which would help pinch the beam and move the new focus further into the gap. The beam would then be over-focused at the target [7, 8]. Unfortunately, Shots 2028 and 2029 had only one row out of two that had large enough spectral signals to fit line splitting. With better alignment, it may be possible to fit splitting on both rows and determine the difference between the current density at the surface and 0.5-1 mm off the surface.

5.7.3 Comparison with Simulation

The LSP simulation suggests that most of the diode current is located within a 2.5 mm radial distance from the beam axis. In order to obtain currents that match the LSP simulations, the CIV fits would have to be drastically different from the data, particularly for Shot 2028. Using the average current measured from the B-dots, the best fit for spectra taken at 2.6 mm and 2.9 mm is plotted in Figure 5.18. The simulation suggests that essentially all the current should be located within these radii. On Shot 2028 the best fit, assuming all 120 kA is within a 2.6 mm radius, suggests that the line broadening is due entirely to the instrument, which is not possible. On Shot 1920, the fit shows a clearly split $^2\mathrm{P}_{1/2} -^2 \mathrm{S}_{1/2}$ transition (at 581.20 nm), which is not seen in the data. In addition, the Lorentzian width of the line is very similar to the widths of the outer fibers, which would suggest the electron density is uniform across the anode. Ultimately, the C IV spectral lines appear to be fit more accurately with lower current densities.

Additionally, the LSP simulations do not predict the fast spot growth that is often measured using the TRSD. Usually, the beam pinches to a minimum rapidly, within the first half of the radiation pulse, and then it begins to expand. This dynamic is shown in Figure 5.19 for Shots 2028 and 2029.

As mentioned earlier, Shot 2028 had significant beam motion (4 cm/us), and rapid spot

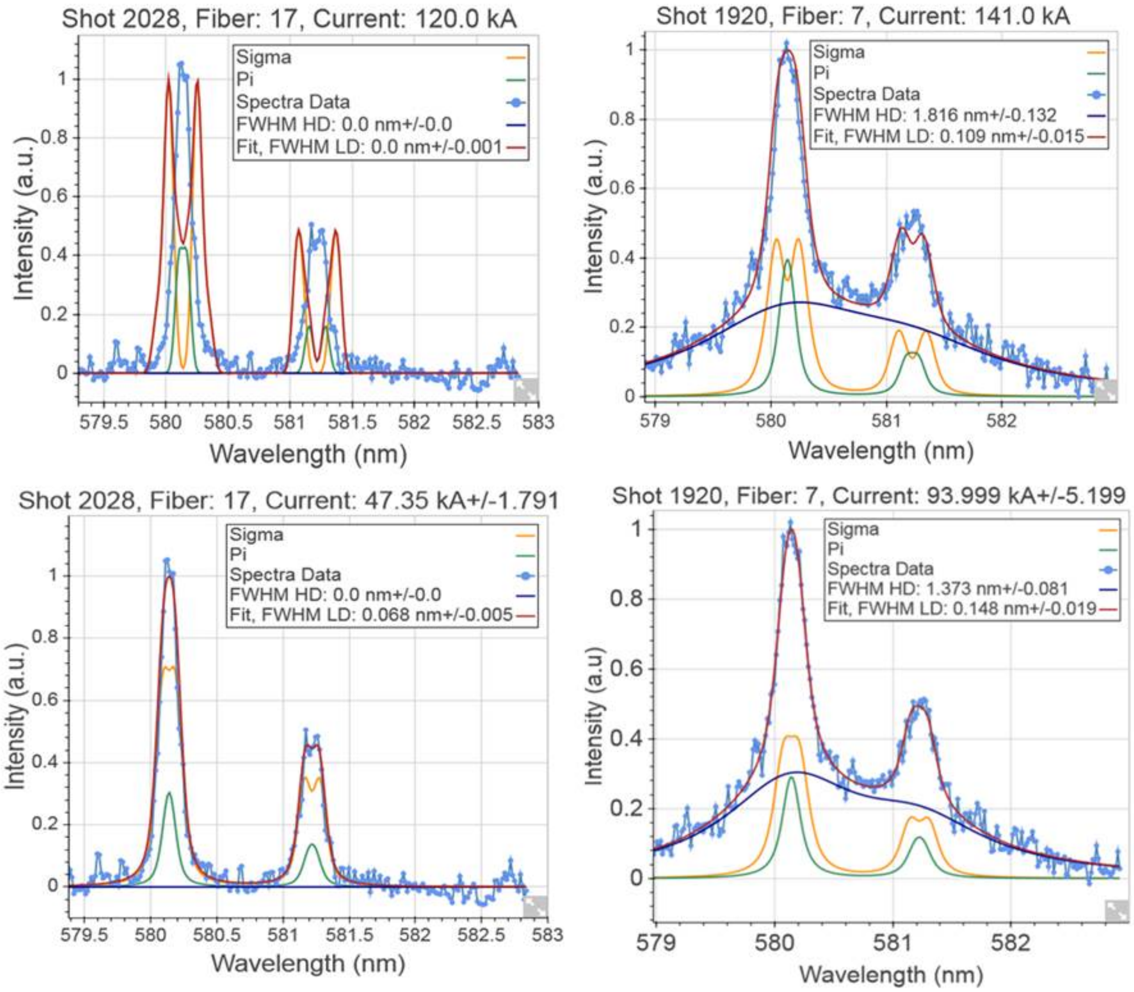

Figure 5.18: Spectra from two shots, 2028 (at 2.6 mm) and 1920 (at 2.9 mm) are fit using the average current measured with B-dots (Top). The fits are very different from the data, particularly for Shot 2028. Because of the low density at this axial location, the Zeeman split spectrum clearly does not fit the data. The best fit for these lines (bottom) involve a lower current.

expansion (1.75 mm at the minimum spot diameter to 3.5 mm by the end of the ICCD gate), possibly due to a 2 MV drop in voltage. Shot 2029 only expanded by about 0.5 mm from the minimum spot size to the end of the ICCD gate. The spot expansion seen in both shots may result in lower current densities than what simulations would predict during the middle-end of the pulse, when the spectra are taken. However, this expansion cannot entirely explain the discrepancy between the Zeeman splitting estimates and the LSP simulation, because final measured spot sizes are still typically within the radii at which the Zeeman effect is

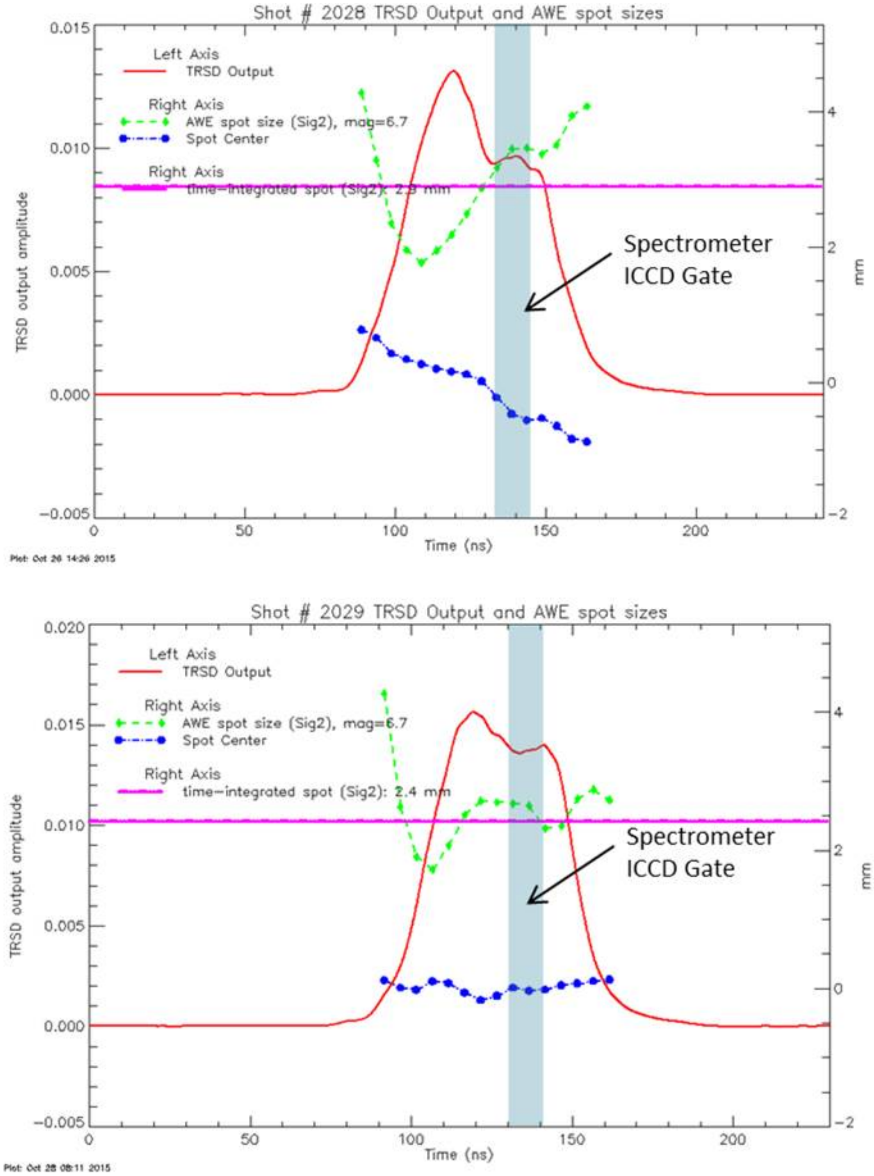

Figure 5.19: TRSD data for Shots 2028 and 2029 (From T. Webb). The spot expansion (green) and spot motion (blue) is plotted with the x-ray pulse (red).

visible.

Although a significant portion of the current appears to be outside the x-ray spot region, the current density, in Figure 5.20, rapidly increases toward the axis, as expected. The data, excluding Shot 2028 (which had a sudden, 2 MV voltage drop), are fit with an exponential curve. While measurements of line splitting closer to the axis are not possible with the C IV line at the anode surface due to high electron densities, it appears as though the

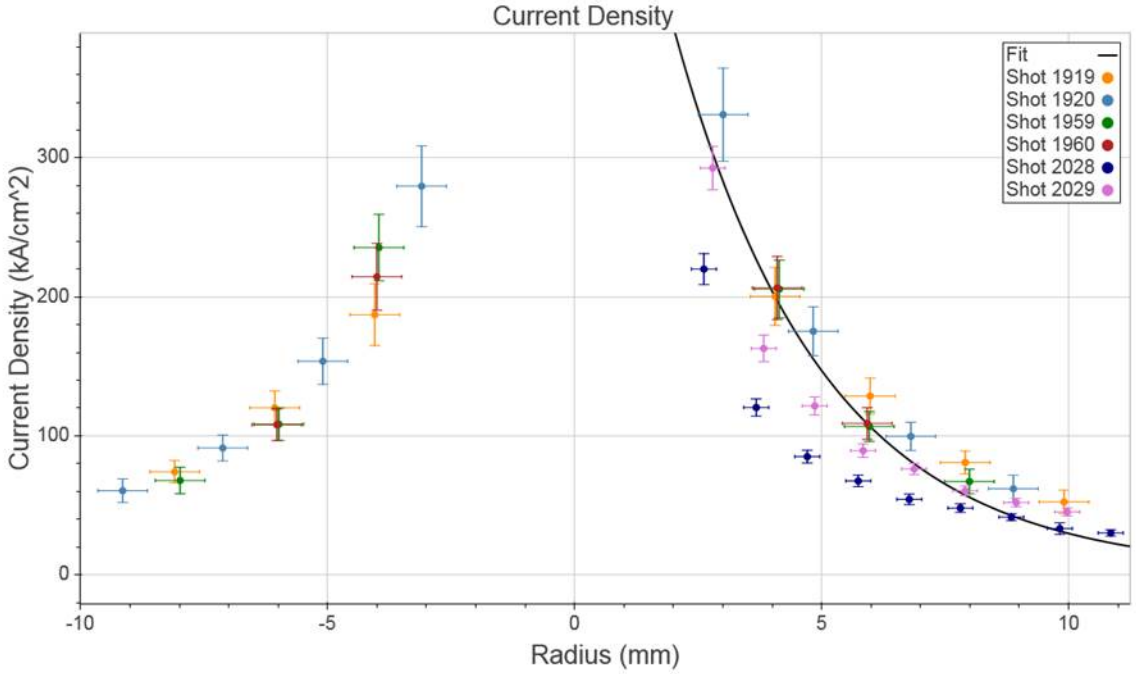

Figure 5.20: Current density calculated from the enclosed current. These data are fit with an exponential decay function.

current density should continue to increase approximately exponentially toward the axis. Consequently, even though the current appears to be distributed more evenly across the diode than expected, the x-ray spot could still be small, with a longer tail that is partially attenuated in the TRSD and image plate measurements.

5.7.4 Diamagnetism

Shown in Figure 5.21 is a plot of magnetic field profiles calculated from the current profiles. The 1/r decay of the magnetic field, if all of the current (120-150 kA) were enclosed within these measurements, is also plotted. The expected magnetic field is larger at small radii than the measurements show. This could be due to a diamagnetic effect. Large density and temperature gradients are present close to the axis and they may partially screen the beam current's magnetic field. This effect would be more pronounced at small radii where the pressure gradients are the largest.

A simulation by Dr. Nichelle Bennett in Figure 5.22 shows the ion density near the

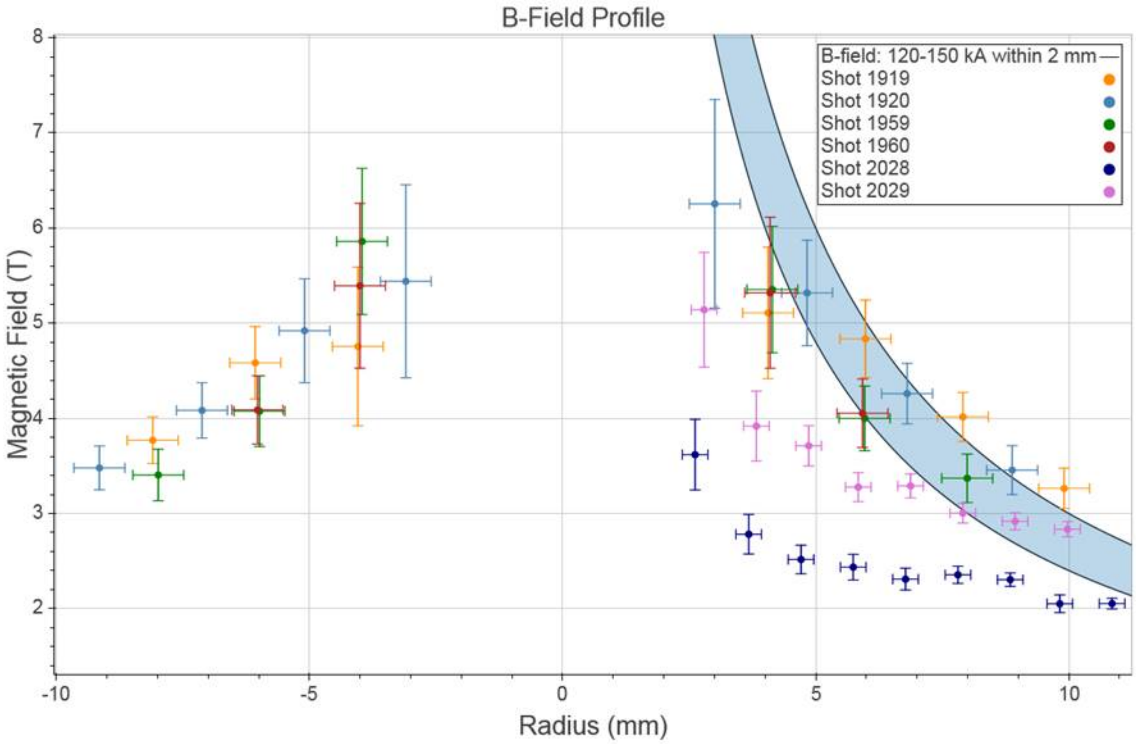

Figure 5.21: Plot of the magnetic field profiles. The B-field for all of the current (120-150 kA) located within 2 mm of the axis is also plotted in the blue band.

anode surface at the end radiation pulse, for a standard SMP diode configuration. It shows a large density gradient close the beam axis. The dense, on-axis, plasma extends about 1 mm into the AK gap, with a radius of about 2 mm on the anode surface. Similarly, the on-axis plasma, seen in the framing camera image in Figure 5.1 for Shot 1959, extends 1.2 mm into the AK gap and 2.14 mm along the anode surface. At larger radii, plasma emission is not seen in the framing camera image. Since the intensity of the bremsstrahlung and recombination continuum intensity is proportional to the square of the electron density [69], it is likely that electron densities at these locations are too low to be imaged with the 10 ns time gated camera.

Spectroscopy measurements also suggest a sharp density increase near the axis. Line emission is usually visible at a radius of $>$2.5 mm, and within 1 mm the spectrum becomes continuum-dominated. Stark broadening measurements of the diode suggest electron densities are about 4-5$\times 10^{17}$ cm^{-3} at 2.5-5 mm from the axis, decreasing to 1-2$\times 10^{17}$ cm^{-3} at

8-10 mm from the axis. These measurements, particularly at large radii, are higher than what is predicted in the simulation below, and they indicate that the experimental density decreases more gradually.

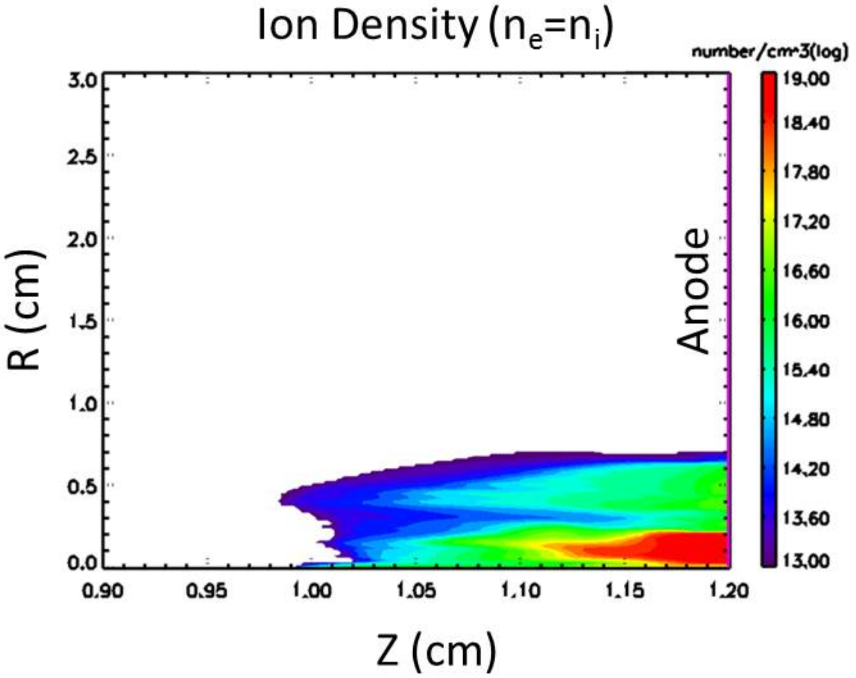

Figure 5.22: LSP simulation by Dr. N. Bennett for ion near the anode surface densities in the SMP diode near the end of the radiation pulse.

Chen's textbook [70] has a derivation for the diamagnetic drift, starting with the equation of motion,

$$mn\left(\frac{\partial \mathbf{v}}{\partial t} + (\mathbf{v}\cdot\nabla)\mathbf{v}\right) = qn(\mathbf{E} + \mathbf{v}\times\mathbf{B}) - \nabla p \tag{5.6}$$

Assuming the drifts are much slower than the time scale of the cyclotron frequency, and ignoring second order effects,

$$0 = qn[\mathbf{E}\times\mathbf{B} + (\mathbf{v}_\perp \times \mathbf{B})\times\mathbf{B} - \nabla p \times \mathbf{B} \tag{5.7}$$

$$0 = qn[\mathbf{E}\times\mathbf{B} + \cancel{\mathbf{B}(\mathbf{v}_\perp \cdot \mathbf{B})} - v_\perp B^2] - \nabla p \times \mathbf{B} \tag{5.8}$$

After rearranging,

$$v_{\perp} = \mathbf{E} \times \frac{\mathbf{B}}{B^2} - \nabla p \times \frac{\mathbf{B}}{qnB^2} \tag{5.9}$$

The second term in this equation is the diamagnetic drift which opposes the external magnetic field. Because the ions and electrons drift in opposite directions, a diamagnetic current forms. For $n_e = n_i$ the current density is,

$$j_D = \frac{\mathbf{B} \times \nabla(n(kT_i + kT_e))}{B^2} \tag{5.10}$$

Electron temperatures measured from the C III/C IV line ratios are between 5.5-6.5 eV. Temperature measurements from the continuum near the beam axis have not been estimated. However, LSP simulations indicate ion temperatures are about 10 eV on axis and decrease to 2 eV at a 2 mm radius.

For the plot in Figure 5.23, Ti=2 eV from LSP, and Te=6 eV, from C III/C IV line ratio measurements. As an approximation, the temperatures are assumed to be constant across the diode. The density is assumed to peak at 10^{19} cm^{-3} at 2 mm to match the LSP simulation, decreasing to about 2×10^{17} cm^{-3} at 8 mm, to match the Stark broadening measurements. An exponential function is used to approximate the density profile and obtain a diamagnetic current density from Equation 5.10, assuming that a current of 130 kA is located within the 2 mm radius.

With a sharp pressure gradient, the diamagnetic current could play a large role in the measured current profiles in Figure 5.13. Additionally, because the diamagnetic current partially cancels the imposed magnetic field, B-field measurements should be lower than expected, as in Figure 5.21, close to the axis where the gradients are largest. Using the diamagnetic current density, shown in Figure 5.23, the enclosed current (including the diamagnetic effect) can be calculated assuming the beam current is located with 2 mm of the axis. This is plotted in Figure 5.24. For comparison, the electron beam current is also plotted assuming a uniform beam current density and a 2 mm beam radius.

After including the diamagnetic current, the total current (130 kA) is enclosed at about

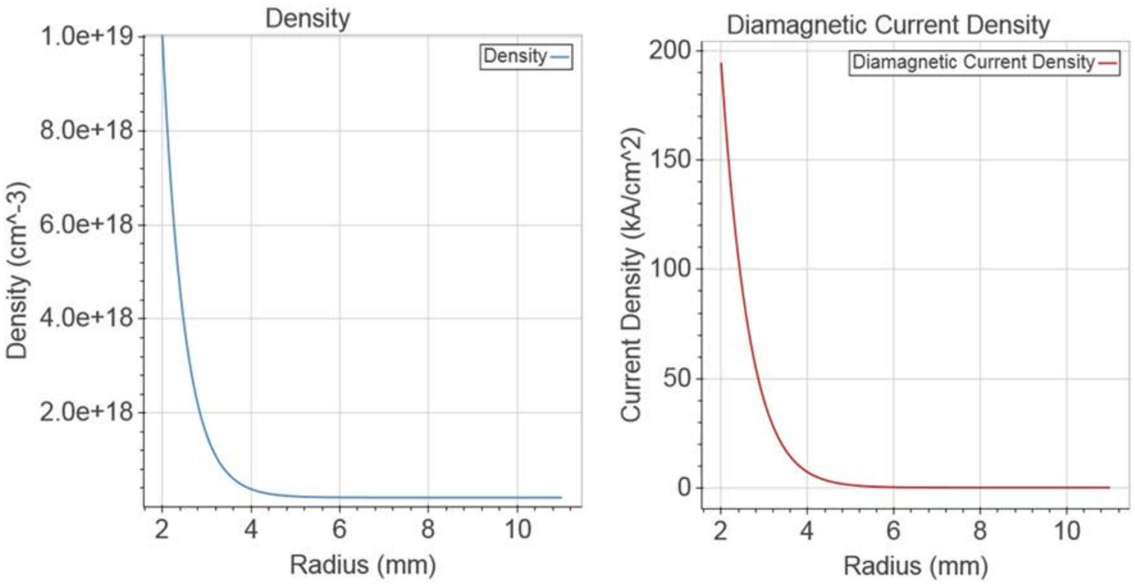

Figure 5.23: Figure 5.23 An exponentially decaying density profile (left) is shown, and the corresponding diamagnetic current density (right) is plotted.

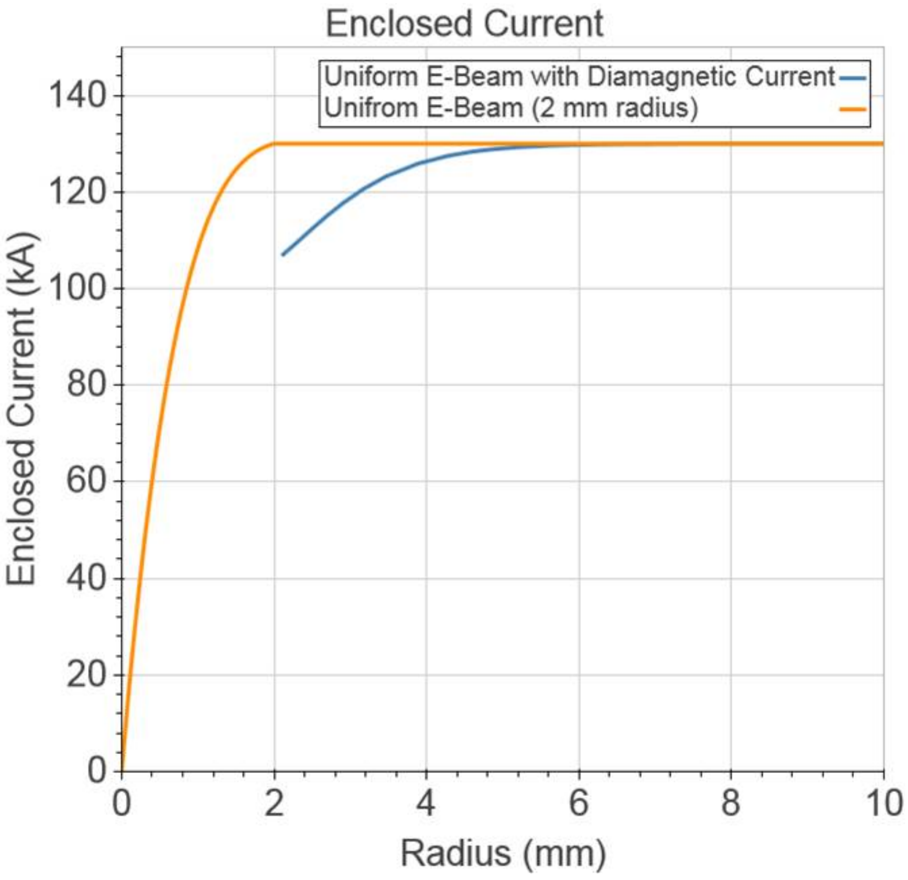

Figure 5.24: Enclosed current, including the diamagnetic effect.

a 5 mm radius, rather than a 2 mm radius. Although this plot replicates the shape of the measured enclosed current values in Figure 5.13, the measured values are still lower. However, the diamagnetic current density was estimated assuming a uniform temperature for ions and electrons across the anode surface, and it is expected that there is also a large temperature gradient at the beam radius. Additionally, estimates of the on-axis ion density were taken from LSP simulations which simulated singly ionized carbon. If plasma densities are larger than simulations suggest, then the diamagnetic current will have an even larger effect. Also, the addition of sheath current at large radii, will cause the enclosed current to increase to values larger than what is measured by the cathode B-dots. This is discussed in the next section.

Diamagnetism is also expected to play a role in Z-pinch experiments [71]. This reference suggests that although the current in a Z-pinch is carried on-axis, the axial current density could be uniformly distributed through the plasma due to the diamagnetic electron orbits, as pictured in Figure 5.25. A similar effect could be present in the SMP diode.

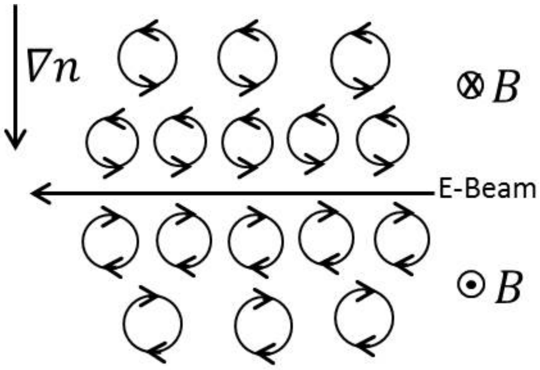

Figure 5.25: Sketch of stationary electron orbits due to an electron beam.

In the case of the SMP diode, usually the spot pinches to a minimum just before the peak of the radiation pulse. The density gradients should increase with time as the beam continues to ionize the anode surface. This could then increase the diamagnetic screening of the beam magnetic field. The lower B-field may cause the spot to eventually expand, as is seen in the TRSD measurements.

5.7.5 Sheath Current

The CIV doublet (at 580.13 nm and 581.20 nm) intensity at radii larger than 10-11 mm becomes extremely weak, preventing an estimate of the current density using this line. But from Figure 5.13, it does appear as though the total current may continue to increase to values larger than what the corresponding B-dot traces estimate. Four B-dots, placed symmetrically behind the cathode stalk, measure the current within a 6.35 cm radius. A second set of four B-dots located past the anode, measure the current within an 11 cm radius. An LSP simulation [35], shown in Figure 5.26, shows the MITL sheath current wrapping around the field shaping knob and impacting the anode downstream of the cathode B-dots.

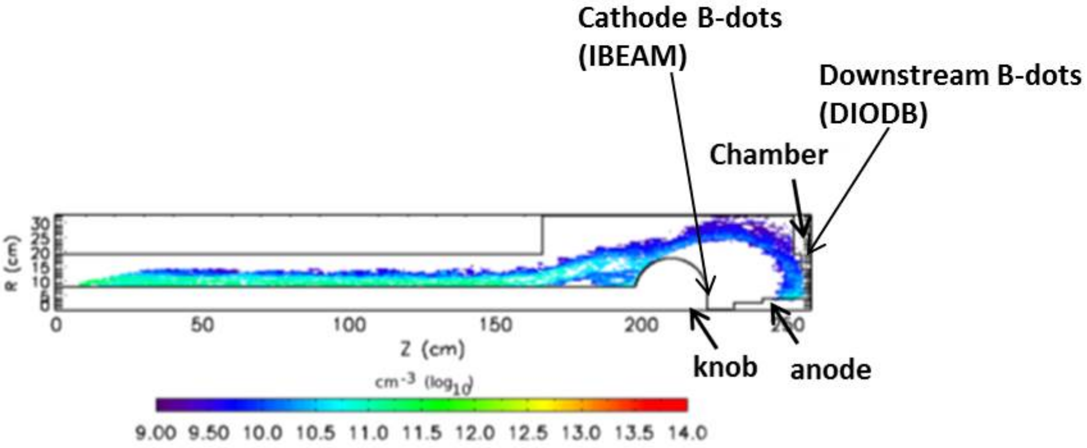

Figure 5.26: LSP simulation of the sheath current electron density [35]. The sheath current wraps around the knob and strikes the anode and outer chamber wall.

The downstream B-dots, on the chamber, typically measure currents that are about 50 kA higher than the cathode B-dots, as shown in Figure 5.27. If the some of the sheath current wraps around the 6.35 cm radius where the B-dots are located and enters the diode at the anode surface, the cathode B-dots would not register it. Current at large radii is also suggested by damage on the anode surface, and x-ray pinhole images which show emission at large radii.

Electron densities at 1 cm from the axis, estimated from C IV Stark broadening are about 10^{17} cm^{-3} and appear to be at least two orders of magnitude larger than the LSP simulation in Figure 5.22. The addition of the sheath current at large radii may further ionize the anode surface. Emission from the field shaping knob outside the 6.35 mm B-dot radius could also impact the anode, and increase the current measured from line splitting. Since the high current densities at large radii appear to be a symmetric effect, the sheath current connecting with the diode or uniform emission from the knob seems more likely than localized knob emission.

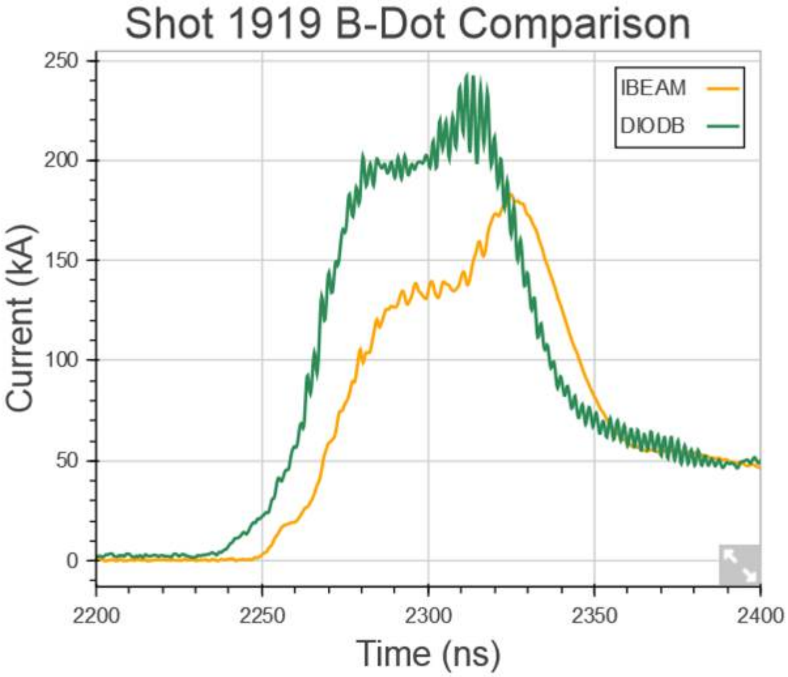

Figure 5.27: Comparison between the beam B-dots, located behind the cathode (orange), and the downstream B-dots (green), located past the anode. The cathode B-dots measure the diode current (within a 6.35 cm radius), and the downstream B-dots measure some of the sheath current (within an 11 cm radius) in addition to the diode current.

5.8 Dopants

Initially, dopants that are not typically found in the SMP diode were used to coat the entire anode convertor surface with the intention of identifying spectral lines which have high enough signals to spatially isolate the diode measurements by coating a portion of the anode. A thin film deposition technique was used for the majority of these shots, with a coating thickness of about 1 μm. Several of the Al-coated converters were coated using a plasma thermal spray technique, resulting in a few hundred micron thick coating.

5.8.1 Aluminum

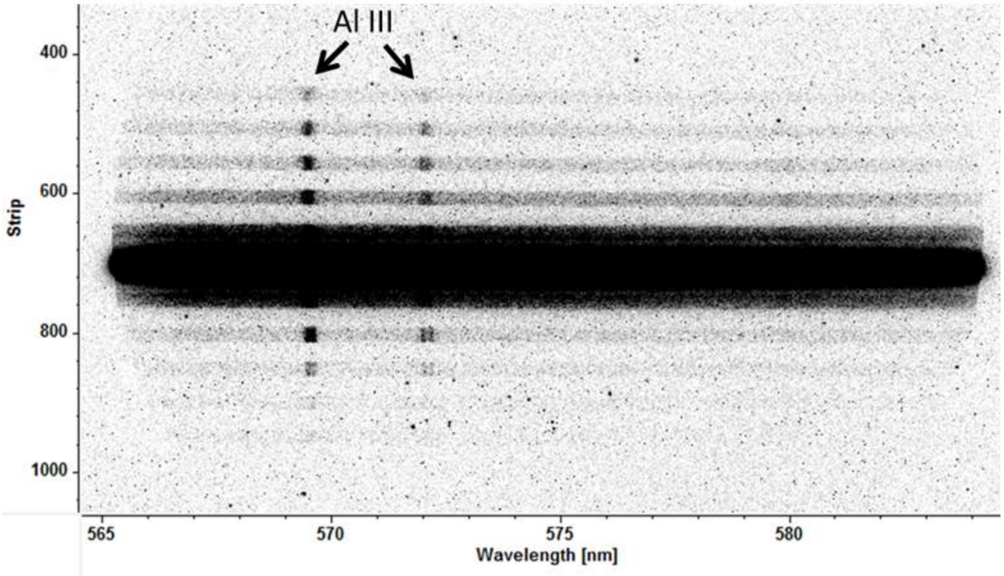

Figure 5.28: Raw spectral data for Shot 1925 which had Al thermal spray coated target. Strong Al III (at 569.7 nm and 572.3 nm) lines are visible.

Aluminum-coated targets resulted in strong Al III lines at 569.7 nm and 572.3 nm. For example, Shot 1925, shown in Figure 5.28, had an Al-thermal spray coating. This shot used a shorter, 8.3 mm AK gap, and an 8.5 mm diameter cathode to increase the current density. Typically these sub 1 cm AK gap shots have shorter pulse lengths than the corresponding standard SMP shots. For instance, while Shot 1925 had an x-ray radiation pulse length of about 14 ns, Al thermal spray coated targets with a standard SMP AK gap and cathode diameter of about 1 cm resulted in an average pulse length of 37 ns.

The 15 ns spectrometer ICCD gate for Shot 1925 was taken during the fall of the radiation pulse, when the current rose from 110 kA to 180 kA. Although Zeeman splitting is measured on this shot, and is visible on Fibers 8 and 9 in the raw spectral data, the splitting is asymmetric. The anode plasma formation also appears asymmetric, as shown in Figure 5.29.

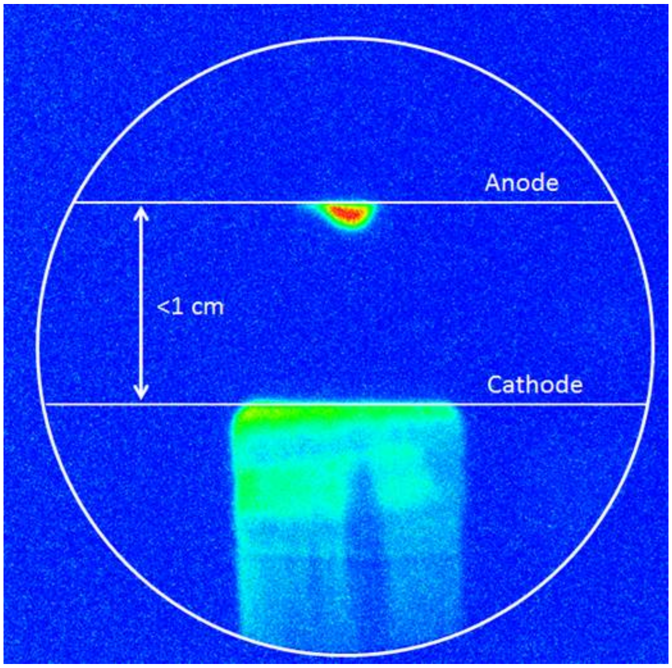

Figure 5.29: Shot 1925 self-emission image of the SMP diode, taken with a 10 ns gate during the fall of the radiation pulse. The anode plasma appears asymmetric, with a lower intensity tail on the left side.

The splitting was fit for two fibers on opposite sides, 4 mm from the axis. A parallel line of sight to the magnetic field is assumed. Due to the asymmetrical splitting measured in the spectra and seen in the framing camera image, a current estimate was not obtained since cylindrical symmetry may not be a valid assumption for this shot. The best fit, in Figure 5.30, for these spectra suggest a magnetic field difference of about 1.3 T between the two measurement locations.

The strong Al III lines suggest that aluminum could be used to coat a portion of the target surface and still provide reasonable signals. A thin strip across the diameter of the anode would localize the measurement. The Abel inversion of the line intensity would not be required, and the spectra would not contain the superposition of multiple field strengths and angles. In this case, the magnetic field would essentially be parallel to the line of sight for a cylindrically symmetric beam. In Shot 1946, a 3 mm stripe across the anode resulted

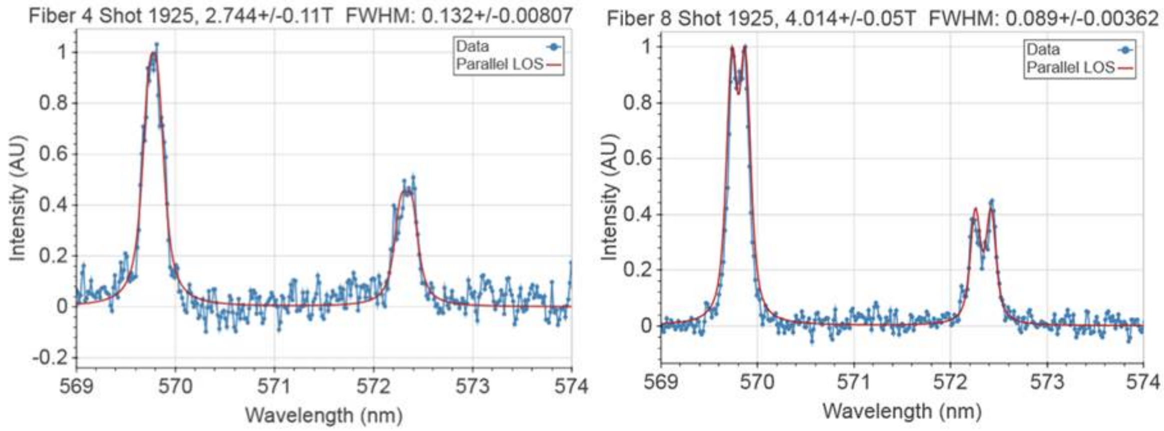

Figure 5.30: Spectra from two fibers (blue), located 4 mm from the axis, are fit assuming a magnetic field (red). The magnetic field is assumed to be parallel to the line of sight and cylindrical symmetry is not assumed.

in strong Al lines.

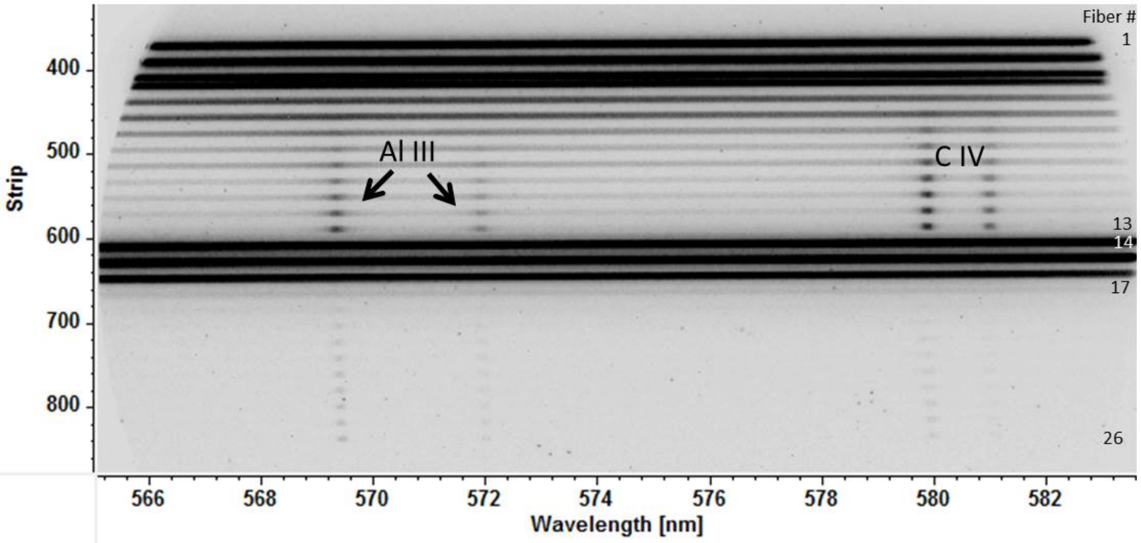

Figure 5.31: Raw spectral data from Shot 1946. The anode surface was coated with a 3 mm stripe across the target diameter.

Splitting was not measured on Shot 1946, in Figure 5.31, (with the possible exception of Fiber 26), due to the fact that the spectra were taken during the impedance collapse, when the AWE spot diameter from TRSD measurements was about 4 mm. A potential disadvantage of using this line for Zeeman splitting measurements is the presence of the C III line, also at 569.6 nm, the same location at the Al III $\mathrm{P}_{3/2} - \mathrm{S}_{1/2}$ transition, could obscure the splitting. Still, the $\mathrm{P}_{1/2} - \mathrm{S}_{1/2}$ transition would be unaffected, and if the C III line is present, the ratio of $\mathrm{P}_{3/2} - \mathrm{S}_{1/2}$ to the $\mathrm{P}_{1/2} - \mathrm{S}_{1/2}$ transition would be greater than two. Consequently, the strong signal to noise ratio of the Al III line on the diode surface makes this a good candidate for future localized splitting measurements.

5.8.2 Boron and Silicon

Shot 2024

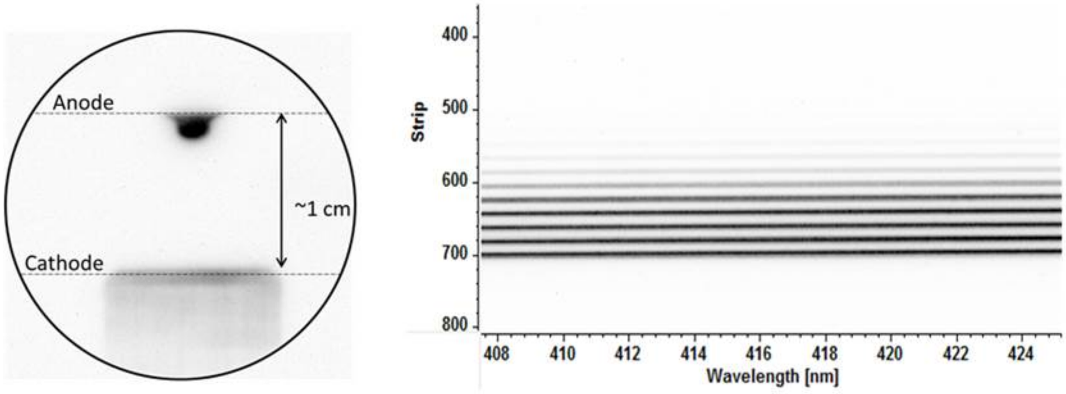

Shot 2025

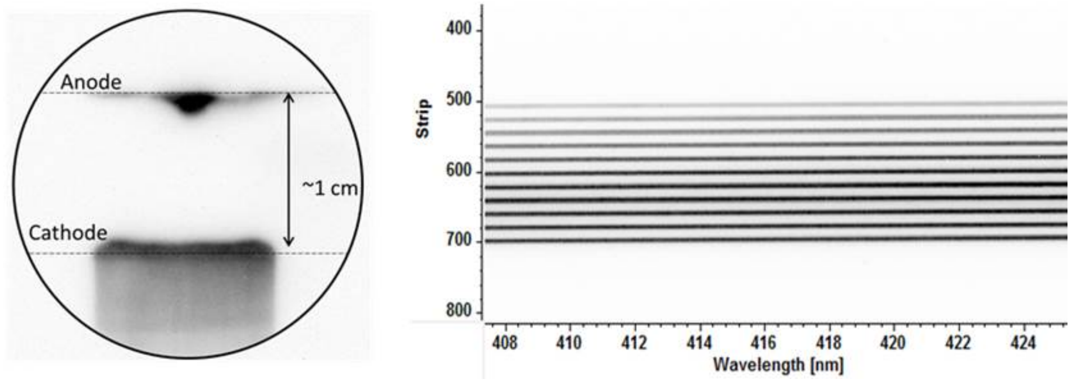

Figure 5.32: Boron coated tantalum target shots. Boron lines were not visible, and both shots show mostly continuum, particularly Shot 2025 which also shows dense plasma formation across the anode surface.

Shots 2024 and 2025, in Figure 5.32, were taken with boron coated convertors in order to measure B III lines at 424.4 nm and B II at 412.2 nm. Both shots used a single row

100 μm array, with an edge fiber positioned at the anode center. Typically only the 2-3 fibers closest to the axis are continuum dominated. Shot 2024 had a 38 ns pulse. However, while the framing camera image looked normal, the spectra showed intense continuum up to about 5-6 mm from the axis. For example, Shot 2023, discussed in the next section, had an average of about 150 counts of continuum about 5 mm from the axis. In contrast, Shot 2024 had an average of about 5000 counts. Shot 2025 was even more continuum dominated than Shot 2024, with counts greater than 10,000, about 10 mm from the axis. This is also seen in the framing camera image, where dense plasma has formed along the entire anode surface. The radiation pulse length for this shot was also very short at around 16 ns.

TRSD data for these shots show significant spot motion (2.6 cm/µs for Shot 2024). Shot 2025 had a discontinuity in the spot location, suggesting that the beam pinched onto the anode at two different radial locations over the course of the radiation pulse. Additionally, the shorter pulse lengths for these two shots, resulted in measurements that were taken after the end of the radiation pulse, when the x-ray source spot rapidly expands. These two effects could account for the measured spectra which shows continuum across much of the fiber array.

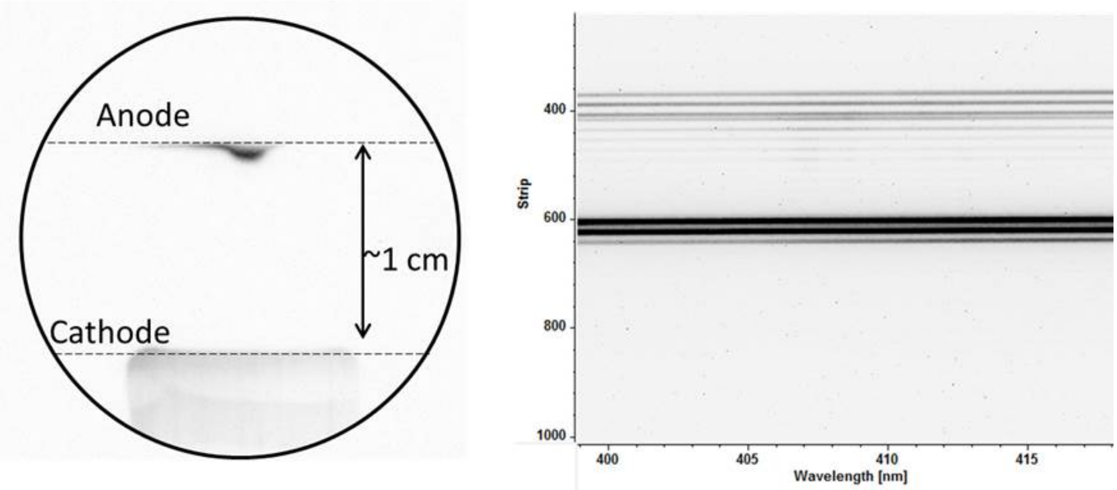

Figure 5.33: Framing camera image (left) and raw spectral data (right) for Shot 2030 on a Si-coated target.

Shots on two silicon-coated targets were also performed. Shot 1920 was discussed in

Section 5.7.2. It had a 31 ns radiation pulse, and Zeeman splitting was measured on C IV lines. However, the Si line at 574 nm was not measured. Shot 2030 also had a Si coating. Weak Si II and/or Si IV lines at 412 nm may be present but are at most 20-40 counts above the continuum. Figure 5.33 shows a framing camera image and spectra for this shot. Like the B-coated target in shot 2025, this shot also had plasma formation along a large section of the anode.

5.8.3 LiF, NaCl, and MgF2

The Li I doublet at 670.8 nm has a small fine structure separation of about 0.015 nm, and so the line would be in the Pachen-Back regime for the magnetic fields measured on RITS-6. Although strong Li I lines were measured, plotted in Figure 5.34, line splitting was not measured. Like the H-alpha line discussed in Section 4.2.1 it is possible that the neutral Li I line is located far from the beam axis where the magnetic fields are too low to measure. Also like H-alpha, the width of the Li I line does not change with the fiber position. Therefore, because these measurements are line integrated across the anode surface, it is also likely that the neutral lithium measurements across all the fibers were located at comparable radii in a ring around the axis, as shown in Figure 4.21 for H-alpha

Shot 2035, which had a Ta convertor with a 3 mm stripe of LiF across the diameter showed no Li I emission at this wavelength while a ring of LiF outside a 20 mm diameter showed the Li I line, which again suggests that most of the neutral lithium emission comes from radii greater than 12 mm, the length of the array. The LiF coated shots resulted in an average radiation pulse length of 45 ns, provided the coating was within the beam diameter.

NaCl coatings also resulted in full radiation pulse lengths which averaged about 46 ns. The purpose of this coating was to measure splitting on the Na I doublet at 589.0 nm and 589.6 nm, but the line was barely visible in Shot 2029 as seen in Figure 5.16. For similar quantities of Li and Na, the line intensity of Li I 2s-2p and Na I 3s-3p is equal from 0.5 eV to 3 eV, but by about 4.5 eV the line intensity of Na I is almost negligible compared to

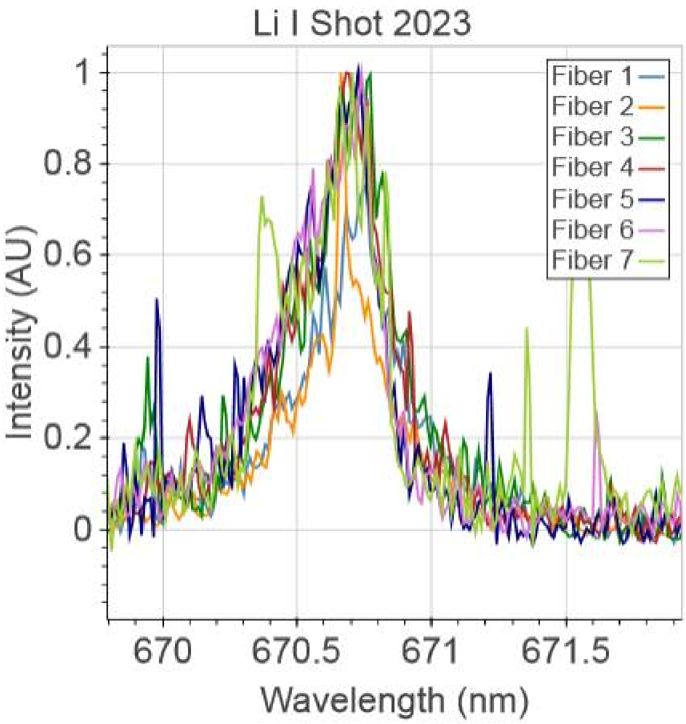

Figure 5.34: Li-Coated target shot. Lineouts from fibers 4-10 mm from the axis are shown. Since the spectra have similar widths, they are likely from the similar radii.

that of Li I, according to a PrismSPECT zero width, non-LTE simulation. MgF2 was also tried as a target coating in order to measure Mg I at 552.8 nm, but this line was also not measured during the shot. However, the shot performed well with this coating and a full radiation pulse of 44 ns was achieved.

5.8.4 X-ray Radiation Pulse Length Comparison

Although Zeeman splitting was successfully measured only on C IV, a non-localized contaminant, and Al III, the coatings appear to have affected the performance of the SMP diode. Shown in Figure 5.35 is a plot of the radiation pulse length vs. the average atomic number of the coating. The majority of the coatings were full surface coatings. Several of the coatings were 3 mm stripes and 20 mm diameter circles centered on the axis but since these two coating geometries were within the electron beam radius on the target surface, they are also included in the plot.

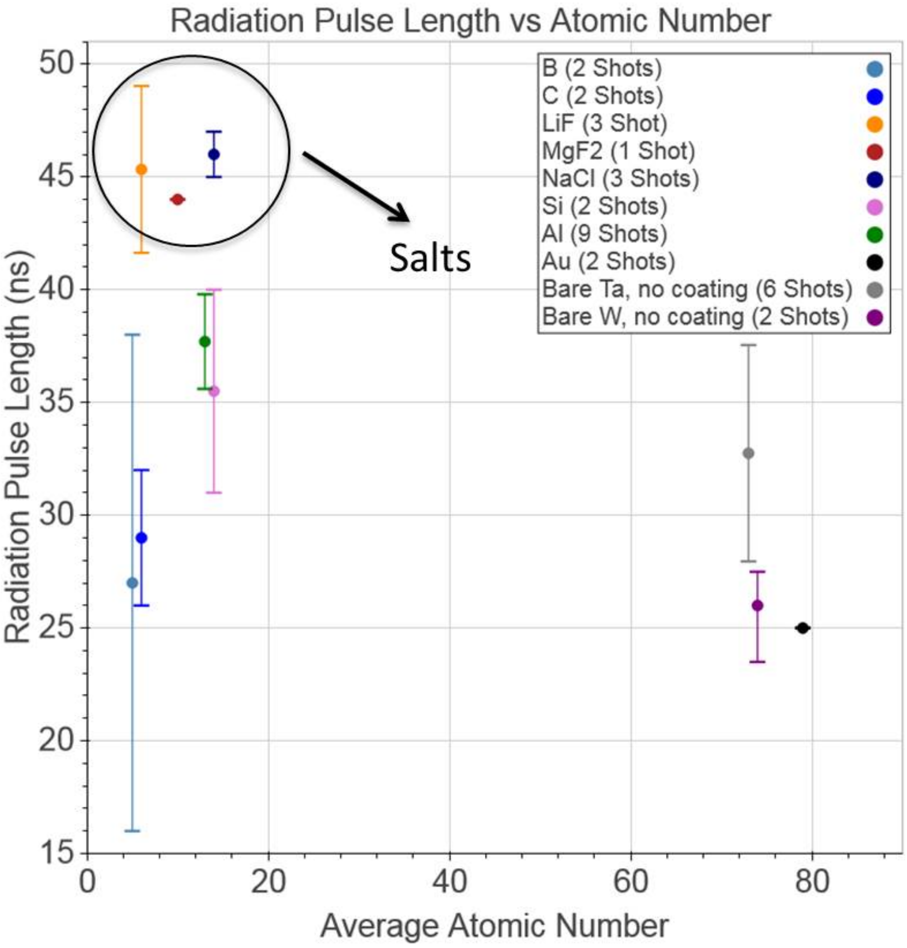

Figure 5.35: Radiation pulse length vs atomic number. There does not appear to be a correlation between the atomic weight of the coating and the pulse length. The plot only includes shots which had an 80 kV charge voltage and a 12 mm AK gap and cathode diameter.

AK gap closure from hydrocarbon contaminants is thought to eventually short the diode, and end the radiation pulse. The lightest atoms and ions should determine the rate at which this occurs [5]. As seen in Figure 5.35, there does not appear to be a correlation between the radiation pulse length and the atomic weight of the coating. If the gap closure is primarily due to hydrogen contaminants on the anode surface [72–74], then higher Z coatings should not reduce the pulse length significantly. Yet the gold coating resulted in the shortest pulse length of the coatings shown here. However, gold may not have been transparent to the electron beam. As a result, more of the beam energy could have been deposited near the coating surface and have more easily desorbed contaminant monolayers that form on the electrode surfaces.

Still, the salt coatings resulted in full pulse lengths that were on average about 15-20 ns longer than the transition metal surfaces and about 10 ns longer than the metals and semimetals. CsI coatings have also been shown to slow diode gap closure [75, 76]. Extending the radiation pulse is particularly important for radiographic diodes because the x-ray dose and pulse length are roughly proportional. A few these coatings have only two shots, and, particularly for the boron-coated shots which resulted in very different pulse lengths of 38 ns and 16 ns, more statistics are needed to draw definitive conclusions.

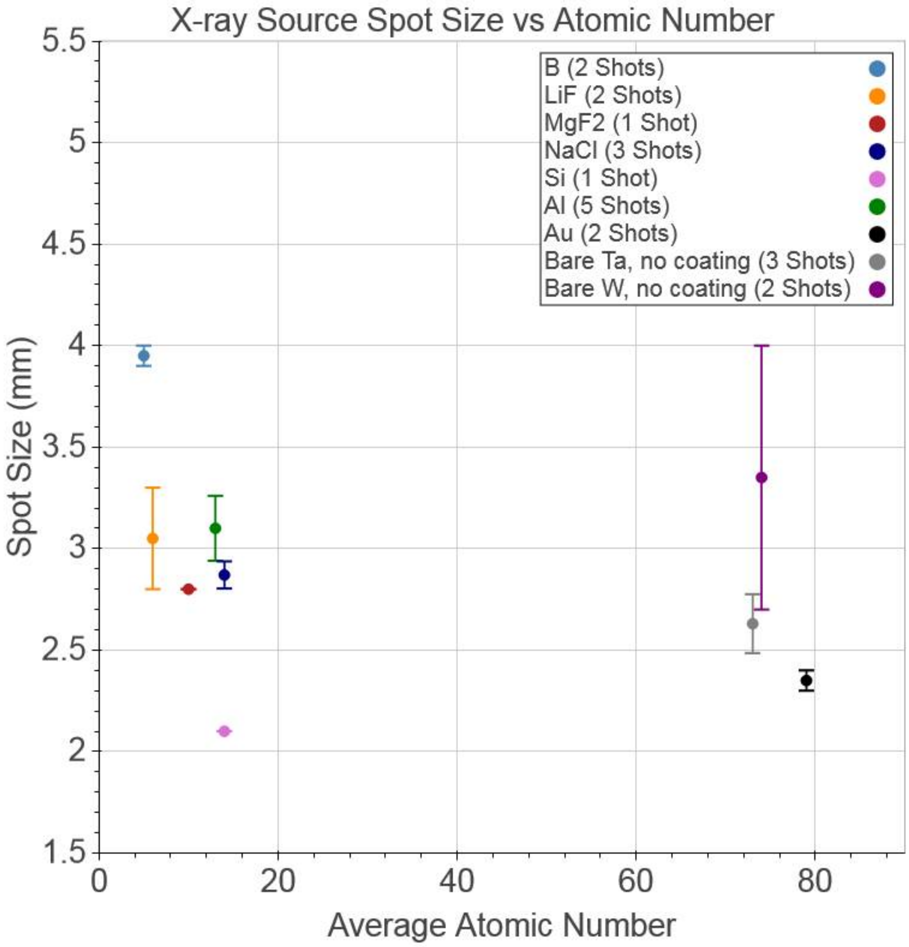

Figure 5.36: X-ray source spot size vs atomic number, for shots which had an 80 kV charge voltage and a 12 mm AK gap and cathode diameter.

X-ray source spot sizes (using the AWE metric, discussed in Section 3.7) are also plotted as a function of atomic number in Figure 5.36. The salt and aluminum coatings resulted in similar spot sizes that were on average about 3 mm in diameter. Correlations between spot sizes and atomic number for the other coatings do not appear to be present, but like in Figure 5.35 more statistics are needed for several of these coatings.

CHAPTER 6

Conclusions

The RITS-6 accelerator has served as a test bed for the development of flash radiography sources. This thesis, in particular, studied the SMP diode in which a hollow cathode emits electrons through an approximately 1 cm vacuum A-K gap onto a high Z material. The electron beam pinches from its own magnetic field as it crosses the gap [16]. Plasmas that form on the surface expand into the gap and eventually short the diode ending the x-ray radiation pulse [4]. Consequently, measurements of the magnetic field and electrode plasma formation yield insights into the diode physics which can benchmark SMP diode simulations and help improve future diode designs.

A standard SMP diode geometry consists of an aluminum foil offset by about 0.8 mm from a tantalum converter plate. The anode surface plasma was characterized using optical spectroscopy. Initially, a single row, 11 fiber, 200 μm array imaged the surface onto a low resolution (0.15 m) spectrometer. These measurements suggested the anode plasma consists mainly of hydrocarbon contaminants and aluminum from the foil. Streaked spectra confirmed this plasma composition. Streaked spectroscopy also indicated that the spectral line intensity is greatly increased by removing the Al foil and imaging a bare or coated converter plate. This is likely due to the fact that the Al foil is transparent to the electron beam and consequently takes more time to thermally ionize. As a result, this foil slows the AK gap closure which ends the radiation pulse, but reduces the high spectral signals required to measure Zeeman splitting.

After the initial characterization of the anode plasma, the 0.15 m spectrometer was replaced with a high resolution, 0.32 m spectrometer. With a 2400 g/mm holographic grating and 50 μm slit, this spectrometer had a resolution of about 0.065 nm. In Chapter 5 C III/ C IV line ratios were compared to non-LTE PrismSPECT simulations to obtain electron temperatures. Temperatures for two standard SMP diodes increased toward the axis from about 5.6 eV to about 6.2 eV. A coated convertor shot without a foil resulted in slightly higher temperatures of 5.8-6.3 eV.

Measurements of Al III, C IV, H, and C II, were also performed to obtain electron densities from the Stark broadened lines. The profiles were deconvolved into Gaussian and Lorentizan components, and the Lorentzian FWHM was compared to Griem's tabulated Stark widths for H I and C II [20] and Prof. Maron's calculations for Al III and C IV [57].

H-alpha spectra were fit with two profiles for all 11 fibers, a higher intensity, smaller width component, and a lower intensity, larger width component in order to accurately fit the high density wings. Electron densities between about 1-4$\times10^{16}$ cm^{-3} were obtained for the low density component without correlation to the fiber position, similar to densities obtained from C II. Electron densities of 1-5$\times10^{17}$ cm^{-3} were obtained from the high density H-alpha fits, with densities rising slightly toward the axis. In contrast, C IV was fit with two densities for only the central 1-2 fibers closest to the axis. Electron densities ranged from 1-5$\times10^{17}$ cm^{-3} for the low density C IV fits, and 1-5$\times10^{18}$ cm^{-3} for the high density components, with densities rising toward the axis.

Because there is no correlation between the radius and electron density from H-alpha and since these measurements are integrated along the line of sight, it is likely that neutral hydrogen is located beyond the extent of the fiber array, far from the beam axis, due to lower electron temperatures at this location. C IV electron densities continue to rise toward the axis and therefore it is likely that C IV is present closer to the axis. The wings of the spectra may be due to a dense surface plasma, because the fiber lines of sight are essentially 1 mm diameter chords viewing across the anode. If an axial density gradient is present, a colder higher density surface plasma may be superimposed onto a lower density plasma further into the AK-gap than the anode surface. The high density wings measured on the H-alpha lines could be due to this dense surface plasma. If the surface is colder, then the C IV high density wings may only be seen close to the axis where the temperatures are higher. Further from the axis, only C IV from a less dense but higher temperature region is measured. These measurements are summarized with a qualitative sketch in Figure 6.1, and are discussed in detail in Chapter 4.

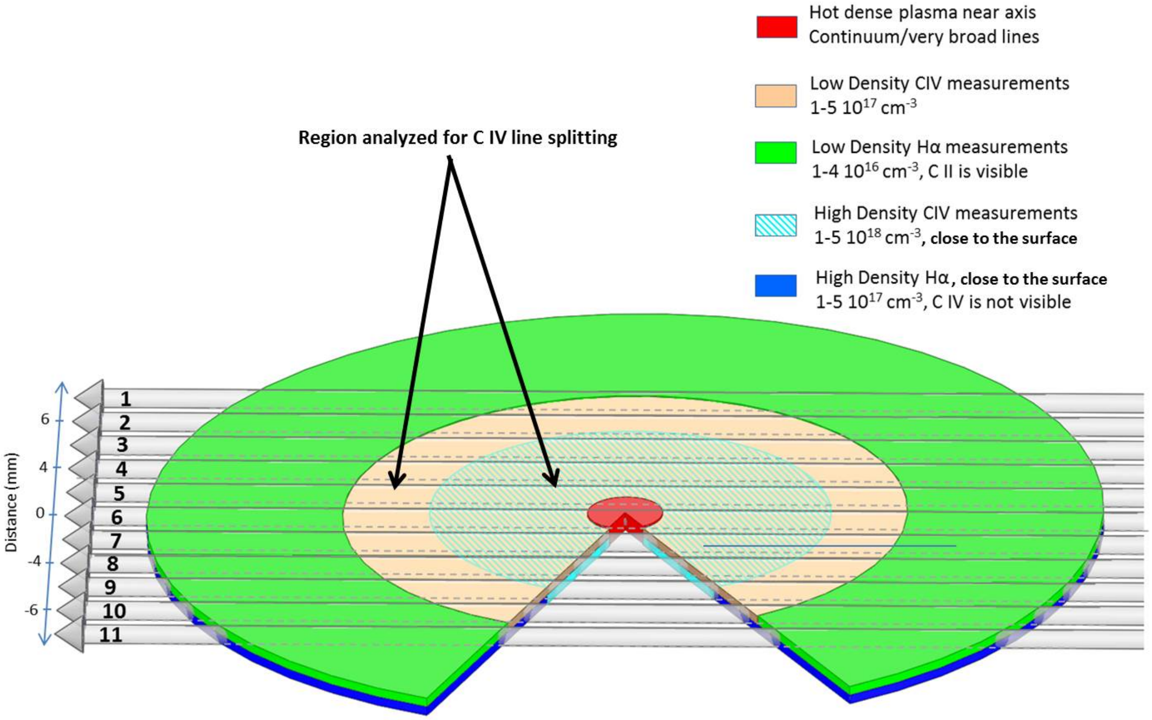

Figure 6.1: Sketch of the different density regions that may be present on the SMP anode surface to form the spectra discussed in Chapter 4. The arrows represent the fiber line of sight for the single row 200 um fiber array.

In order to separate the high density surface plasma and lower density plasma further from the surface a double fiber array was designed. This array consisted of two rows of 13, 100 μm fibers. The fibers were imaged to a 0.5 mm diameter, half the diameter of the 200 μm, single row array. Because C IV was never measured simultaneously on both rows, electron densities were estimated from Al III. Measurements of electron density from the fibers closest to the surface still required a two-density fit. Al III Stark widths from this row resulted in densities of 4-5$\times 10^{17}$ cm^{-3} for the low density and 0.9-3.5$\times 10^{18}$ cm^{-3} for the high density component. Al III Stark widths from the offset row, 0.5-1 mm from the anode surface, gave densities of 1-4$\times 10^{17}$ cm^{-3}, and did not require a two-density fit. Because the array closest to the surface had a large density gradient, there is likely a very dense surface plasma that occurs within <0.5 mm from the surface.

Future measurements of the anode electron densities could include a comparison between the foil surface and the bare convertor surface, to confirm that the foil surface does result in lower densities and therefore delays AK gap closure. Furthermore, an absolute calibration of the spectrometer for intensity can yield atomic and ionic densities [19]. Understanding the ratios of hydrogen to carbon abundances, for instance, may yield important insights into gap closure rates. Finally, measuring densities and temperatures between the foil and target surface in a standard SMP diode configuration, may help determine the plasma pressure in this region, which could be used to better characterize the role of the Al foil and determine possible beam defocusing effects due to high plasma pressures.

The Zeeman split C IV doublet was used to determine the current distribution in the diode in Chapter 5. These measurements suggest that the enclosed current continues to increase with the radius. In contrast, simulations suggest that nearly all of the diode current is located within a 2 mm radius. Measurements of the x-ray source spot size also fall within this radius, suggesting that most of the current should be located within 2 mm. There may be several explanations for this discrepancy. Although a significant fraction of the current appears to be outside the measured source size, the current density calculated from these measurements still appears to increase exponentially toward the axis. Therefore, the x-ray spot measurements could have a longer tail that is partially attenuated in the TRSD and image plate measurements.

Diamagnetism may also play a large role in these measurements. Simulations, framing camera images, and spectroscopy measurements, suggest that there are large density gradients close to the axis which can partially screen the beam currents magnetic field. The effect would be more pronounced close to the axis where the pressure gradients are the largest. The beam current, can therefore be carried near the diode axis, as the simulations and spot size measurements suggest, but diamagnetism, in which particle orbits orient to cancel the external magnetic field, could cause the measured current density to decrease.

Due to the low intensity of C IV at large radii, measurements of the enclosed current were limited to radii less than 10 mm. However, it does appear that the enclosed current may continue to increase to values larger than the B-dot measurements. This may be due to the sheath current or uniform knob emission which may be impacting the diode at large radii.

Several dopants, not typically measured in the SMP diode, were also evaluated. Dopant lines with high spectral signals in the SMP diode plasma may be used to obtain localized magnetic field measurements. Al III resulted in strong signals and line splitting was measured. Due to the electron temperatures on the anode surface, neutral lines may not be ideal for magnetic field profile measurements. For instance, Li I at 670.3 nm, had a strong signal, but like hydrogen, the width was essentially constant across the fiber array, suggesting that it was measured far from the axis.

The diode performance was greatly affected by the coatings. The salt coatings MgF2, NaCl, LiF, resulted in greater than 40 ns radiation pulse lengths, while boron, silicon, and aluminum coatings shortened the pulse. The reasons for this are not presently clear.

More work is still needed to truly localize these measurements. Placing a thin strip of a dopant across the diameter of the anode would result in a local measurement that could be used to obtain the current distribution without Abel inverting the line intensity or summing multiple magnetic field contributions along the line of sight. These measurements would also be parallel to the magnetic field and so the central pi component contribution to the Zeeman pattern would not be visible. Thin strips of NaCl, LiF, and Al, have been placed across the diameter of the anode. Na I and Li I emission lines were not present (which again suggests that these neutral atoms are located at radii larger than the extent of the fiber array). Al III showed strong signals but the spectra were taken after the shortened radiation pulse had ended.

Additional improvements to these measurements could involve an independent density measurement such as estimates from interferometry. This would remove the need to fit both the enclosed current and the Lorentzian FWHM for a given spectra, reducing fitting errors. With a known density, the line profile could be convolved with the instrument resolution and Doppler width, and any additional broadening may be assumed to be due to a magnetic field.

APPENDIX A

Electron Density Fits

Three shots were used to determine the electron density from H-alpha. The array imaged a bare tantalum surface for Shot 1948, and Al-coated tantalum surfaces for Shot 1949 and 1950. These fits are shown in this appendix. An 1800 g/mm grating was used on a 0.32 m spectrometer with a 50 um slit, resulting in a 0.094 nm instrument resolution. H-alpha and C II were fit and the electron densities were calculated in Chapter 4. Also shown are the Al III fits for Shot 2029 which used the double row fiber array, a 2400 g/mm grating, and a 50 um slit, to image a Na-coated tantalum target.

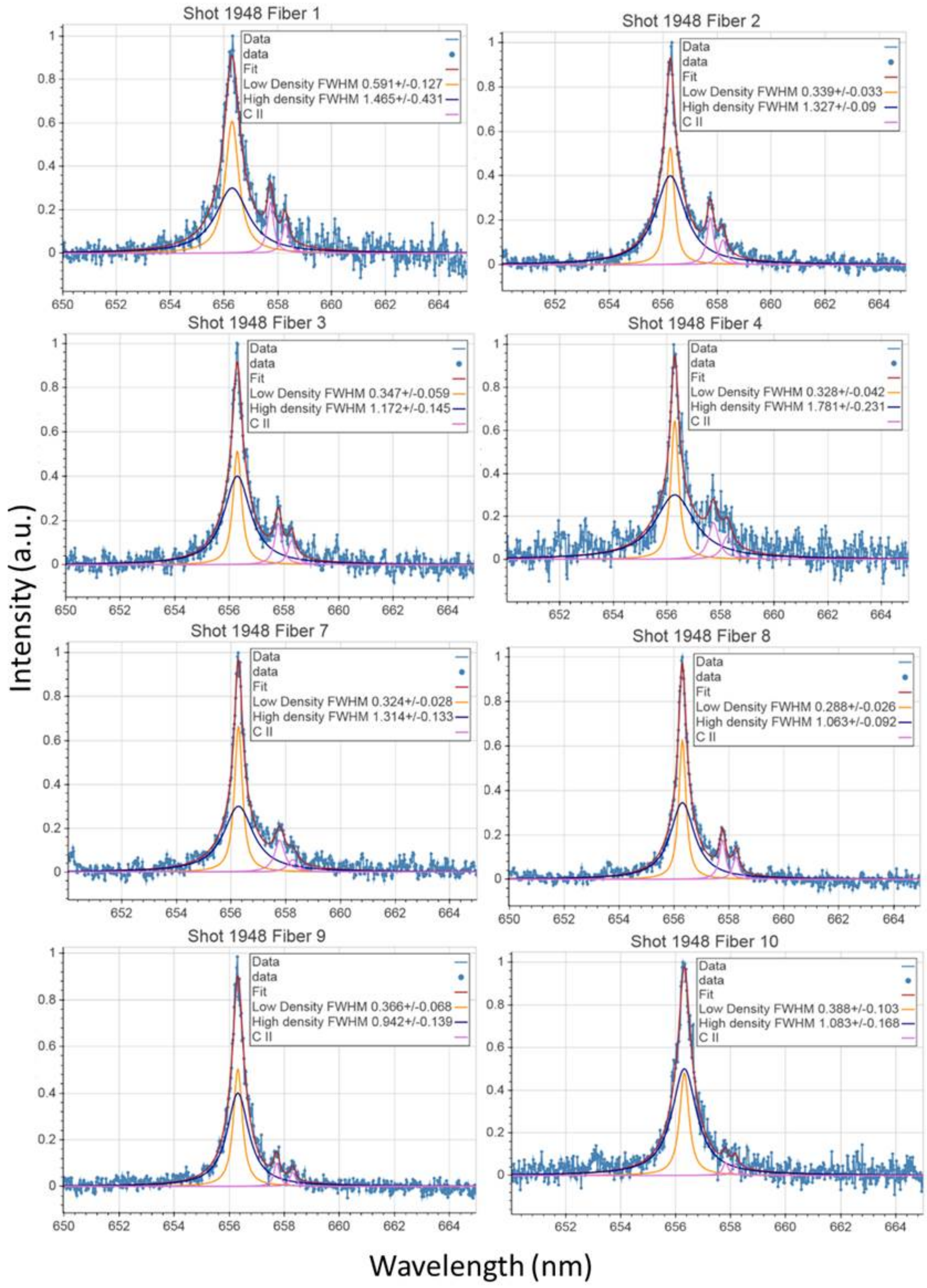

Figure A.1: Profile fits for Shot 1948 which had a bare Ta anode. Fiber 4 was at -2.45 mm and Fiber 7 was at 3.66 mm. The other fibers are 2 mm apart.

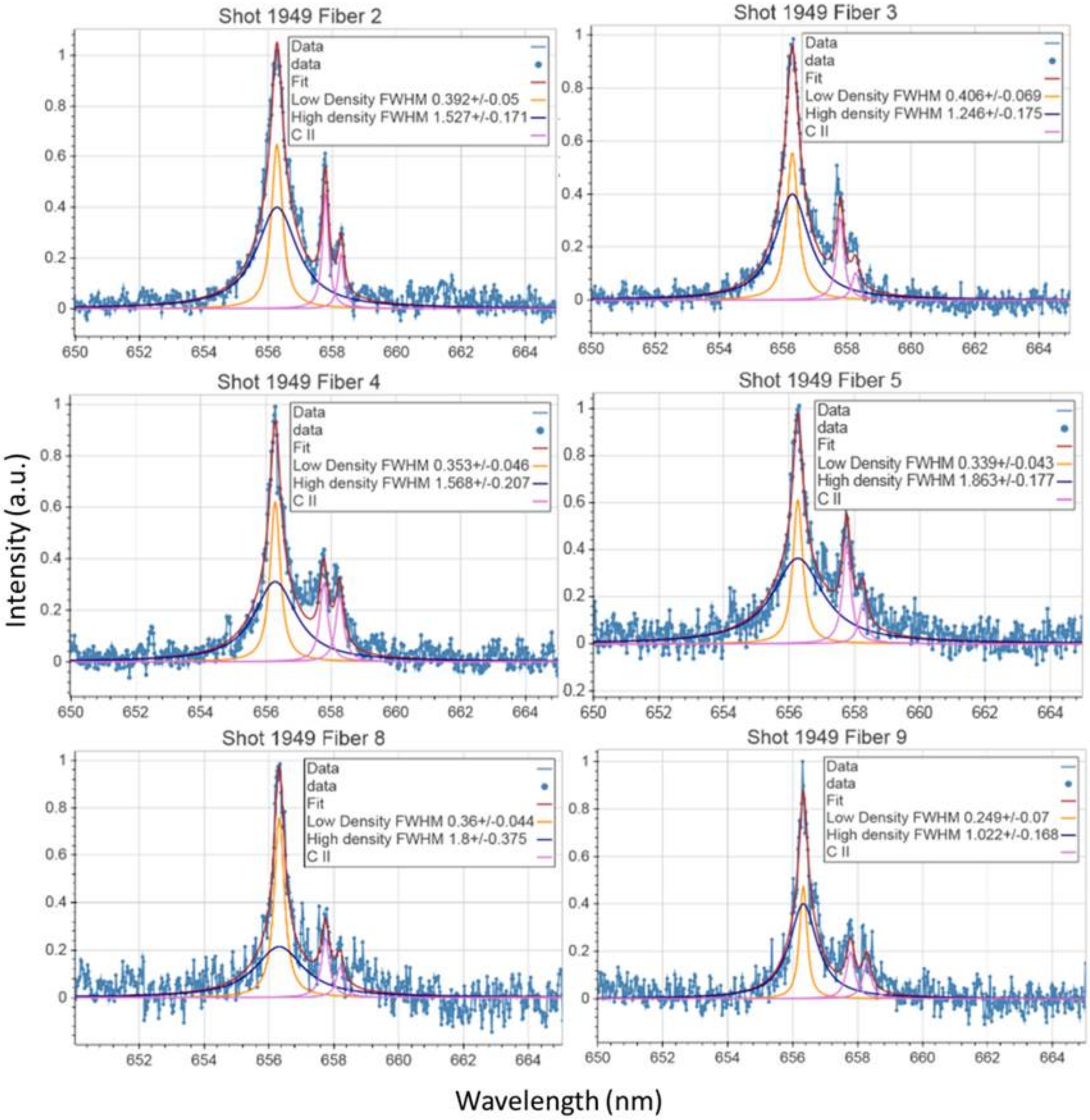

Figure A.2: Profile fits for Shot 1949 which had a Al-coated Ta anode. Fiber 5 was at -2.74 mm and Fiber 8 was at 3.2 mm. The other fibers are 2 mm apart.

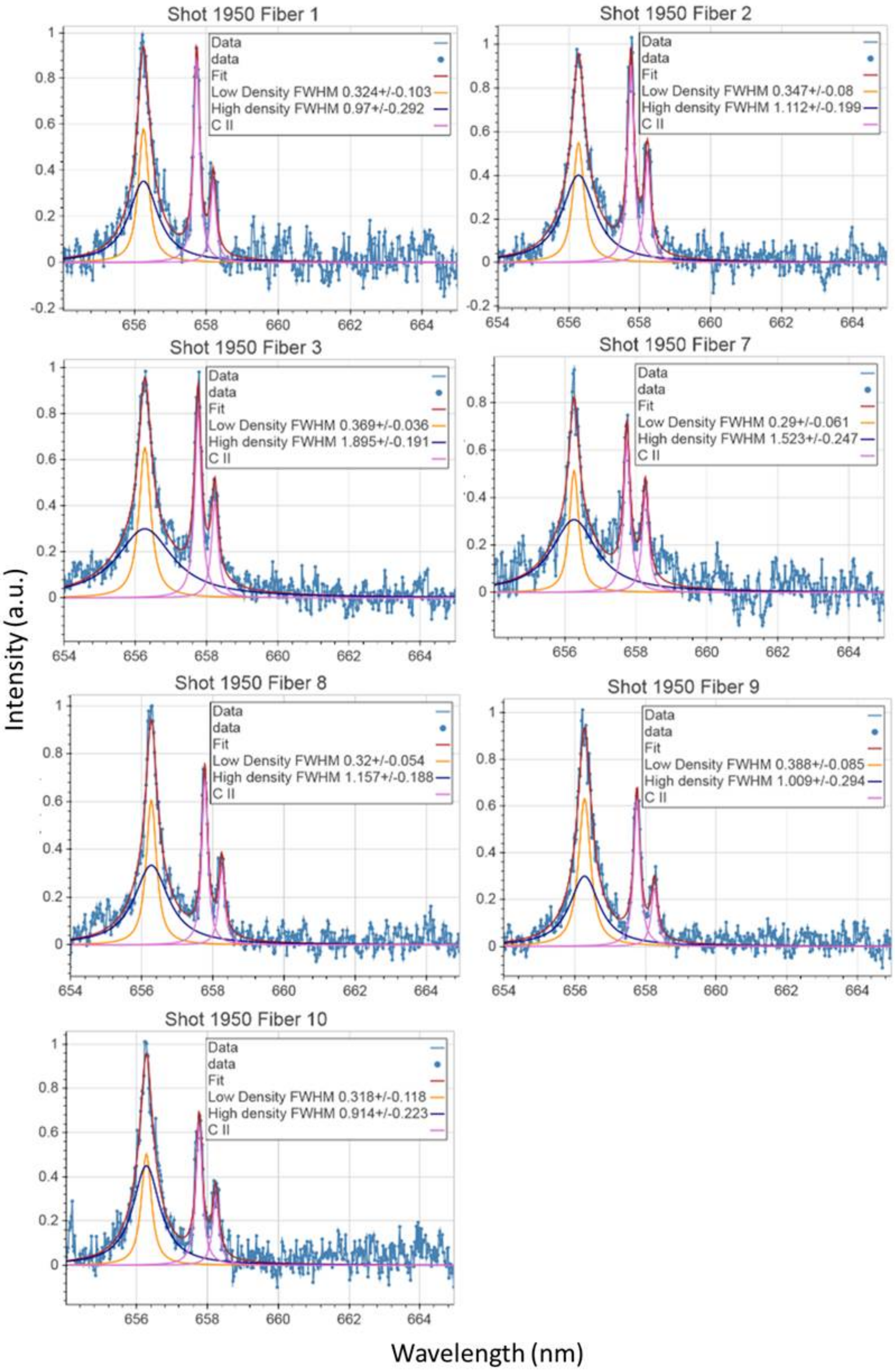

Figure A.3: Profile fits for Shot 1950 which had a Al-coated Ta anode. Fiber 3 was at -5.2 mm and Fiber 7 was at 2.8 mm. The other fibers are 2 mm apart.

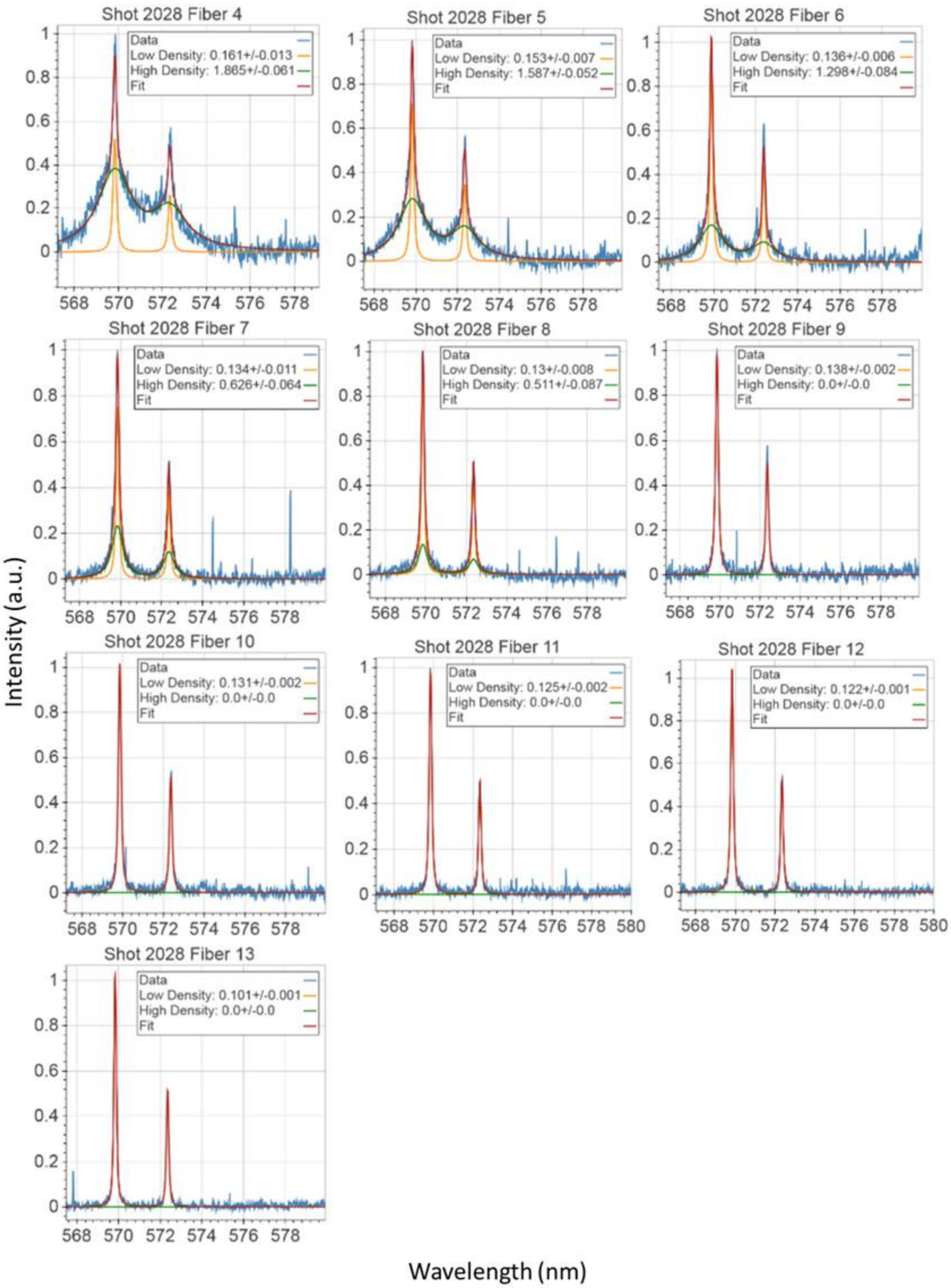

Figure A.4: Al III fits for Shot 2028, a Na-coated target. The double fiber array was used for this shot. These fits are for the fibers closest to the anode surface. Fiber 4 was located 2.65 mm from the axis. The fibers are separated by about 1 mm.

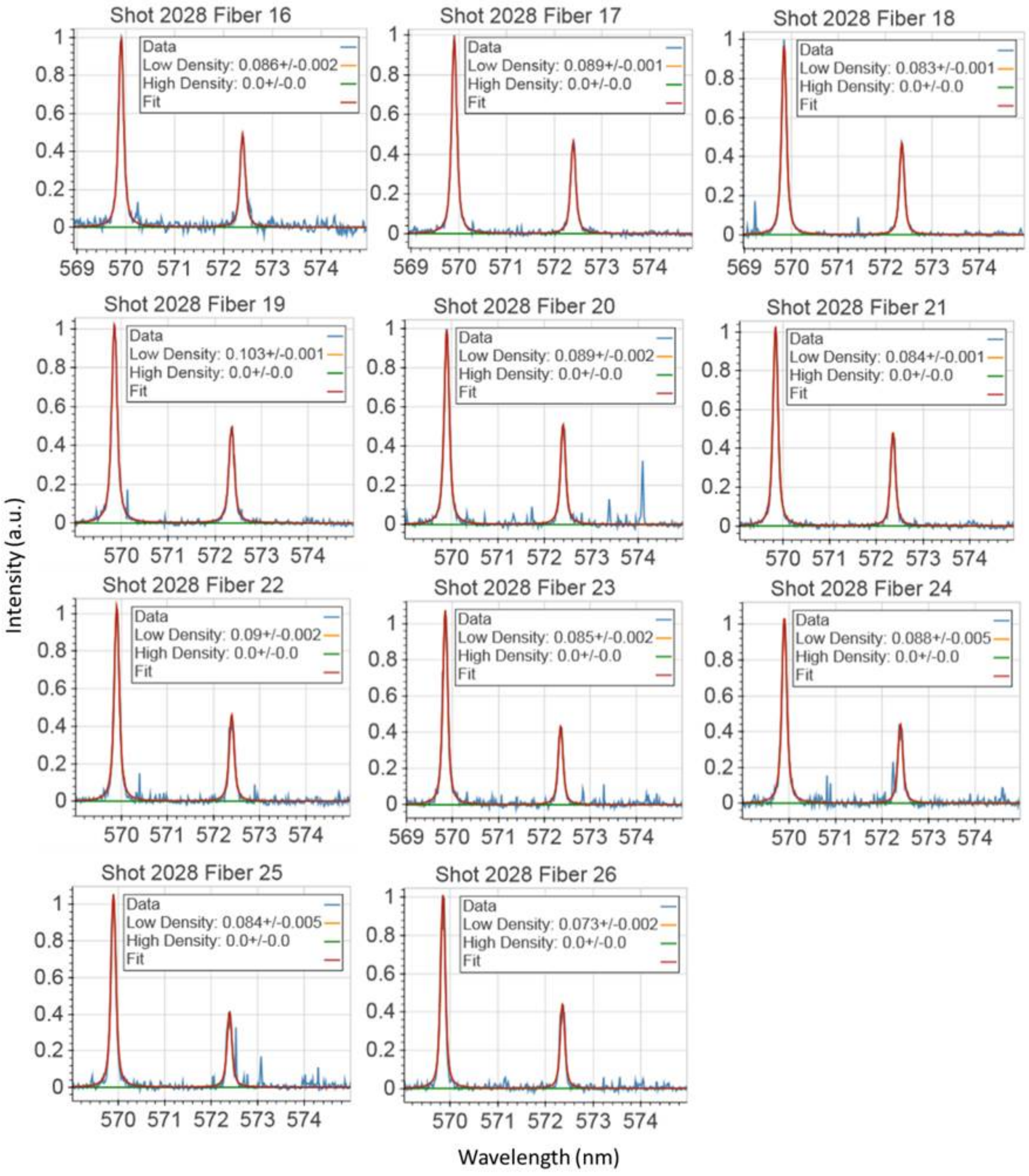

Figure A.5: Al III fits for Shot 2029, a Na-coated target. These fits are for the fibers offset from the anode surface by .5-1 mm. Fiber 16 was located 1.56 mm from the axis. The fibers are separated by about 1 mm.

APPENDIX B

Zeeman Splitting Fits of C IV

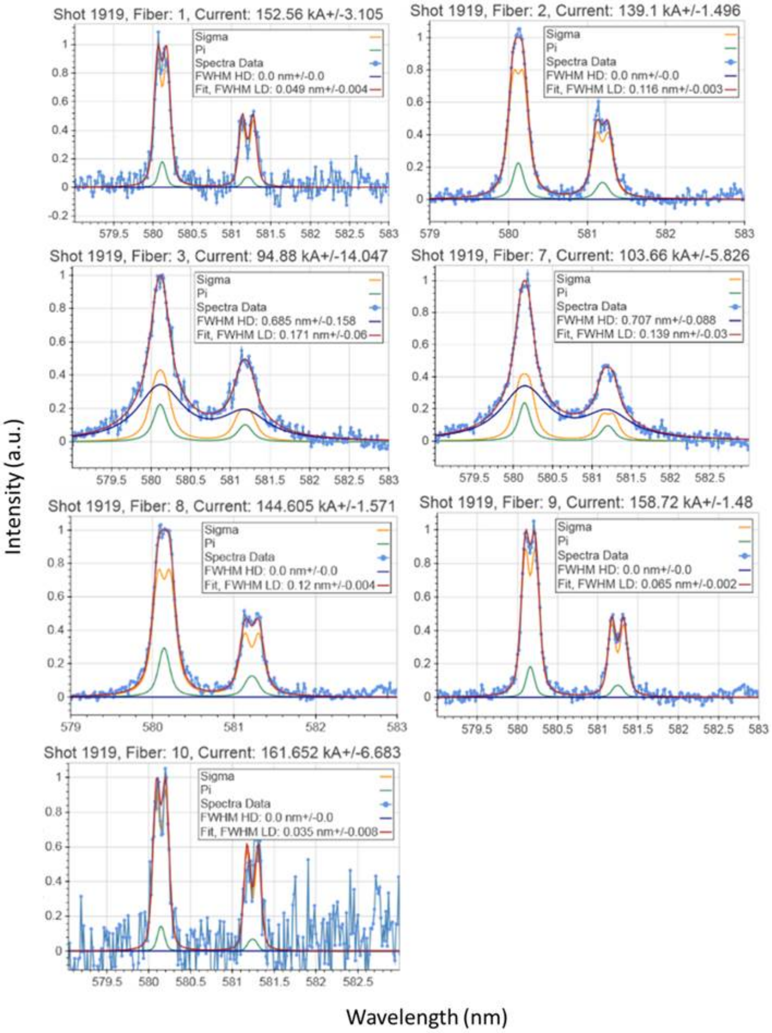

Figure B.1: Shot 1919, carbon-coated tantalum convertor with the single row fiber array. Fiber 4 was at -4.08 mm and Fiber 7 was at -4.07 mm, the fibers are separated by about 2 mm.

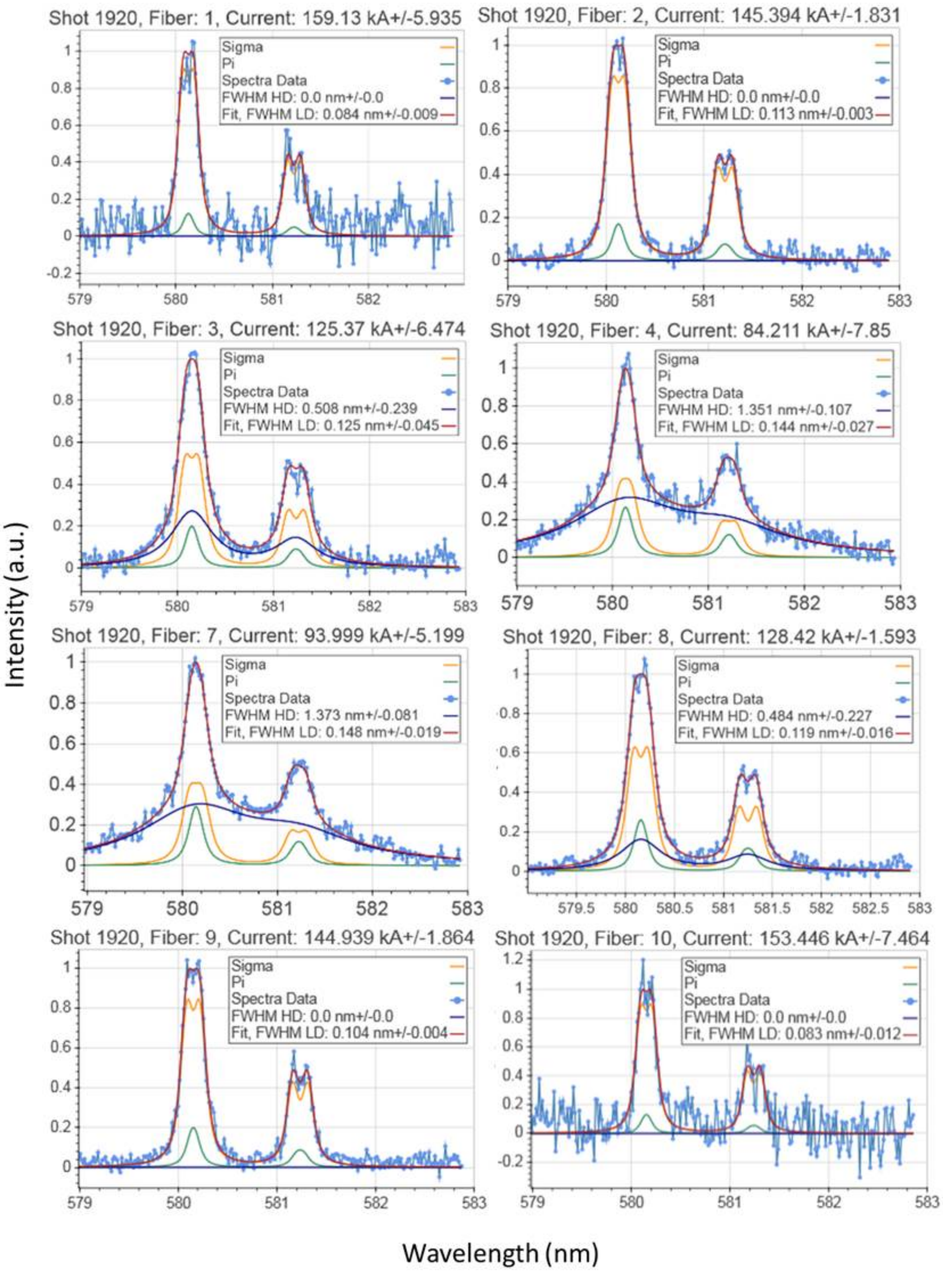

Figure B.2: Shot 1920, silicon-coated tungsten convertor with the single row fiber array. Fiber 4 was at -3.10 mm and Fiber 7 was at -3.0 mm, the fibers are separated by about 2 mm.

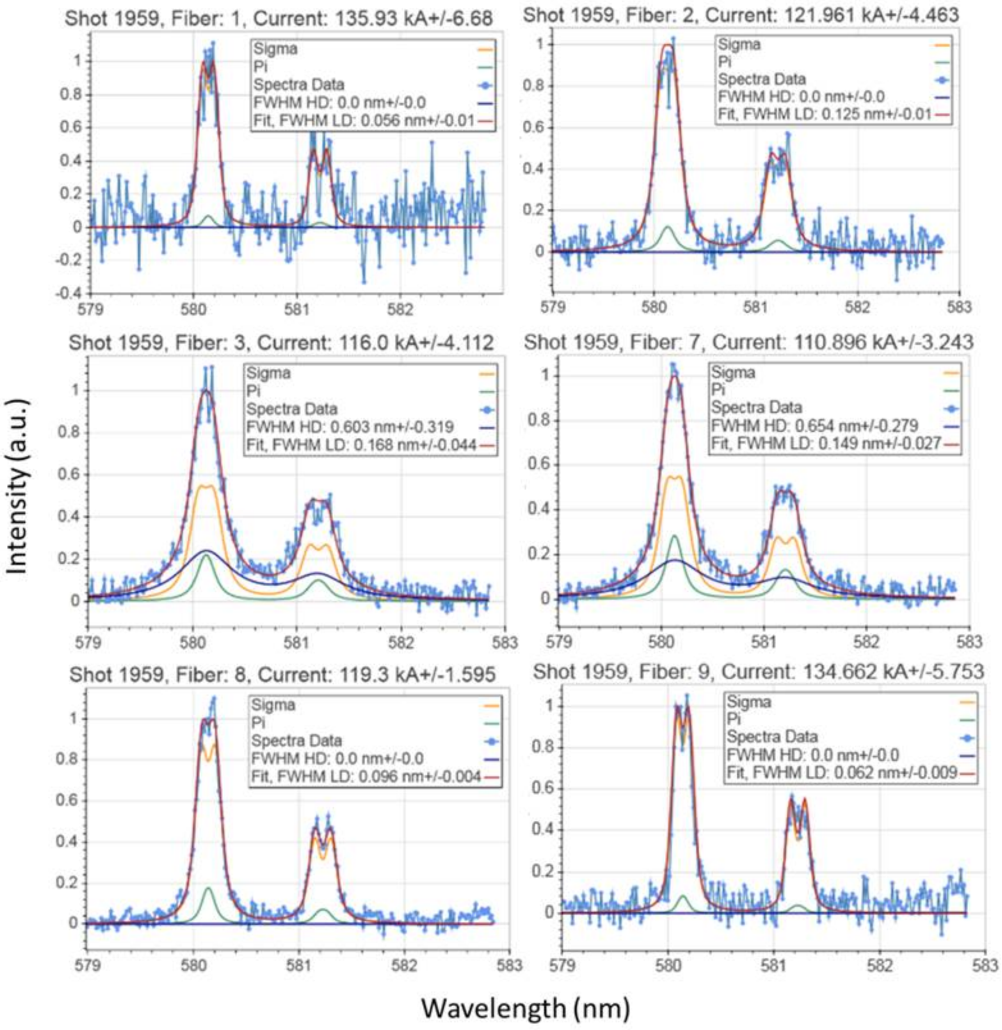

Figure B.3: Shot 1959, standard SMP Diode with an Al-foil and single row fiber array. Fiber 3 was at -3.9 mm and Fiber 7 was at 4.14 mm, the other fibers are separated by about 2 mm.

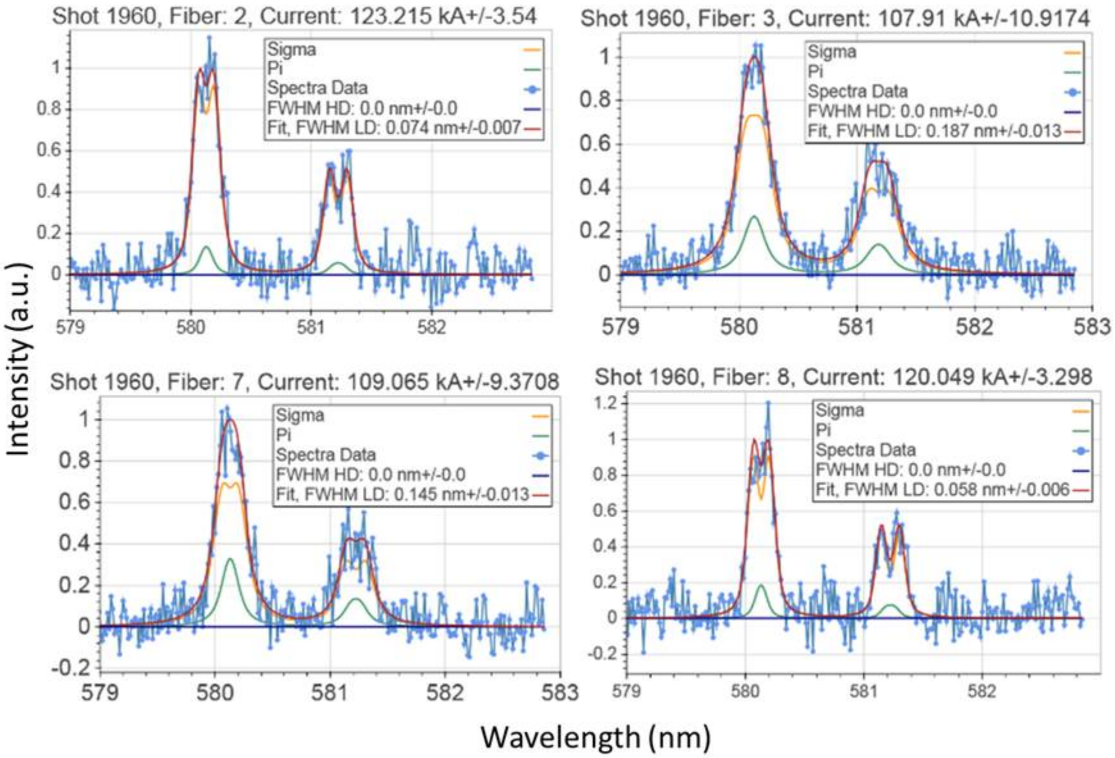

Figure B.4: Shot 1960, standard SMP Diode with an Al-foil and single row fiber array. Fiber 3 was at -4.0 mm and Fiber 7 was at 4.1 mm, the other fibers are separated by about 2 mm.

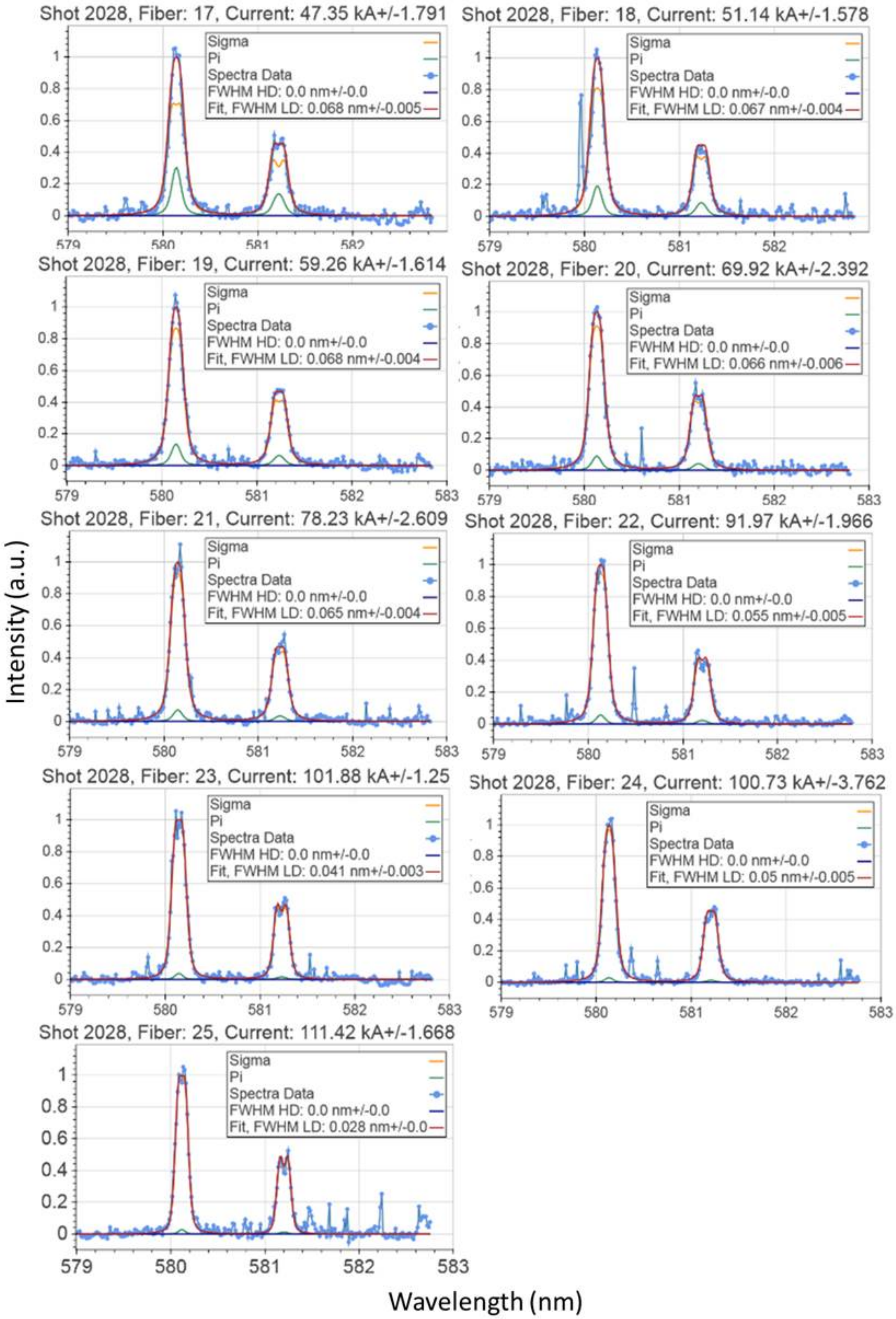

Figure B.5: Shot 2028, Al-coated target with the double row fiber array. Fiber 17 was at 2.6 mm. The other fibers are about 1 mm apart.

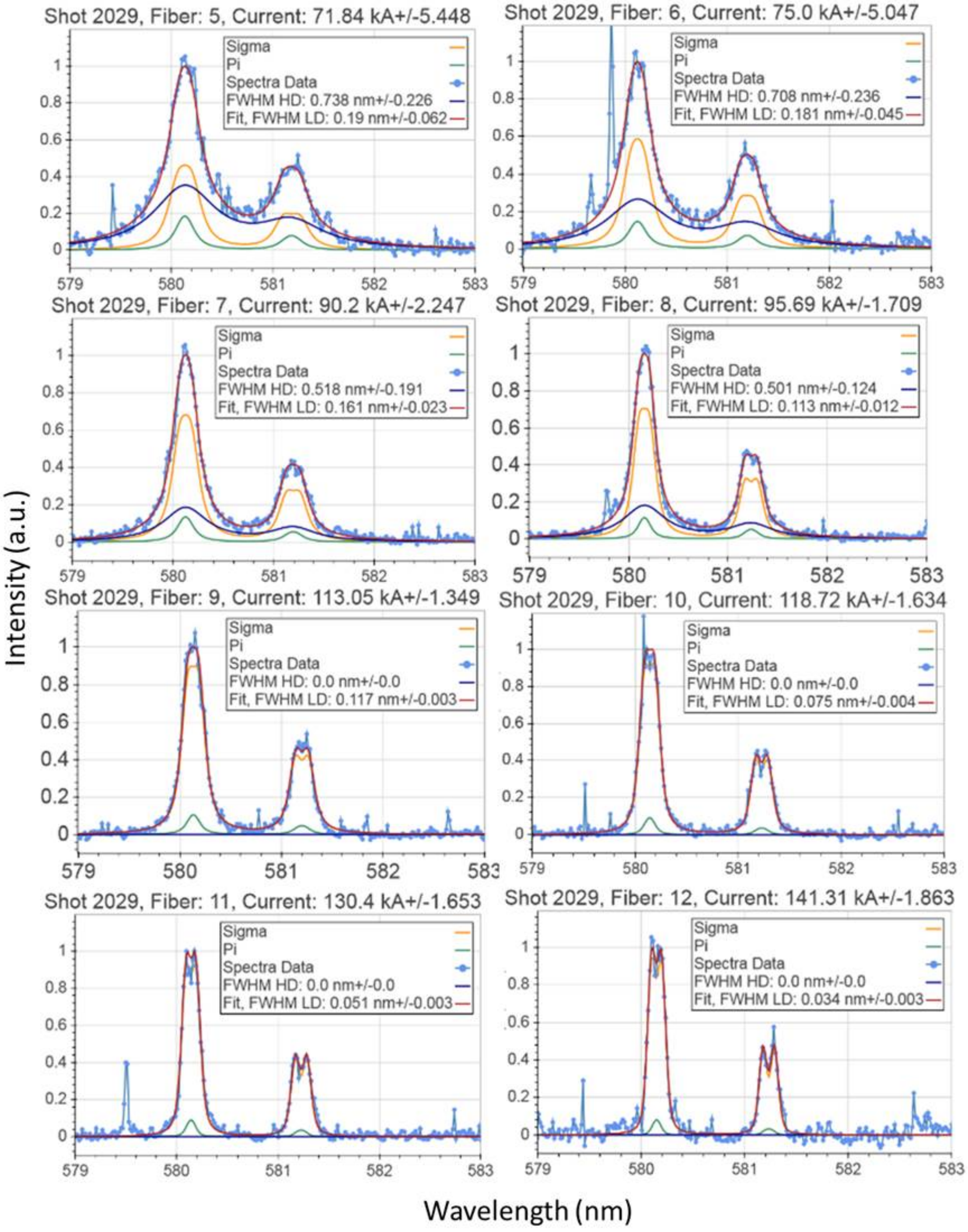

Figure B.6: Shot 2029, Na-coated target with the double row fiber array. Fiber 5 was at 2.8 mm. The other fibers are about 1 mm apart.

APPENDIX C

Zeeman Fitting Algorithm

```
pi = np.pi
m=4*pi*10**-7

#shot number and fiber number
shotnum='1920'
fibernum=3

#instrument resolution from the fit of the calibration lamp
int_res=.065
temperature=6
#get Doppler width
dop_width=doppler(temperature,580)
FWHM_G=np.sqrt(int_res**2+dop_width**2)

# fitting range in pixels
range1=670
range2=980
#Initial Guesses
#current enclosed
I=100000
#Lorentzian FWHM
FWHM_L=.167
#high density Lorentzian FWHM
hd_fw=.5
# high density component intensity
hd_h=.1
# 1/2-1/2 relativity intensity
constant=0.5

#obtain fiber position from a lineout across the fibers
fiber_mm=intensity_fall_off(shotnum,fibernum)
los=fiber_mm
```

```
#obtain abel inverted intensity
path = 'splitting plots data/abel inversion/'
radius=np.array(radius)
abel=np.array(abel)

#calculate equation of circle in x and y coordinates,
#radii is radius of circle, los is line of sight
def circle(radii, los):
    xp=np.linspace(-1*radii,radii,100)
    yp=((radii**2)-(xp**2))**.5
    return (xp,yp)

#calculate the tangent and angle at each radii
def Bphi(xp, yp, radii,los):
    isection=((radii**2)-(los**2))**.5
    slope=(isection)/(los)
    mtangent=-1/slope
    b=isection-(mtangent*los)
    xtangent=np.linspace(1,radii*1.2,9)
    #equation of tangent line
    ytangent=(mtangent*xtangent)+b
    #find angle tangent makes with horizontal line
    phi=abs(math.atan(mtangent))
    return (phi,isection,xtangent,ytangent)

#calculated zeeman profile
def zeeman_calculated(wavelength,I,FWHM_L,constant):

    #global varibles calculated elsewhere
    global abel
    global los
    global FWHM_G
    global Ep3_2, Ep1_2, Es1_2

    #step size for zeeman profile calculations
    radius=np.linspace(1,los+10,500)

    circles=[] #plots the circles and tangent lines
    total_spectra=0.0
    total_si=0.0
    total_pi=0.0

    #loop over the number of circles (step sizes)
    for i in xrange(0,len(radius),1):
        xp,yp=circle(radius[i],los)
```

```
        #get index value of los so only
        #radii that are less than depth of field are used
        xp_ind=min(range(len(xp)), key=lambda i:abs(xp[i]-los))

        if radius[i]<los:
            #plot circle contours not along LOS
            p0=[[xp,yp,'B Field \
            Contours not along LOS','color=seagreen']]
            circles.append(p0)

        if radius[i]>los and yp[xp_ind]<10:
#Plot contours along LOS up to depth of field/2
            phi,isection,xtan,ytan=Bphi(xp,yp,radius[i],los)
            r=radius[i]


 p0=[[xp,yp,'B Field Contours','color=cornflowerblue'], \
 [xtan,ytan,'Tangent','color=firebrick'],\
[[los],[isection],'scatter','tangent point',\
'color=firebrick']]
            circles.append(p0)

            #calculate B field at each circle
            B=m*(I)/(2*pi*r/1000)

 #calculate zeeman splitting, LOS perp to B.
 #All perp intensities are multiplied by the stoke calculations
            sim_spectra,si_spectra,\
            pi_spectra,p1_2_spectra, p3_2_spectra=\
            zeeman_splitting\
            (wavelength,B,FWHM_G, F WHM_L,Ep3_2,Ep1_2,Es1_2,\
            constant)

#this gets the intensity from the \
#abel inversion of C IV line for the radius of the current\
#circular contour
            abel_i=\
            abel[(np.abs(fiber_mm_sim - radius[i])).argmin()]

            #calculate sigma components
            si_voigt_comp=((1+(math.cos((pi/2)\
            -phi))**2)*si_spectra)*abel_i
            #calculate pi components
            pi_voigt_comp=(((math.sin((pi/2)\
            -phi))**2)*pi_spectra)*abel_i

            #add pi and sigma components to previously\
```

```
            #calculated contours
            total_si=np.array(total_si+si_voigt_comp)
            total_pi=np.array(total_pi+pi_voigt_comp)

    total_spectra=total_si+total_pi
    #normalize spectrum
    total_spectra=total_spectra/max(total_spectra)
    return total_si, total_pi,total_spectra,circles

def zeeman_fit(wavelength,I,FWHM_L,hd_FWHM_L,hd_c,constant):
#this function uses the energies fit from \
#previous function
    global Ep3_2
    global Ep1_2
    global Es1_2
    global FWHM_G
    h=4.13566733*10**-15
    c=2.99792458*10**8

    wavelength32=(h*c/(Ep3_2-Es1_2))*10**9
    wavelength12=(h*c/(Ep1_2-Es1_2))*10**9

    #calculate zeeman profile
    total_si, total_pi,total_spectra,circles=\
    zeeman_calculated(wavelength,I,FWHM_L)

    #calculate high density components for 3/2 and
    #1/2 transition
    highd_v1=voigt_plot(\
    wavelength,wavelength32,FWHM_G,hd_FWHM_L)*hd_c
    highd_v2=voigt_plot(\
    wavelength,wavelength12,FWHM_G,hd_FWHM_L)*.5*hd_c
    highd=highd_v1+highd_v2

    #calculate total spectrum including high density component
    total_spectra_hd=highd+total_spectra

    #return the total spectrum
    return total_spectra_hd

#if high density components are not present use this
def zeeman_fit_inner_ld(wavelength,I,FWHM_L,constant):
#this function uses the energies fit from the previous
#function

    total_si, total_pi,total_spectra_ld,circles=\
    zeeman_calculated(wavelength,I,FWHM_L)
```

```
    return total_spectra_ld

cal_line,raw_lamp,raw_spectra,location=shot_pics(shotnum)

#obtain vertical lineout region. 10 px lineout is default
y1,y2=location[fibernum-1]

#this calibrates the spectral data for the
#fiber chosen for wavelength and relative intensity.
#Base_spectra is the final calibrated spectrum
wavelength,spectra,intensity_spectra,norm_spectra,peaks,\
hg_spectra,fiber_int2,base_spectra=\
spectra_full_method(raw_spectra,raw_lamp,cal_line,\
[576.9598, 579.0663],y1,y2)

#fits data with calculated zeeman profile
#p0 is initial guess, curve_fit returns the
#best fit according to the Levenburg Marquardt
#fitting algorithm
#This fits enclosed current at the fiber position,
#the lorentzian FWHM for high density and low density component,
#and the intensity of the high density
#component
popt, pcov = curve_fit(zeeman_fit,wavelength[range1:range2],\
base_spectra[range1:range2]\
,p0=[(I,FWHM_L,hd_fw,hd_h,constant)])

hdfw=popt[2]
hd_c=popt[3]

#if the high density FWHM component of the fit is negative
#or the intensity is very small than try the fit again
#without a high density component
if popt[2]<0 or popt[3]<.0001:

#This fits enclosed current at the fiber
#position and a single lorentzian FWHM
popt, pcov =\ curve_fit(zeeman_fit_ld,\
wavelength[range1:range2],\
base_spectra[range1:range2],p0=[(I,FWHM_L,constant)])

#calculate error in the fit
perr=np.sqrt(np.diag(pcov))
```

BIBLIOGRAPHY

[1] D. L. Johnson, R. Altes, V. Bailey, P. Corcoran, I. Smith, S. Cordovaa, F. Griffina, K. Hahna, D. Jaramilloa, J. Maenchena, *et al.*, “Rits-6, a 10-mv inductive voltage adder accelerator,” in *Proceedings of the 13th International Symposium on High Current Electronics*, pp. 115–118, 2004.

[2] J. J. Leckbee, B. V. Oliver, M. D. Johnston, K. D. Hahn, S. Portillo, and B. Bui, “Negative-polarity rod-pinch diode experiments on rits-6,” in *Pulsed Power Conference, 2009. PPC’09. IEEE*, pp. 551–554, IEEE, 2009.

[3] K. Hahn, B. V. Oliver, M. D. Johnston, S. Portillo, J. Leckbee, D. Rovang, I. Molina, S. Cordova, G. Cooper, J. McLean, *et al.*, “Radiographic paraxial diode investigations on rits-6,” in *Pulsed Power Conference, 2007 16th IEEE International*, vol. 1, pp. 794–797, IEEE, 2007.

[4] N. Bennett, D. R. Welch, T. J. Webb, M. G. Mazarakis, M. L. Kiefer, M. D. Crain, D. W. Droemer, R. E. Gignac, M. D. Johnston, J. J. Leckbee, *et al.*, “The impact of plasma dynamics on the self-magnetic-pinch diode impedance,” *Physics of Plasmas (1994-present)*, vol. 22, no. 3, p. 033113, 2015.

[5] N. Bruner, D. R. Welch, K. D. Hahn, and B. V. Oliver, “Anode plasma dynamics in the self-magnetic-pinch diode,” *Physical Review Special Topics-Accelerators and Beams*, vol. 14, no. 2, p. 024401, 2011.

[6] B. V. Oliver, K. Hahn, M. D. Johnston, and S. Portillo, “Advances in high intensity e-beam diode development for flash x-ray radiography,” *Acta Physica Polonica-Series A General Physics*, vol. 115, no. 6, p. 1044, 2009.

[7] J. McCarrick, G. Caporaso, F. Chambers, Y.-J. Chen, S. Falabella, E. Goldin, G. Guethlein, D. Ho, R. Richardson, and J. Weir, “Electron beam/converter target interactions in radiographic accelerators,” in *Particle Accelerator Conference, 2003. PAC 2003. Proceedings of the*, vol. 1, pp. 563–567, IEEE, 2003.

[8] Y. Chen, T. Houck, J. McCarrick, and B. Poole, “Trapping backstreaming ions from an x-ray converter using an inductive cell,” tech. rep., Lawrence Livermore National Laboratory (LLNL), Livermore, CA, 1998.

[9] M. Tatarakis, R. Aliaga-Rossel, A. Dangor, and M. Haines, “Optical probing of fiber z-pinch plasmas,” *Physics of Plasmas (1994-present)*, vol. 5, no. 3, pp. 682–691, 1998.

[10] I. H. Hutchinson, *Principles of Plasma Diagnostics*. Cambridge University Press, 2005.

[11] D. Greenberger, K. Hentschel, and F. Weinert, *Compendium of quantum physics: concepts, experiments, history and philosophy*. Springer Science & Business Media, 2009.

[12] T. Robishaw, *Magnetic fields near and far: Galactic and extragalactic single-dish radio observations of the Zeeman effect*. Universal-Publishers, 2008.

[13] Prism Computational Sciences Inc., *PrismSPECT*, 1998.

[14] D. R. Welch, D. Rose, B. Oliver, and R. Clark, "Simulation techniques for heavy ion fusion chamber transport," *Nuclear Instruments and Methods in Physics Research Section A: Accelerators, Spectrometers, Detectors and Associated Equipment*, vol. 464, no. 1, pp. 134–139, 2001.

[15] T. P. Hughes, R. E. Clark, and S. Y. Simon, "Three-dimensional calculations for a 4 ka, 3.5 mv, 2 microsecond injector with asymmetric power feed," *Physical Review Special Topics-Accelerators and Beams*, vol. 2, no. 11, p. 110401, 1999.

[16] K. D. Hahn, N. Bruner, M. D. Johnston, B. V. Oliver, T. J. Webb, D. R. Welch, S. R. Cordova, I. Crotch, R. E. Gignac, J. J. Leckbee, *et al.*, "Overview of self-magnetically pinched-diode investigations on rits-6," *Plasma Science, IEEE Transactions on*, vol. 38, no. 10, pp. 2652–2662, 2010.

[17] M. A. Linne, *Spectroscopic measurement: an introduction to the fundamentals*. Academic Press, 2002.

[18] D. L. Andrews and A. A. Demidov, *An introduction to laser spectroscopy*. Springer Science & Business Media, 2012.

[19] H. R. Griem, *Principles of plasma spectroscopy*, vol. 2. Cambridge University Press, 2005.

[20] H. Griem, *Spectral line broadening by plasmas*. Elsevier, 2012.

[21] M. S. Dimitrijević and S. Sahal-Bréchot, "On the application of stark broadening data determined with a semiclassical perturbation approach," *Atoms*, vol. 2, no. 3, pp. 357–377, 2014.

[22] A. Lesage, "Experimental stark widths and shifts for spectral lines of neutral and ionized atoms a critical review of selected data for the period 2001–2007," *New Astronomy Reviews*, vol. 52, no. 11, pp. 471–535, 2009.

[23] J. Olivero and R. Longbothum, "Empirical fits to the voigt line width: A brief review," *Journal of Quantitative Spectroscopy and Radiative Transfer*, vol. 17, no. 2, pp. 233–236, 1977.

[24] D. J. Griffiths, *Introduction to Quantum Mechanics*. Pearson, 2013.

[25] Auletta, Gennaro and Fortunato, Mauro and Parisi, Giorgio, *Quantum Mechanics*. Cambridge University Press, 2009.

[26] A. E. Siegman, *Lasers*. University Science Books, 1986.

[27] A. Candler, *Atomic Spectra and the Vector Model*. Cambridge University Press, 2015.

[28] E. U. Condon and G. H. Shortley, *The theory of atomic spectra*. Cambridge University Press, 1951.

[29] B. Martin and D. Wickramasinghe, "Magneto-optical effects in magnetic white dwarfs–i. the line spectra," *Monthly Notices of the Royal Astronomical Society*, vol. 196, no. 1, pp. 23–31, 1981.

[30] A. Kawka and S. Vennes, "The cool magnetic daz white dwarf nltt 10480," *Astronomy & Astrophysics*, vol. 532, p. A7, 2011.

[31] S. Tessarin, D. Mikitchuk, R. Doron, E. Stambulchik, E. Kroupp, Y. Maron, D. Hammer, V. Jacobs, J. Seely, B. Oliver, *et al.*, "Beyond zeeman spectroscopy: Magnetic-field diagnostics with stark-dominated line shapes," *Physics of Plasmas (1994-present)*, vol. 18, no. 9, p. 093301, 2011.

[32] E. Stambulchik, K. Tsigutkin, and Y. Maron, "Spectroscopic method for measuring plasma magnetic fields having arbitrary distributions of direction and amplitude," *Physical review letters*, vol. 98, no. 22, p. 225001, 2007.

[33] J. Leckbee, B. Oliver, J. Maenchen, S. Portillo, M. Johnston, K. Hahn, D. Rovang, I. Molina, S. Cordova, D. L. Johnson, *et al.*, "Rits-6 output pulse modifications," in *Pulsed Power Conference, 2007 16th IEEE International*, vol. 2, pp. 1264–1267, IEEE, 2007.

[34] I. D. Smith, "Induction voltage adders and the induction accelerator family," *Physical Review Special Topics-Accelerators and Beams*, vol. 7, no. 6, p. 064801, 2004.

[35] N. Bennett, M. D. Crain, D. W. Droemer, R. E. Gignac, G. Lare, I. Molina, R. Obregon, C. C. Smith, F. L. Wilkins, D. R. Welch, *et al.*, "Shot reproducibility of the self-magnetic-pinch diode at 4.5 mv," *Physical Review Special Topics-Accelerators and Beams*, vol. 17, no. 5, p. 050401, 2014.

[36] M. Mazarakis, M. Johnston, M. Kiefer, J. Leckbee, T. Renk, T. Webb, D. Ziska, N. Bennett, *et al.*, "Dependence of the back-streaming ion current on the self-magnetic pinch (smp) electron diode parameters," *Bulletin of the American Physical Society*, vol. 60, 2015.

[37] S. R. Cordova, S. Portillo, B. V. Oliver, J. R. Threadgold, I. Crotch, and D. R. Ziska, "Characterization of the self magnetic pinch diode at high voltages for flash radiography.," tech. rep., Sandia National Laboratories, 2008.

[38] C. Mendel, D. Seidel, and S. Rosenthal, "A simple theory of magnetic insulation from basic physical considerations," *Laser and Particle Beams*, vol. 1, no. 03, pp. 311–320, 1983.

[39] P. Ottinger and J. Schumer, "Rescaling of equilibrium magnetically insulated flow theory based on results from particle-in-cell simulations," *Physics of Plasmas (1994-present)*, vol. 13, no. 6, p. 063109, 2006.

[40] "Pimax/pimax 2 system." `ftp://ftp.princetoninstruments.com/public/Manuals/Princeton%20Instruments/PI-MAX%20System%20Manual.pdf`. Accessed: 19-Apr-2016.

[41] W. Schrenk, *Analytical atomic spectroscopy*. Springer Science & Business Media, 2012.

[42] V. Protopopov, *Practical Opto-Electronics: An Illustrated Guide for the Laboratory*, vol. 184. Springer, 2014.

[43] K. N. Rao, *Molecular spectroscopy: modern research*. Elsevier, 2012.

[44] J. F. Rabek and G. W. Scott, *Photochemistry and photophysics*, vol. 1. CRC Press, 1989.

[45] "Princeton instruments-acton series-spectrographs/monochromators." `http://www.princetoninstruments.com/products/spec/actonseries/dsheet.aspx`. Accessed: 22-Dec-2015.

[46] J. McClure, "Anastigmatic imaging spectrograph," 2014. US Patent 8,773,659.

[47] R. Scientific, "Introduction to image intensifiers for scientific imaging," tech. rep., Technical Note, 2000.

[48] K. Kraus, *Photogrammetry: geometry from images and laser scans*. Walter de Gruyter, 2007.

[49] S. Portillo, S. Lutz, L. Mix, K. Hahn, D. Rovang, J. E. Maenchen, I. Molina, S. Cordova, D. Droemer, R. Chavez, *et al.*, "Time-resolved spot size measurements from various radiographic diodes on the rits-3 accelerator," *Plasma Science, IEEE Transactions on*, vol. 34, no. 5, pp. 1908–1913, 2006.

[50] S. Lutz, D. Droemer, D. Devore, D. Rovang, S. Portillo, and J. Maenchen, "Development of a dynamic spot size diagnostic for flash radiographic x-ray sources," in *Pulsed Power Conference, 2003. Digest of Technical Papers. PPC-2003. 14th IEEE International*, vol. 1, pp. 197–200, IEEE, 2003.

[51] C. Ekdahl, "Characterizing flash-radiography source spots," *JOSA A*, vol. 28, no. 12, pp. 2501–2509, 2011.

[52] T. Webb. personal communication, 2016.

[53] D. Goude and J. Threadgold, “Lsp simulations of the self-magnetic-pinch-diode,” in *Pulsed Power Conference (PPC), 2015 IEEE*, pp. 1–6, IEEE, 2015.

[54] Y. Ralchenko, “Nist atomic spectra database.,” *Memorie della Societa Astronomica Italiana Supplementi*, vol. 8, p. 96, 2005.

[55] S. Sahal-Bréchot, M. S. Dimitrijević, and N. B. Nessib, “Widths and shifts of isolated lines of neutral and ionized atoms perturbed by collisions with electrons and ions: An outline of the semiclassical perturbation (scp) method and of the approximations used for the calculations,” *Atoms*, vol. 2, no. 2, pp. 225–252, 2014.

[56] M. S. Dimitrijević and N. Konjević, “Stark widths of doubly-and triply-ionized atom lines,” *Journal of Quantitative Spectroscopy and Radiative Transfer*, vol. 24, no. 6, pp. 451–459, 1980.

[57] R. Stamm, E. Smith, and B. Talin, “Study of hydrogen stark profiles by means of computer simulation,” *Physical Review A*, vol. 30, no. 4, p. 2039, 1984.

[58] E. Stambulchik and Y. Maron, “A study of ion-dynamics and correlation effects for spectral line broadening in plasma: K-shell lines,” *Journal of Quantitative Spectroscopy and Radiative Transfer*, vol. 99, no. 1, pp. 730–749, 2006.

[59] M. Dimitrijevic, S. Sahal-Bréchot, and V. Bommier, “Stark broadening of spectral lines of multicharged ions of astrophysical interest. i-c iv lines. ii-si iv lines,” *Astronomy and Astrophysics Supplement Series*, vol. 89, pp. 581–598, 1991.

[60] B. Blagojević, M. Popović, N. Konjević, and M. S. DIMITRIJEVIĆ, “Stark broadening parameters of analogous spectral lines along the lithium and beryllium isoelectronic sequences,” *Journal of Quantitative Spectroscopy and Radiative Transfer*, vol. 61, no. 3, pp. 361–375, 1999.

[61] H. Elabidi, S. Sahal-Bréchot, and N. B. Nessib, “Quantum stark broadening of 3s–3p spectral lines in li-like ions; z-scaling and comparison with semi-classical perturbation theory,” *The European Physical Journal D*, vol. 54, no. 1, pp. 51–64, 2009.

[62] S. Glenzer, N. Uzelac, and H.-J. Kunze, “Stark broadening of spectral lines along the isoelectronic sequence of li,” *Physical Review A*, vol. 45, no. 12, p. 8795, 1992.

[63] M. Dimitrijevic, Z. Djuric, and A. Mihajlov, “Stark broadening of al iii and cu iv lines for diagnostic of the rail gun arc plasma,” *Journal of Physics D: Applied Physics*, vol. 27, no. 2, p. 247, 1994.

[64] G. Cristoforetti, A. De Giacomo, M. Dell’Aglio, S. Legnaioli, E. Tognoni, V. Palleschi, and N. Omenetto, “Local thermodynamic equilibrium in laser-induced breakdown spectroscopy: beyond the mcwhirter criterion,” *Spectrochimica Acta Part B: Atomic Spectroscopy*, vol. 65, no. 1, pp. 86–95, 2010.

[65] P. Bogen, “Pressure broadening of multiply ionized carbon lines,” *Zeitschrift für Naturforschung A*, vol. 27, no. 2, pp. 210–214, 1972.

[66] H.-J. Kunze, *Introduction to plasma spectroscopy*, vol. 56. Springer Science & Business Media, 2009.

[67] T. E. Oliphant, "Python for scientific computing," *Computing in Science & Engineering*, vol. 9, no. 3, pp. 10–20, 2007.

[68] N. Bennett. personal communication, 2016.

[69] J. Cooper, "Plasma spectroscopy," *Reports on Progress in Physics*, vol. 29, no. 1, p. 35, 1966.

[70] F. F. Chen, *Introduction to Plasma Physics and Controlled Fusion*. Springer, 2006.

[71] M. Haines, "Particle orbits, diamagnetism, and energy balance in a z-pinch satisfying the lawson criterion," *Journal of Physics D: Applied Physics*, vol. 11, no. 12, p. 1709, 1978.

[72] J. I. Rintamaki, *Effects of RF Plasma Processing on the Impedance and Electron Emission Characteristics of a MV Beam Diode*. PhD thesis, University of Michigan, 1999.

[73] J. Rintamaki, R. Gilgenbach, W. Cohen, R. Jaynes, M. Cuneo, and P. Menge, "Radio frequency plasma processing effects on the emission characteristics of a mev electron beam cathode," *Applied physics letters*, vol. 75, no. 1, pp. 31–33, 1999.

[74] M. Cuneo, "The effect of electrode contamination, cleaning and conditioning on high-energy pulsed-power device performance," *Dielectrics and Electrical Insulation, IEEE Transactions on*, vol. 6, no. 4, pp. 469–485, 1999.

[75] J. Benford, D. Price, and W. DeHope, "Lowered plasma velocity with cesium iodide/carbon fiber cathodes at high electric fields," in *High-Power Particle Beams, 1998. BEAMS'98. Proceedings of the 12th International Conference on*, vol. 2, pp. 695–698, IEEE, 1998.

[76] D. A. Shiffler, M. J. LaCour, M. D. Sena, M. D. Mitchell, M. D. Haworth, K. J. Hendricks, and T. A. Spencer, "Comparison of carbon fiber and cesium iodide-coated carbon fiber cathodes," *Plasma Science, IEEE Transactions on*, vol. 28, no. 3, pp. 517–522, 2000.